

# Optical and Structural Analysis of Luminescent Nanoparticles in Glasses for Medical Diagnostics

## Dissertation

zur Erlangung des  
Doktorgrades der Naturwissenschaften (*Dr. rer. nat.*)

der

Naturwissenschaftlichen Fakultät II

Physik

der Martin-Luther-Universität  
Halle-Wittenberg,

vorgelegt

von Herrn M.Sc. Christian Paßlick  
geb. am 14.04.1985 in Bad Driburg

## Gutachter

- 1 : Prof. Dr. Stefan Schweizer, Fachhochschule Südwestfalen Standort Soest
- 2 : Prof. Dr. Ralf B. Wehrspohn, Martin-Luther-Universität Halle-Wittenberg
- 3 : Prof. Dr. Albrecht Winnacker, Friedrich-Alexander Universität Erlangen-Nürnberg

März 2013

Tag der Verteidigung: 26.11.2013



## ABSTRACT

---

In this thesis fluorescent europium (Eu)- and barium chloride ( $\text{BaCl}_2$ )-doped fluorozirconate (FZ) based glasses and glass ceramics, which are known for their efficient scintillation and storage phosphor properties, were the subject of improvement going along with their structural and optical investigation. In applications like digital radiography, they already provide image resolutions which are one order higher than that of commercially used polycrystalline state of the art detector screens, but they suffer from their lower light output. In order to become competitive, the fluorescence efficiency of the glass systems must increase. The fastest and easiest way is through an increase of the doping level of the fluorescent activator  $\text{Eu}^{2+}$ . This level is unfortunately limited due to energy quenching effects and hence also other possibilities have to be investigated. X-ray absorption near edge structure (XANES) measurements have shown that a small but significant amount of trivalent  $\text{Eu}^{3+}$  is always present in the glass, which is formed by partial oxidation of  $\text{Eu}^{2+}$  during the melting step or is already added to the glass by oxygen contaminated powdered  $\text{Eu}^{2+}$  raw material. Therefore, one main focus of this work was the investigation and optimization of the Eu valency as XANES measurements additionally showed that cheaper  $\text{Eu}^{3+}$  can partially be reduced to  $\text{Eu}^{2+}$  during glass melting lowering the total glass ceramic costs. However, photostimulated luminescence measurements revealed that  $\text{Eu}^{3+}$  is essential for the storage phosphor effect and a higher conversion efficiency.

Several routes were explored in order to improve the complex FZ glass system and in particular the  $\text{Eu}^{2+}$  luminescence efficiency. It is shown that the addition of indium to the glass host improves glass quality. Differential scanning calorimetry and x-ray diffraction showed that it is also needed for a phase transformation from hexagonal to orthorhombic phase  $\text{BaCl}_2$  nanoparticles, which is important for storage phosphor applications. Subsequent remelting of the glass has proved to increase the  $\text{Eu}^{2+}$  content and thus the performance of the glass ceramics for scintillator applications. Additional co-doping with other trivalent rare earths, namely Gd, Nd, Yb, or Tb, for light output enhancement influenced the nanocrystal nucleation and growth as well as the  $\text{Eu}^{2+}$  photoluminescence.

In order to address issues with homogeneity and reproducibility of the produced FZ based glasses and glass ceramics, borate glasses, known for their highly optical transparency, good reproducibility and low production costs were introduced as host for  $\text{Eu}^{2+}$  ions and orthorhombic  $\text{BaCl}_2$  nanoparticles. First investigations have shown a full ceramization of the glass directly after the pouring step. The metastable hexagonal  $\text{BaCl}_2$  was not observed.

The  $\text{Eu}^{2+}$ -doped FCZ based glass system was chosen for the development of radiation detection fibers, which have proven their functionality under UV excitation.



# CONTENTS

---

<b>I THE BASICS</b>	<b>1</b>
1 INTRODUCTION	3
2 PHYSICAL BACKGROUND	7
2.1 X-ray Storage Phosphors . . . . .	7
2.1.1 Spatial Resolution . . . . .	8
2.1.2 Photostimulated Luminescence . . . . .	10
2.2 Photon Conversion Processes . . . . .	11
2.2.1 General Processes . . . . .	11
2.2.2 Photoluminescence . . . . .	12
2.3 Rare-Earth Ions . . . . .	14
2.3.1 General characteristics . . . . .	14
2.3.2 Europium . . . . .	14
2.4 Matrix Materials . . . . .	17
2.4.1 ZBLAN . . . . .	17
2.4.2 Borate Glasses . . . . .	18
2.4.3 Barium Chloride . . . . .	18
2.5 Additional Experimental Methods . . . . .	19
2.5.1 X-Ray Absorption Near Edge Structure . . . . .	19
2.5.2 X-Ray Diffraction . . . . .	22
2.5.3 Differential Scanning Calorimetry . . . . .	23
<b>II THE RESULTS</b>	<b>25</b>
3 INDIUM AND REMELTING	27
3.1 X-Ray Absorption Near Edge Structure . . . . .	28
3.2 Differential Scanning Calorimetry . . . . .	31
3.3 X-Ray Diffraction . . . . .	32
3.4 Photoluminescence . . . . .	35
3.5 Discussion . . . . .	35
4 MULTIVALENT EUROPIUM-DOPING	39
4.1 X-Ray Absorption Near Edge Structure . . . . .	40
4.2 Differential Scanning Calorimetry . . . . .	42
4.3 X-Ray Diffraction . . . . .	47
4.4 Photoluminescence . . . . .	51
4.5 Photostimulated Luminescence . . . . .	53
4.6 Discussion . . . . .	55
5 RARE-EARTH CO-DOPING	57
5.1 X-Ray Absorption Near Edge Structure . . . . .	57
5.2 Differential Scanning Calorimetry . . . . .	58
5.2.1 Preliminary Investigations . . . . .	58
5.2.2 Co-Doping Investigations . . . . .	62
5.3 X-Ray Diffraction . . . . .	65
5.4 Photoluminescence . . . . .	67
5.5 Photostimulated Luminescence . . . . .	71

5.6	Discussion . . . . .	72
6	EU-DOPED BORATE GLASS CERAMICS	75
6.1	X-Ray Absorption Near Edge Structure . . . . .	75
6.2	X-Ray Diffraction . . . . .	77
6.3	Photoluminescence . . . . .	78
6.4	Photostimulated Luminescence . . . . .	82
6.5	Discussion . . . . .	82
7	RADIATION DETECTION FIBERS	85
7.1	Fiber pulling via pipette . . . . .	85
7.2	Fiber pulling via capillary . . . . .	86
7.3	Photoluminescence . . . . .	88
7.4	Discussion . . . . .	90
8	SUMMARY	93
9	OUTLOOK	97
	<b>III APPENDIX</b>	99
A	CALCULATION OF THE PSL PARAMETERS	101
A.1	Conversion Efficiency . . . . .	101
A.2	Stimulation Energy . . . . .	101
B	ERROR CALCULATION	103
B.1	Thermal Stability Parameters . . . . .	103
B.2	Photostimulated Luminescence . . . . .	103
B.3	X-ray Absorption Near Edge Structure . . . . .	104
C	MISCELLANEOUS	105
C.1	Used Filters . . . . .	105
	<b>BIBLIOGRAPHY</b>	107
	<b>PUBLICATIONS</b>	113
	<b>ACKNOWLEDGEMENTS</b>	117
	<b>CURRICULUM VITAE</b>	119
	<b>DECLARATION</b>	123

## ACRONYMS

---

BDE	bond dissociation energy
BFB	barium fluoride bromide
CE	conversion efficiency
DSC	differential scanning calorimetry
DPSS	diode-pumped solid state
EXAFS	x-ray absorption fine structure
FCZ	fluorochlorozirconate
FWHM	full width at half maximum
FZ	fluorozirconate
HMFG	heavy metal fluoride glasses
IR	infrared
LCB	lithiumchloroborate
MTF	modulation transfer function
NEXAFS	near edge x-ray absorption fine structure
PL	photoluminescence
PSL	photostimulated luminescence
RE	rare-earth
SDD	silicon drift detector
SE	stimulation energy
SEM	scanning electron microscope
UV	ultraviolet
WL	white line
XANES	x-ray absorption near-edge structure
XRD	x-ray diffraction



Part I

THE BASICS



## INTRODUCTION

---

Starting in 1895 with the discovery of x-rays by *W. C. Röntgen*, the evolution and technical developments in the field of ionizing radiation detection, especially in medical diagnostics, are constantly improving to meet modern requirements. Higher life expectancy, along with an increasing number of cancer cases, demand new inexpensive systems with excellent properties to increase the probability of an early diagnosis and prospect of cure. A changeover from analog investigation techniques such as film-screens for x-ray detection to digital radiography is still ongoing. Polycrystalline materials are most commonly used.

Most digital radiography systems produce their images by converting x-rays into visible light. In direct radiography (DR), the energy conversion is done instantly via scintillator screens, while in computed radiography (CR) the radiation image can be stored into electron-hole (e-h) traps of a storage phosphor screen with read-out afterwards via a photostimulation process with an external laser. By laser stimulation the e-h pairs recombine and the released energy is transferred to doped fluorescent activators which emit photons with characteristic energies [2]. Figure 1 shows the comparison between computed radiography (left) with powdered polycrystalline materials, for example, the most commercially used x-ray storage phosphor barium fluoride bromide (BaFBr) doped with divalent europium ( $\text{Eu}^{2+}$ ) and conventional screen-film radiography (right). It can be seen, that digital radiography provides a higher sensitivity with a larger dynamic range. In addition, these x-ray storage phosphor materials offer the advantage of multiple use and fast digital processing. However, the image quality of BaFBr: $\text{Eu}^{2+}$  is inferior to film-screen systems due to scattering of the read-out laser light by the crystal grains, decreasing the spatial resolution. Another disadvantage is the requirement of a point-by-point read-out to achieve the specified resolution.

In order to overcome the limitations described above, fluorescent nanoparticles embedded in transparent fluorozirconate (FZ) based glasses and glass ceramics came in the spotlight of research and development. They promise high potential as image plates for high-resolution digital radiography applications and provide some advantages compared to common polycrystalline materials [3–6]. They are re-usable, less expensive, can be read in a single imaging event and do not lose resolution or show noise due to light scattering from grain boundaries of the polycrystalline powder [2, 7].

When doped with fluorescent activators like rare-earth (RE) ions such as  $\text{Eu}^{2+}$ , an increase in luminescence output can be achieved by additional doping with barium halides and post-annealing of the "as-poured" glass to form barium halide nanocrystals in the glass matrix, which partially incorporate some of the RE ions. The small nanocrystal sizes of a few hundred nanometers allow even

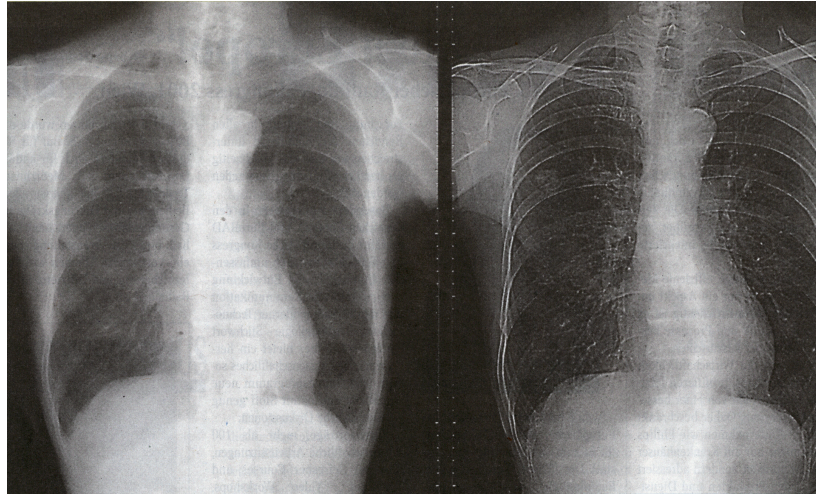


Figure 1: Chest radiographs obtained with computed radiography (left) and conventional screen-film radiography (right) [1].

smaller phonon frequencies for some REs, leading to enhanced fluorescence efficiencies of the glasses [8–10]. Today, such glass systems already provide good quality images as shown in Ref. [3]. In Ref. [6] it was shown that an increase in luminescence by a factor of 2 would lead to a commercially competitive image plate reducing the x-ray dose and the risk of tissue damages from irradiation, respectively.

Besides the steadily growing demands of the industry, research and development of such image plates are also subject to economic fluctuations. Currently, there is a serious shortage of rare-earth minerals; Beijing cut its export quotas by 72% in the latter half of 2010 and by a further 35% during the first half of 2011 in an effort to ostensibly address its environmental problems. Whatever the reason, China has doubled or, in some cases, tripled the cost of rare-earth materials in recent times and a crisis is predicted to be reached in 2014 and 2015 [11]. China has about one-third of the global rare-earth deposits but produces around 95% of the world's supply. The RE portion of the image plate is, therefore, the most expensive part,  $\text{Eu}^{2+}$  being particularly costly. One chance to overcome this problem is the synthesis of the more expensive  $\text{Eu}^{2+}$  by melting the cheaper trivalent  $\text{Eu}^{3+}$  raw material [12–14]. The investigation of such a conversion and its limits are also a substantial point of interest in this work.

The main objective of this thesis is to increase the luminescence efficiency of the studied glass systems by optimizing the  $\text{Eu}^{2+}$  doping level, the luminescent nanoparticles, as well as by tailoring the properties of the glass matrix system itself. The obtained glasses and glass ceramics are not limited to medical imaging applications, but also show huge potential as precise x-ray fiber dosimeters for applications in the human body or in other light converting systems like down- or up-converting glass-ceramic layers for high efficiency solar cells [15–18].

In Chapter 2 the theoretical physical background as well as the different experimental measurement techniques used for this work are briefly presented and explained. Chapter 3 describes the influence of a glass remelting step and the addition of indium as reducing agent on the nanoparticles. The effect of multivalent Eu doping on the crystallization of barium chloride ( $\text{BaCl}_2$ ) nanoparticles is discussed in Chapter 4. X-ray absorption near edge structure (XANES) and x-ray diffraction (XRD) investigations were performed to evaluate the accurate  $\text{Eu}^{2+}$ -to- $\text{Eu}^{3+}$  ratios, as well as the produced corresponding crystal phases. Chapter 5 deals with RE co-doping as another attempt to enhance light output by a possible energy transfer between the RE dopants, while a different approach with another glass host system, namely borate glasses, is investigated in Chapter 6. Chapter 7 gives a short introduction into preliminary work on using luminescent glasses and glass ceramics as radiation detection fibers.

Finally, the most significant results of this work are summarized in Chapter 8, and an outlook for future trends is given in Chapter 9.



## PHYSICAL BACKGROUND

In the following sections the physical background, as well as the different measurement techniques used for this work, will be presented and explained.

### 2.1 X-RAY STORAGE PHOSPHORS

An x-ray storage phosphor absorbs and down-converts ionizing radiation like x- or  $\gamma$ -rays (high energetic photons) into visible luminescence. Storage phosphors can store the energy in meta-stable electron-hole (e-h) pairs which are trapped in localized defects with energies lying in the bandgap between conduction and valence band (see Fig. 2, left). In halide crystals, the electron trap centers are color centers (F centers), while the hole trap centers are activator holes ( $A^+$ ). Storage times up to several hours are possible. Photostimulation with a laser leads to recombination of the charge carriers via direct tunnel recombination to an excited state of the activator ( $A^0$ )\* or via excitation into the conduction band followed by a recombination to the excited state of the activator where it then recombines with the activator hole  $A^0$  by emitting trapped e-h pair density dependent luminescence (see Fig. 2, right).

Requirements for a good storage phosphor are a high x-ray absorption, high light output, low afterglow and a well separated stimulation and emission range. In addition, the emission must match the range of high detector quantum efficiency and the material transmission for both emission and stimulation light must be high. The stored image must be stable for several hours (low fading

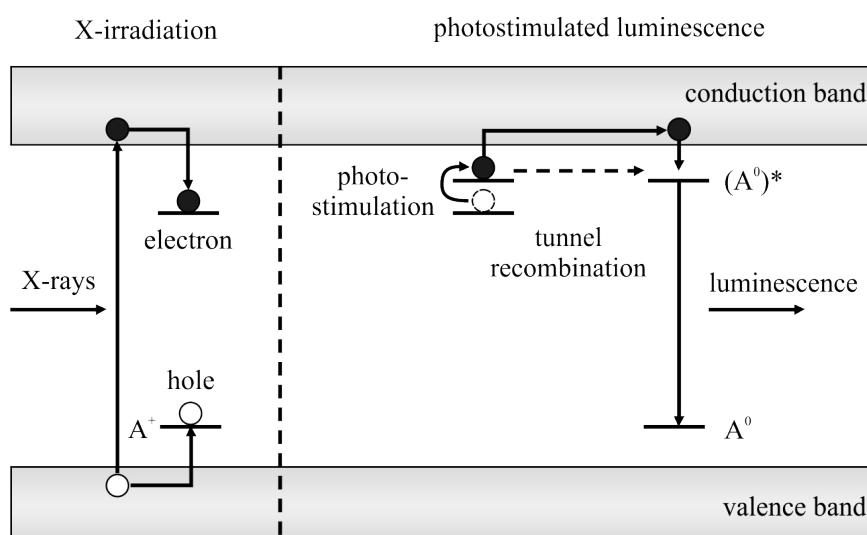


Figure 2: Schematic energy band model for storage (left) and read-out (right) mechanism.

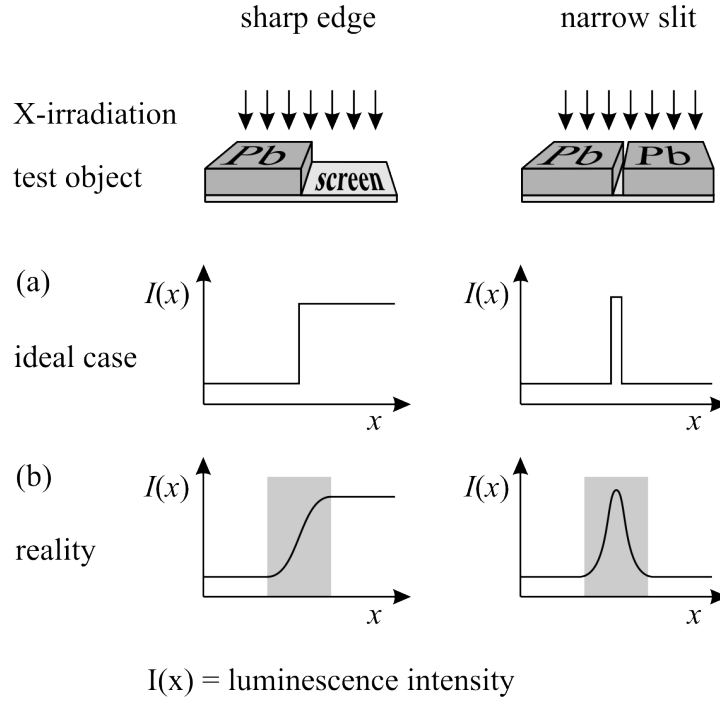


Figure 3: Ideal and real imaging of an infinitely sharp edge (left) and a narrow slit (right) by an x-ray storage phosphor imaging system [2].

between exposure and read-out) and the material must be reusable after read out or optical erasure [19, 20].

Up to now, the worldwide most used x-ray storage phosphor for medical imaging and other x-ray applications is barium fluoride bromide (BFB) doped with  $\text{Eu}^{2+}$  [21]. Providing a high x-ray absorption coefficient and high conversion and stimulation efficiency, BFB is still the reference for all other storage phosphors. For this work a commercially available  $\text{BaFBr}:\text{Eu}^{2+}$  (1000 ppm) was used for comparison.

### 2.1.1 Spatial Resolution

In addition to the above mentioned requirements for a good storage phosphor, the spatial resolution is also an important factor for resolving small structures like bone fractures with digital radiography. In order to understand the limitations in resolution, Fig. 3 shows a comparison of the image sharpness of an infinitely sharp edge and an infinitely narrow slit by an ideal and real x-ray storage phosphor imaging system [2]. In case of an infinitely sharp edge as original image, an ideal system should show a sharp step in the detected luminescence intensity from zero to an absorbed x-ray dose proportional intensity level (Fig. 3a, left). Changing the original image to an infinitely narrow slit, the system should show an infinitely small square function (Fig. 3a, right). However, this is not the case in reality, where the luminescence intensity shows a sigmoidal increase for the sharp edge (Fig. 3b, left) and a bell-shaped intensity curve for the narrow slit (Fig. 3b, right). The image sharpness of the system is given by the half width of this curve.

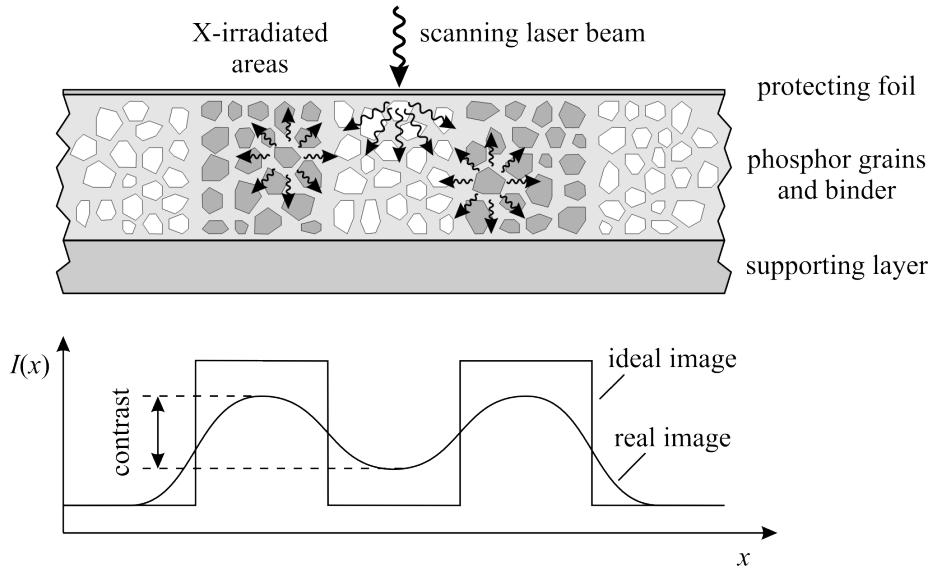


Figure 4: Illustration of the read-out laser beam scattering of a storage phosphor image plate (top) and the effect on the luminescence intensity distribution (bottom) [2].

Another common way to classify the resolving power of an x-ray imaging system is the use of the modulation transfer function (MTF). It describes the decrease of the image contrast with higher spatial frequencies or the frequency in space of equally spaced parallel lines, respectively. Therefore, the highest spatial resolution is obtained for the smallest detectable contrast. Detailed theoretical calculations and further information on the MTF are given in Ref. [2].

Compared to scintillator screen-film detectors ( $\approx 5$  line pairs/mm), conventional BaFBr:Eu<sup>2+</sup> x-ray storage phosphor screens have an inferior spatial resolution ( $\approx 3$  line pairs/mm). Figure 4 shows a main reason for this. The scanning read-out laser beam is scattered by the storage phosphor layer due to the different refractive indices of the phosphor grains and the organic binder of the image plate [2]. These scattered photons can excite trapped e-h pairs in areas away from the laser beam position. The global luminescence detection leads to a spread of the sharp edges, a reduced contrast modulation and thus a reduced spatial resolution. Storage phosphors based on glasses and glass ceramics can minimize this scattering effect, because they are grainless. However, Section 2.4 will show, that some other considerations must be taken into account, when a glass host matrix is chosen.

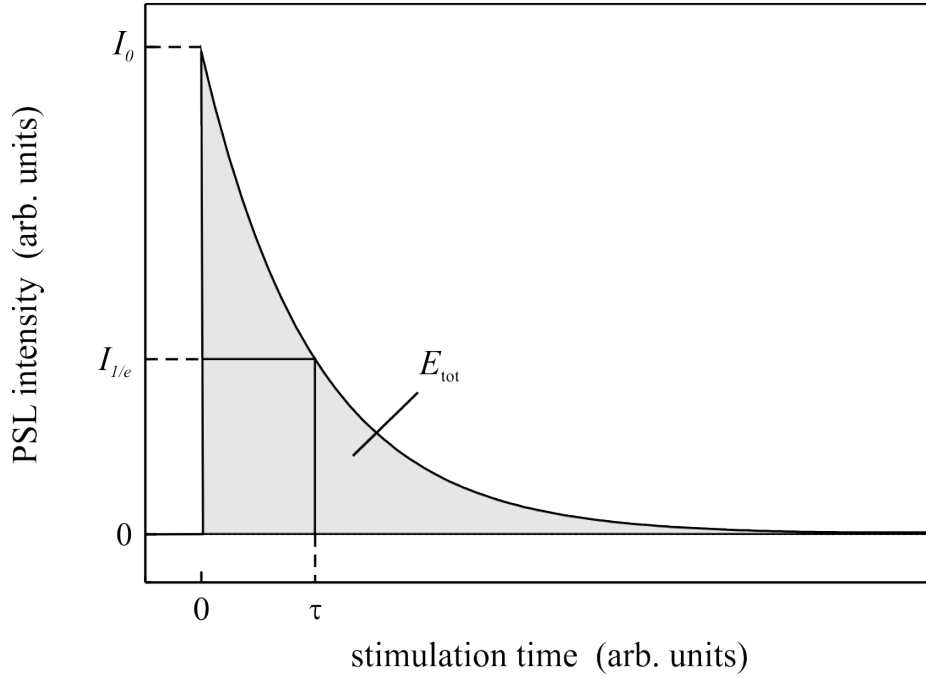


Figure 5: Mono-exponential PSL decay curve of an x-ray storage phosphor under continuous stimulation.

### 2.1.2 Photostimulated Luminescence

#### Fundamentals

Once having stored energy within a storage phosphor (see Section 2.1), the energy can be released by stimulation with appropriate visible light producing photostimulated luminescence (PSL). The continuous stimulation leads to a PSL intensity decay, because the number of PSL-active centers decreases over time. This time dependence follows a mono-exponential decay

$$I(t) = I_0 \cdot \exp(-t/\tau) \quad (1)$$

with the maximum PSL intensity,  $I_0$ , at the beginning of the measurement, the stimulation time  $t$  and the time constant  $\tau$  which depends on the power  $P$  of the stimulation light and the lifetime of the activator luminescence and is defined as the time after which the PSL intensity is decreased to  $1/e$  of its initial value. Such a bleaching-curve is shown in Fig. 5. The area below the curve corresponds to the released photon energy,  $E_{\text{tot}} = I_0 \cdot \tau$ , which is proportional to the absorbed x-ray dose  $D$ . Excluding the dose the conversion efficiency (CE) achieved is [2]:

$$\text{CE} = \frac{I_0 \cdot \tau}{D} \quad (2)$$

The required energy to reduce the PSL intensity to  $1/e$  of its initial value is called stimulation energy (SE) and given by

$$\text{SE} = \tau \cdot P. \quad (3)$$

The ratio CE/SE gives the sensitivity of an x-ray storage phosphor.

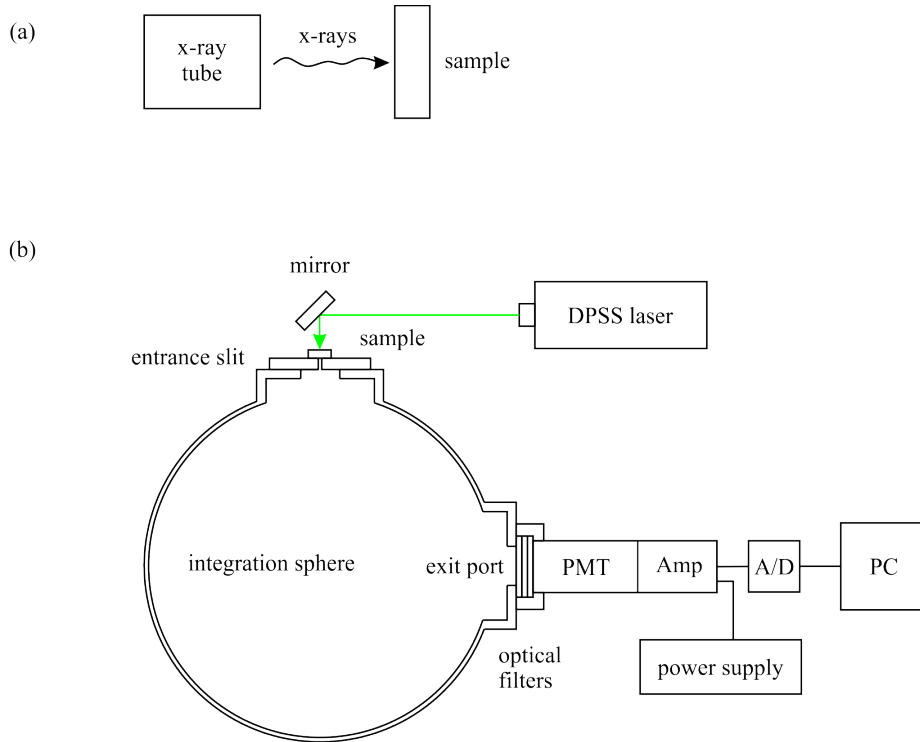


Figure 6: Schematic photostimulation experiment. (a) Exposure of the sample with x-rays. (b) Stimulation of the sample with 532 nm laser light and detection via photomultiplier tube [22].

### Experimental Details

The PSL measurements on the glass ceramics were performed at SUNY-Stony Brook, NY, USA. They consist of an initial exposure of the samples with x-rays of a specific dose (here about 320 mR) to generate e-h pairs (see Fig. 6a). The x-ray absorption of the samples was above 90%. In Fig. 6b the read-out scheme is shown. The e-h pairs were stimulated with a 532 nm diode-pumped solid state (DPSS) laser from *Coherent* which was pumped with a wavelength of 810 nm. An appropriate highpass filter was used to reduce the intensity. The remaining constant offset signal was subtracted from the data, before analyzing. The sample port has a 3 mm hole. The exit port is followed by 3 filters to cut out the respective  $\text{Eu}^{2+}$  emission. The signal was detected with a R6095 photomultiplier tube from *Hamamatsu*, which is operated at 700 V.

## 2.2 PHOTON CONVERSION PROCESSES

### 2.2.1 General Processes

In the previous section, the down-conversion of high energetic photons like x- or  $\gamma$ -rays was briefly introduced. This work focuses on the adjustment and optimization of this effect and its efficiency. It is an umbrella term for the down-shifting and quantum cutting processes. Down-shifting, also known as photoluminescence (PL) describes the conversion of a high energetic photon into one lower energetic photon. Therefore the high energetic photon is absorbed

from a luminescent center, for example a Eu ion, which hence is excited from the ground state into a higher energetic state. Relaxing back to the ground state, the ion releases its energy by emitting a photon with the same or lesser energy, with the remaining energy absorbed by the crystal lattice and phonons, respectively.

While down-shifting is the observed and investigated process in this work, a higher photon-conversion efficiency is reached in the case of quantum cutting, where a high energetic photon is converted into two or more lower energy photons. Here, several conversion routes are possible including different intermediate states and different ions located close enough to one another to allow energy transfer between them.

For the sake of completeness, the up-conversion process describes the effect of two low-energy photons, for example infrared (IR) photons, becoming sequentially absorbed by a RE ion followed by an emission of a high energy photon in the visible spectral range. The absorption depends mainly on the intermediate level lifetime of the RE ions, which itself depends on the phonon energies of the host material, in particular, decreasing phonon energies lead to a more improbable non-radiative recombination.

### 2.2.2 Photoluminescence

#### *Fundamentals*

This section will briefly discuss the radiative return of a light excited luminescent system to the ground state for the case of low luminescent center concentration and a non-absorbing host material. Figure 7 shows a configurational coordinate diagram with energy parabolas of the system for ground and excited state as a function of a configurational coordinate which describes one of the vibrational modes of the luminescent center. A broad absorption band excites it in a high vibrational level of the excited state, where it then relaxes non-radiatively to the lowest level by transferring its excess energy to phonons or the host lattice, respectively. The relaxation can also be described as a position adjustment of the nuclei to the new excited state for which the interatomic distances change to the equilibrium distances of the excited state. As a consequence thereof, the configurational coordinate changes by  $\Delta R$ . The system then returns spontaneously to a high vibrational level of the ground state along with the emission of radiation. From here it relaxes non-radiatively back to the lowest level. The relaxation processes are the reason for the lower energy emission and the so called Stokes shift of the emission band, which is given by the energy difference between the maximum of the lowest excitation and emission level. The shift increases and the optical bands broaden with larger value of  $\Delta R$ . In case of RE ions, which are explained later on in this chapter, the emission transition goes from a 5d or 4f orbital to the 4f orbital.

Photoluminescence (PL) is the general heading for fluorescence and phosphorescence, which are distinguished by their respective decay time; the time in which the PL intensity decreases to  $e^{-1}$  of its initial value: While fluorescence

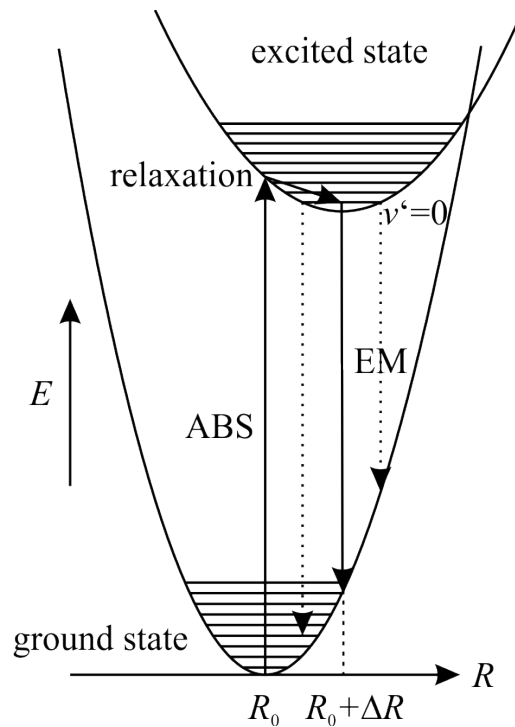


Figure 7: Configurational coordinate diagram (reproduced from [23]). After absorption transition from the ground to the excited high vibrational levels the system relaxes to the lowest vibrational level  $v'=0$  from where a broad band emission occurs. The parabola offset is given by  $\Delta R$ .

decay times are lying under  $10^{-4}$  s, phosphorescence can have decay times from milliseconds up to several hours due to metastable energy levels working as charge carrier traps (see Section 2.1).

### Experimental Details

PL measurements were done at room temperature with a *Fluorolog-3* from *HORIBA Jobin Yvon*. A 450 W xenon lamp combined with a double-grating excitation monochromator was used as the excitation source. The monochromator allows a narrow band of wavelengths of light to reach the sample, which is fixed on a sample holder inside the sample compartment module. The response of the sample or emitted radiation, respectively, was filtered by a single-grating emission monochromator and then was detected by a *R928P* photomultiplier tube for high sensitivity in photon-counting mode (185-900 nm). For the monochromators a 500 nm blaze grating with 1200 lines per mm was used for emission (working range:  $2/3 \cdot \text{blaze}$  to  $5/3 \cdot \text{blaze}$ , i.e. 333 nm to 833 nm) with an accuracy of 0.5 nm. A PL spectrum was produced by stepping one monochromator through a wavelength region, while recording the PL intensity as a function of wavelength. In the case of driving both monochromators, 3D PL maps were obtained.

## 2.3 RARE-EARTH IONS

### 2.3.1 *General characteristics*

Scandium, yttrium and the lanthanides and actinides of the periodic table of elements are called rare earths (REs). The elements are not as rare as their name suggests. For example thulium, the rarest RE element, is more abundant than gold. A characteristic of RE ions is the incompletely filled 4f shell of the ion, which is shielded by the surrounding filled 5s<sup>2</sup> and 5p<sup>6</sup> orbitals with larger radial extension [23]. Therefore the host lattice or phonons have a relatively small influence on the optical transitions inside the 4f<sup>n</sup> configuration.

The parity selection rule forbids optical absorption transitions, but can be partially circumvented by uneven components of the crystal field due to an occupation of a crystallographic site without inversion symmetry by a RE ion. The wave functions of the 5d and 4f shells can then be mixed and the nominal forbidden 4f-4f transition shows spectral intensity. Two transition mechanisms with broad absorption bands become partially allowed:

Charge-transfer transitions ( $4f^n \rightarrow 4f^{n+1}L^{-1}$ , L=ligand) are found for tetravalent RE ions like Ce<sup>4+</sup>, Pr<sup>4+</sup> and Tb<sup>4+</sup>, which like to be reduced [24]. Trivalent ions with a tendency to become divalent like Sm<sup>3+</sup>, Eu<sup>3+</sup> and Yb<sup>3+</sup> show charge-transfer transition absorption bands in the UV.

$4f^n \rightarrow 4f^{n-1}5d$  transitions are found for divalent ions like Sm<sup>2+</sup> in the visible region and for Eu<sup>2+</sup> and Yb<sup>2+</sup> in the long wavelength UV, which like to be oxidized. It is also found that trivalent ions with a tendency to become tetravalent like Ce<sup>3+</sup>, Pr<sup>3+</sup> and Tb<sup>3+</sup> also follow 4f-5d transitions with bands absorbing in the UV.

### 2.3.2 *Europium*

Most of the samples produced in this work were doped by Eu, which can occur in divalent (Eu<sup>2+</sup>) and trivalent (Eu<sup>3+</sup>) valence states. Eu is one of the most reactive lanthanides with atomic number 63 (period 6, orbital block f in the periodic table of the elements). Fast oxidation of Eu<sup>2+</sup> to Eu<sup>3+</sup> in ambient atmosphere makes a nitrogen atmosphere during the glass preparation essential. Also water must be kept away due to Eu reacting with hydroxide ions that might be present. When excited with ionizing radiation like x-rays or ultraviolet (UV) light Eu<sup>2+</sup> is luminescent in a wide optical spectral range from UV to the red spectrum depending on the host lattice structure. Eu<sup>3+</sup> shows less intense luminescence and it is therefore important for this work to have the maximum amount of Eu<sup>2+</sup> inside the glass. A more detailed introduction to the optical properties of both valence states is given in the following sections.

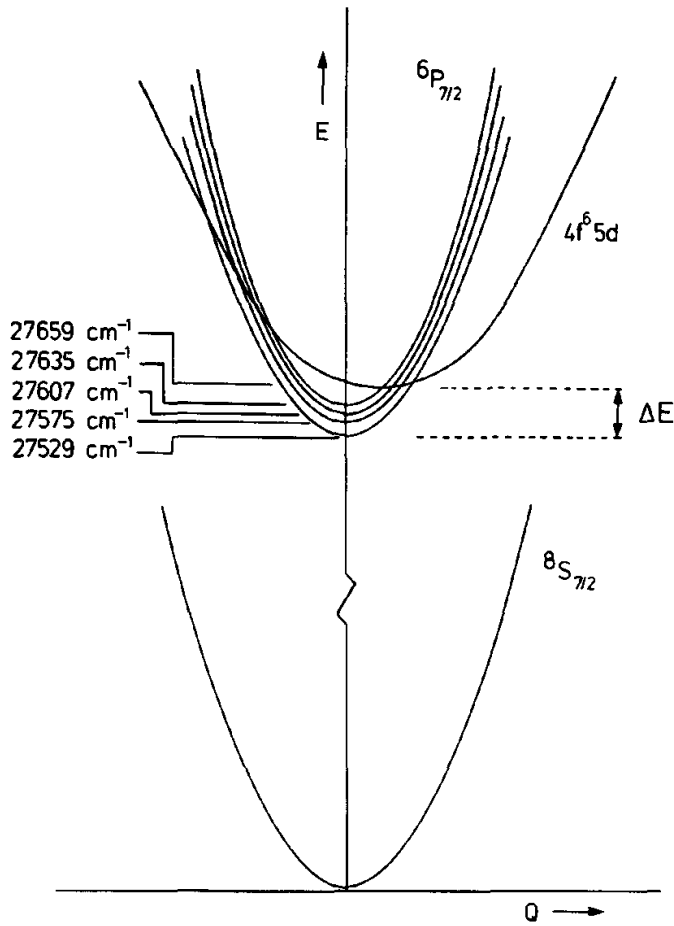


Figure 8: Configurational coordinate model for  $\text{Eu}^{2+}$  in  $\text{SrB}_4\text{O}_7$  [23].

### Divalent Europium

$\text{Eu}^{2+}$  ( $4f^7$ ) shows a broad band emission due to a relaxing electron from a 5d orbital to the 4f orbital. This  $5d \rightarrow 4f$  emission between the crystal field components of the  $4f^65d$  configuration and the  $^8S_{7/2}$  ground state from  $4f^7$  can vary from long-wavelength UV to yellow with normal decay times about  $1 \mu\text{s}$  [23]. The optical transition rate is slowed down by the spin selection rule, because the emission level contains spin octets and sextets, while the ground state level is an octet. The decay time can be even further decreased to the nanosecond regime when the  $\text{Eu}^{2+}$  is embedded into  $\text{BaCl}_2$  nanocrystals [10]. In addition, also the emission energy depends on the host lattice and crystal field coupling, respectively. A weak crystal field could lead to a shift of the lowest  $4f^65d$  level above the  $^6P_{7/2}$  level of the  $4f^7$  configuration and would result in a sharp-line emission due to the  $^6P_{7/2} \rightarrow ^8S_{7/2}$  transition. An example is shown in Fig. 8 for  $\text{Eu}^{2+}$  in  $\text{SrB}_4\text{O}_7$  [23]. However, for fluorochlorozirconate (FCZ) glasses the coupling is high, the  $4f^65d$  level is shifted below the  $^6P_{7/2}$  level and therefore broad emission bands occur.

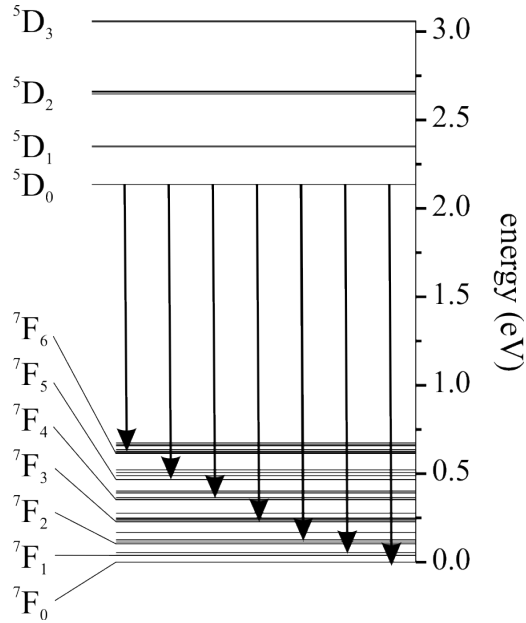


Figure 9: Possible emission lines corresponding to the  ${}^5D_0 \rightarrow {}^7F_J$  ( $J=0, 1, 2, 3, 4, 5, 6$ ) transitions of  $Eu^{3+}$ . The energy level diagram corresponds to data of Ref. [25, 26].

### Trivalent Europium

$Eu^{3+}$  ( $4f^6$ ) shows emission lines in the red spectral range corresponding to electron transitions from the excited state  ${}^5D_0$  to the  ${}^7F_J$  ( $J=0, 1, 2, 3, 4, 5, 6$ ) levels of the  $4f^6$  configuration (see Fig. 9). In addition to these  ${}^5D_0 \rightarrow {}^7F_J$  transitions, emissions from the higher  ${}^5D$  states are also possible. Often, a splitting of the emission lines is observed, which corresponds to the crystal-field splitting of the  ${}^7F_J$  states. The  ${}^5D_0$  level shows no splitting, because the total angular momentum quantum number  $J$  is zero. As mentioned before, the parity selection rule forbids optical electric-dipole transitions between levels of the  $4f^n$  configuration. Instead, magnetic-dipole transitions with  $\Delta J = 0, \pm 1$ , except  $J = 0$  to  $J = 0$ , or vibronic electric-dipole transitions can occur with less intensity. The parity selection rule can be partially abolished by uneven crystal field components if no inversion symmetry is present at the crystallographic site at the  $Eu^{3+}$  ion. Forced electric-dipole transitions with  $\Delta J = 0, \pm 2$ , for example the  ${}^5D_0 \rightarrow {}^7F_2$  transition, are hypersensitive to these deviations from inversion symmetry and show intense optical emission lines.

## 2.4 MATRIX MATERIALS

Having chosen a luminescent RE for a desired application an important step is the selection of the host material. In this section the glass hosts, their advantages and their preparation methods are briefly described.

## 2.4.1 ZBLAN

In 1974 Poulain and Lucas discovered heavy metal fluoride glasses (HMFG) at the University of Rennes in France [27]. ZBLAN is an abbreviation for glasses that are made of a mixture of zirconium, barium, lanthanum, aluminum, and sodium fluorides. The standard ZBLAN composition introduced by Ohsawa and Shibata [28] is known for its lowest critical cooling rate among the FZ glasses [29]. Compared with silicate glasses, ZBLAN has extended transparency into infrared wavelengths and a multi-phonon edge shift to longer wavelengths, due to heavier ions making it useful for ultra-low loss optical fibers [30].

*Sample preparation*

The predominantly used ZBLAN glass compositions for three different series are listed in Table 1. The glasses of the multivalent Eu and co-doping series were prepared under an argon atmosphere inside a glove box by a two-step melting

Material	Indium			Multivalent Eu	Co-Doping
	Series	Series	Series	Series	Series
ZrF <sub>4</sub>	51.2	52.5	51.0	51.0	51.0
BaF <sub>2</sub>	9.7	9.7	9.6	-	-
BaCl <sub>2</sub>	-	-	-	20.0	20.0
LaF <sub>3</sub>	3.9	3.9	3.9	3.5	3.5
AlF <sub>3</sub>	2.9	2.9	2.9	3.0	3.0
NaF	-	-	-	20.0	20.0
NaCl	19.4	19.4	19.2	-	-
InF <sub>3</sub>	-	0.5	1.0	0.5	0.5
EuF <sub>2</sub>	3.0	3.0	3.0	-	-
EuCl <sub>2</sub>	-	-	-	x	1.0
EuCl <sub>3</sub>	-	-	-	2.0-x	-
RECl <sub>3</sub>	-	-	-	-	1.0

Table 1: Nominal composition of the ZBLAN glasses for the indium (left), the multivalent Eu (middle) and the co-doping series (right) (values in mol%). For the co-doping series the trivalent REs are RE=Gd<sup>3+</sup>, Nd<sup>3+</sup>, Tb<sup>3+</sup> and Yb<sup>3+</sup>.

process. The first step involves mixing and melting of all fluorides at 800 °C for 60 minutes in a platinum crucible. After being cooled to room temperature chlorides are added to the melt and the whole composition is remelted for 60 minutes at 745 °C. The glasses of the indium series were one-step melted (with both fluoride and chloride compounds) in a glassy carbon crucible at 745 °C in an inert atmosphere of nitrogen. The final step for every glass involves pouring into a 200 °C hot brass mold, where it stays for 60 minutes before being cooled to 25 °C room temperature over 4 hours.

The glasses are additionally doped with chlorine ions by adding barium chloride or a mixture of barium fluoride and sodium chloride. This enables precipitation of barium chloride nanocrystals within the glass upon appropriate annealing. Depending on the structural phase of the barium chloride, the glass-ceramic material can act either as a scintillator (able to convert ionizing radiation to visible light) [4] or as a storage phosphor (able to convert the radiation into stable electron-hole pairs, which can be recombined at a later time with a scanning laser beam) [6]. More information is given in Section 2.4.3.

#### 2.4.2 Borate Glasses

Borate glasses are known as highly optical transparent, robust and inexpensive matrix materials for fluorescent ions. These characteristics make them attractive for many applications; an example is the usage for spectral down-conversion glasses for photovoltaic applications [31]. In this work lithiumchloroborate (LCB) glasses are investigated as a host material for luminescent  $\text{Eu}^{2+}$  ions incorporated into  $\text{BaCl}_2$  nanocrystals.

##### *Sample preparation*

The nominal lithium borate glass composition is  $53\text{B}_2\text{O}_3\text{-}24\text{Li}_2\text{O}\text{-}5\text{LiF}\text{-}3\text{SiO}_2\text{-}14\text{BaCl}_2\text{-}1\text{EuCl}_2$  (values in mol%). Silicon and boron are network formers, whereas lithium acts as a network modifier to loosen up the network lowering the melting temperature and melt viscosity.  $\text{B}_2\text{O}_3$  forms a random network, in which the boron coordination is partly triangular and partly tetrahedral [32]. It is melted at 500 °C for 60 minutes in a platinum crucible under argon atmosphere inside a glove box. Then the crucible is removed and the other compounds added. The whole composition is remelted for 60 minutes at 1020 °C and then poured into a hot brass mold before being cooled to room temperature at 50 °C per hour. Three different mold temperatures are evaluated, 100, 200 and 300 °C. It turns out even the lowest mold temperature is not sufficient to prevent a rapid crystallization of the  $\text{BaCl}_2$  - resulting in a completely ceramized glass.

#### 2.4.3 Barium Chloride

The additional barium chloride doping enables precipitation of  $\text{BaCl}_2$  nanocrystals within the glasses upon appropriate thermal treatment. These nanocrystals offer even lower maximum phonon energies (around  $200\text{ cm}^{-1}$  [35]) compared

symmetry	structure type	space group	$a$	$b$	$c$
			(Å)	(Å)	(Å)
orthorhombic	PbCl <sub>2</sub>	$Pnma$ (62; $D_{2h}^{16}$ )	7.88	4.73	9.42
hexagonal	anti-Fe <sub>2</sub> P	$P\bar{6}2m$ (189; $D_{3h}^3$ )	8.07	8.07	4.62

Table 2: Structure parameters for bulk orthorhombic and hexagonal BaCl<sub>2</sub> [33].

to the glass matrix host (590 cm<sup>-1</sup> for an FZ glass [36]) as well as the storage phosphor properties. Depending on the annealing conditions two barium chloride phases are obtained in the glass ceramics. Firstly, at temperatures around 250 °C to 270 °C, nucleation and growth of the metastable hexagonal  $P\bar{6}2m$  (space group 189;  $D_{3h}^3$ ) BaCl<sub>2</sub> phase occur. With higher temperatures the crystals grow and around 280 to 290 °C with a phase transition to orthorhombic crystal structure  $Pnma$  (space group 62;  $D_{2h}^{16}$ ) occurring, the thermodynamic system will go over in its state of lowest energy. Note, the given temperatures depend on glass composition and preparation method.

The structure type and lattice parameters for both phases are summarized in Table 2 and shown in Fig. 10 [34]. The orthorhombic unit cell contains four BaCl<sub>2</sub> molecules, while the hexagonal cell contains three formula units (three Ba and six halide atoms). A Ba<sup>2+</sup> ion has nine neighboring Cl<sup>-</sup> anions in a tri-capped trigonal prism configuration; with three halide ions lying in the same crystallographic plane, three lying in a plane in front and three behind the projection plane in Fig. 10.

In the case of single crystals, there are also two other phases available under certain conditions: a cubic form stable at a temperature range from 925-960 °C which gives a complete conversion to orthorhombic phase; this is only possible via a 200 °C heat treatment for 2 days [37]. A monoclinic form is built under high pressures [37, 38].

## 2.5 ADDITIONAL EXPERIMENTAL METHODS

### 2.5.1 X-Ray Absorption Near Edge Structure

#### *Fundamentals*

Looking at the attenuation of x-rays after being transmitted through a material, oscillatory variations of the x-ray absorption occur for photon energies beyond the binding energy of some core levels of an atom in the material. A schematic representation of such transmission measurements with the resulting x-ray absorption spectrum is shown in Fig. 11a. The abrupt increase in the absorption coefficient,  $\mu$ , is also called the absorption edge. Atoms in a molecule or condensed phase show a variation of  $\mu$  or a fine structure above the absorption edge called edge x-ray absorption fine structure (EXAFS), which can extend up to 1 keV above the edge with amplitudes up to a few tenths of the edge jump [39].

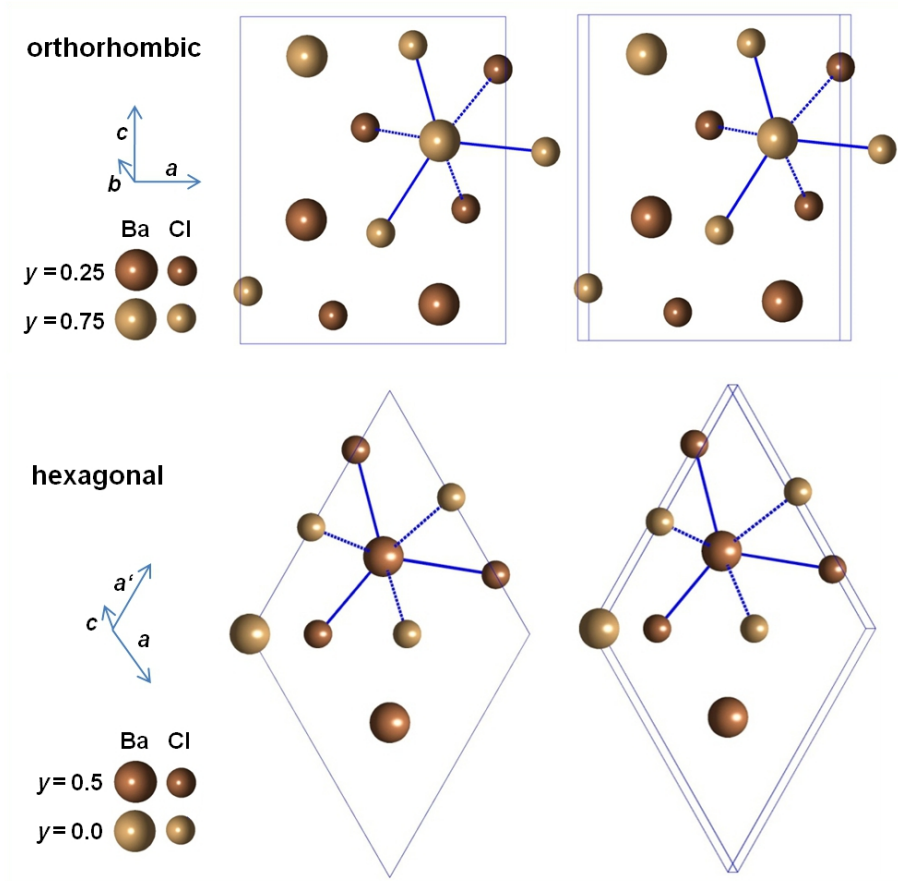


Figure 10: Stereo view of atom positions and unit cells of BaCl<sub>2</sub> in orthorhombic (top) and hexagonal symmetry (bottom). The *y* numbers in the legends are the altitudes in the projection plane [34].

The X-ray absorption near edge structure (XANES) regime, also known as near edge x-ray absorption fine structure (NEXAFS) for soft x-ray absorption spectroscopy (energies less than 1000 eV), lies in between the pre-edge and the EXAFS region, typically from 5 eV up to 150 eV beyond the absorption edge. The low photoelectron energies lead to effects such as many-body interactions and dominant multiple scattering by neighboring atoms giving information about the vicinity of the investigated atoms. Figure 11b shows the excitation of a photoelectron after absorbing an x-ray photon. The photoelectron can be described as a spherical wave with the wavelength  $\lambda = 2\pi/k$  where  $k$  is given by

$$k = \sqrt{\frac{2m_e}{\hbar^2} (h\nu - E_0)} \quad (4)$$

with the incident photon energy,  $E = h\nu$ , the threshold energy of the absorption edge,  $E_0$ , electron mass  $m_e$  and the Planck's constant  $\hbar$ . The photoelectron can be backscattered from neighboring atoms producing a wave which can interfere constructively or destructively with the outgoing wave, resulting in oscillatory variations of the x-ray absorption. The frequency and amplitude of these oscillations depends on the distance and type of neighboring atom to the

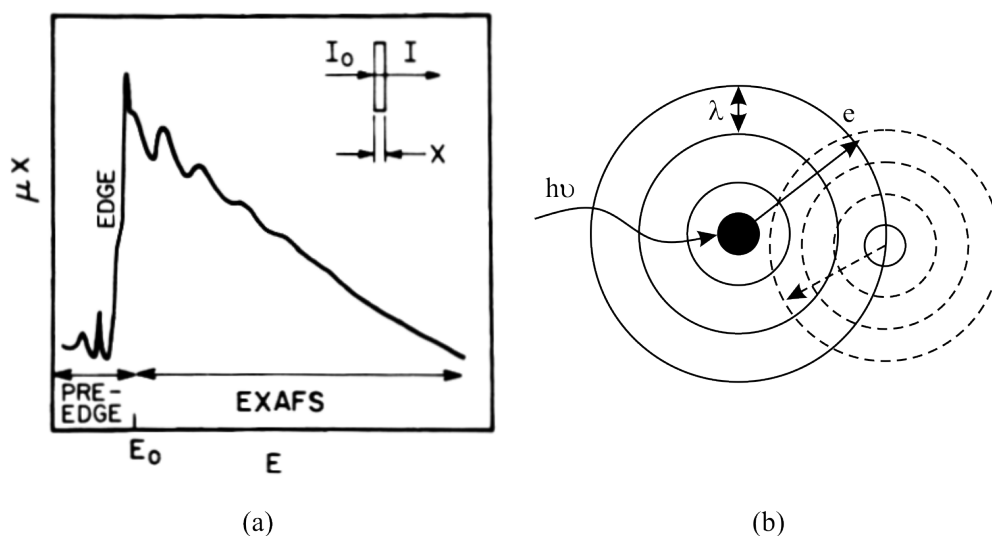


Figure 11: (a) Schematic EXAFS spectroscopy measurement and corresponding x-ray absorption spectrum [39]. (b) Scattering from the outgoing photoelectron from a neighboring atom.

absorbing atom and thus can also distinguish between the different valencies, including divalent and trivalent Eu for this work.

#### *Experimental Details*

The x-ray absorption near-edge structure (XANES) experiments on the multivalent Europium series were performed at the bending magnet beamline 5-BM-D (DuPont-Northwestern Dow Collaboration Access Team, DND-CAT) at the Advanced Photon Source (Argonne National Laboratory, USA). The spectra were recorded in the vicinity of the Eu  $L_{III}$ -edge (6977 eV [40]). To suppress higher harmonics of the fundamental energy, the crystals of the Si(111) double crystal monochromator were continuously detuned to about 70% of the maximum peak intensity of their rocking curve. The monochromator was calibrated using the Fe K-edge (7112 eV [40]). XANES spectra were recorded in fluorescence mode using an energy dispersive 4-pixel silicon drift detector (SDD) (Vortex-ME4, SII NanoTechnology USA Inc.). The region of interest was set to include the  $\text{Eu}^{2+}$  and  $\text{Eu}^{3+}$   $L_{III}$  emission lines only. The incident photon flux was measured by means of an Oxford IC Spec ionization chamber filled with a gas mixture of He (600 torr) and  $\text{N}_2$  (160 torr).

The experiments on the co-doping and borate series were performed at the A1 EXAFS beamline at the DORIS III which operates as a synchrotron radiation source for HASYLAB (Deutsches Elektronen-Synchrotron DESY, Germany). It uses a 1/2 demagnified focused beam to provide high flux density in the working range 2.4 - 8.3 keV. A Si(111) double crystal monochromator with nickel coated mirrors was used. The crystals were continuously detuned to about 70% of the maximum peak intensity of their rocking curve to absorb higher harmonics. Again, the monochromator was calibrated using the Fe K-edge. XANES spectra were recorded in fluorescence mode using an energy dispersive 7-pixel

silicon drift detector (SDD) (DESY FEC / PN sensors, Munich). The ionization chamber was filled with N<sub>2</sub> (570 torr).

For each single XANES spectrum, background correction, normalization and curve fitting were performed individually with WinXAS 3.0 [41]. The pre-edge background fluorescence was subtracted from the raw data by approximating a linear function. This was followed by normalization of the edge jump to unity. Each corrected spectrum was fitted with two pseudo-Voigt functions and two arc tangent functions in order to account for the white line (WL) resonances and the electron excitation into unbound states. The width of both arc tangent functions, however, was kept constant for each XANES spectrum and set to the natural Eu L<sub>III</sub> line width of 3.91 eV [42]. The residual degrees of freedom of the fit, in particular the position of the pseudo-Voigt function and the height of the arc tangent function, was obtained as a result of the fitting process. To quantify the WL intensities of both europium oxidation states, the area of each peak function was calculated based on the resulting fit parameters.

### 2.5.2 X-Ray Diffraction

#### *Fundamentals*

When x-rays interact with a crystalline material, a diffraction pattern of the scattered intensity is obtained depending on incident and scattering angle as well as on the photon energy. This pattern is like a 'fingerprint' of the material, making XRD an ideal non-destructive method to obtain structural information on solid matter e.g. lattice structure, crystalline defects, chemical composition, substrate orientation, mechanical stress, crystallite sizes and much more.

The x-rays are scattered at the electron shells of the atoms and induce harmonics of the electrons, which then excite secondary radiation with the frequency of the excitation radiation. Interference with neighboring scattered x-ray photons occur if the wavelengths of the incident photons are within the same range, usually on the order of a few angstroms, as the periodic distance between the scatter planes or centers, respectively. The distance, the incidence angle and the excitation wavelength determine the appearing reflections, which have maximum intensity (case of constructive interference) if two parallel incident x-rays are still in phase after being reflected at atomic planes. This is the case, when the difference in path ( $2\delta$ ) is an integral multiple number of the wavelength  $\lambda$  ( $2\delta = n \cdot \lambda$  with  $\delta = d_{hkl} \cdot \sin \theta$ ). The well-known Bragg equation then gives the interatomic spacing  $d_{hkl}$

$$n \cdot \lambda = 2 \cdot d_{hkl} \cdot \sin(\theta) \quad (5)$$

In addition to the distance between the lattice planes, mean particle sizes of nanoparticles of different phases can be estimated. This is possible due to crystal size dependent broadening effects of the reflexes, which act like impurities in the crystal lattice. However, the broadening is influenced by instrumental restrictions like resolution, natural linewidth, etc., and has to be subtracted from

the diffraction pattern first. With the assumption that the crystals are free of stress and strain, the apparent particle size can be estimated by [43]:

$$d = \frac{K \cdot \lambda}{b \cdot \cos(\theta)} \quad (6)$$

with the particle size  $d$ , the Scherrer constant  $K$  [44], the wavelength of the radiation  $\lambda$ , the additional broadening (in radians)  $b$ , and the Bragg angle  $\theta$ .  $K$  depends on the full width at half maximum of the reflex, crystal shape and the size distribution and is set to 1 due to low value variations at all low-order reflections from crystals of simple regular shapes [43].

### *Experimental Details*

XRD measurements were performed in the Bragg-Brentano focusing geometry using an *BRUKER AXS D8 Advanced Diffractometer* with a Cu tube operating at 40 kV and 40 mA. The Cu- $K_\beta$  radiation components of the primary beam were attenuated by a 20  $\mu\text{m}$  thick nickel filter. The Cu- $K_{\alpha 2}$  components were subtracted from the measured signal via the *DIFFRACplus EVA v1.2* XRD analysis software.

### 2.5.3 *Differential Scanning Calorimetry*

#### *Fundamentals*

Differential scanning calorimetry (DSC) is a precise tool to gain information on the vitrification or crystallization behavior of a sample. It measures the heat flow in and out of a sample and enthalpy changes, respectively, through a temperature comparison between sample and a reference with known heat capacity. During the heating or cooling stages, physical and chemical changes like phase transitions, evaporation or melting can occur and lead to temperature differences which are proportional to heat flow differences. It is known that some of the investigated glasses and glass ceramics containing  $\text{BaCl}_2$  show crystallization and also phase transitions when post thermal heat treated. Thus, the thermal properties of the samples were investigated with a *NETZSCH DSC 204 F1 Phoenix* instrument.

In general, the thermal stability of glasses can be described by  $\Delta T$  and the Hruby constant  $H_r$ , which are defined as

$$\Delta T = T_x - T_g \quad (7)$$

$$H_r = \Delta T / (T_m - T_x) \quad (8)$$

where  $\Delta T$  gives information about the devitrification tendency of the glass; a wider gap results from a drop in the glass viscosity.  $H_r$  introduced by Hruby [45] also takes into account the gap between melting temperature and crystallization onset, which is influenced by the magnitude of the crystal growth rate. For smaller growth rates the gap decreases.

*Experimental Details*

The samples were cut into small pieces of around 30 to 50 mg and placed in an aluminum crucible. To obtain the differential temperature, which then is converted into absorbed and radiated heat, a second empty crucible was used as a reference. To calculate thermal stability parameters and activation energies of the dopant dependent BaCl<sub>2</sub> crystallization, DSC signals were measured from room temperature to 450 °C with different heating rates of 5, 7.5, 10, 15, 20, 25, and 30 K/min. Afterwards, the measurements were analyzed with the software package *NETZSCH Proteus v4.8.5*.

Part II

THE RESULTS



## INDIUM AND REMELTING

A standard ZBLAN glass consists of the network former  $ZrF_4$ , the network modifier  $BaF_2$ ,  $LaF_3$  to prevent segregation and  $AlF_3$  and  $NaF$  to prevent nucleation and crystallization of the glass matrix. The glasses under investigation in this chapter were additionally doped with chlorine ions by partial substitution of barium fluoride by barium chloride and complete substitution of  $NaF$  by  $NaCl$  (see Table 1 for compositions). This enabled precipitation of barium chloride nanocrystals within the glass upon appropriate annealing. In both scintillator and storage phosphor applications,  $Eu$  is added to the glass for optical activation showing an intense luminescence in the blue spectral region upon excitation with ultraviolet light or x-rays. Note that  $Eu^{2+}$  does not luminesce in the glass matrix but in the  $BaCl_2$  nanocrystals [10, 46]. For this reason, the crystalline structure of the barium chloride nanoparticles is critical to potential applications, as scintillators and storage phosphors require vastly different light collection methodologies, i.e., readout mechanisms. A further additive is  $InF_3$ , whose function as an oxidizing agent is explained below.

For luminescence from these materials, the critical component is the  $Eu$ , in particular the  $Eu^{2+}$  present in the  $BaCl_2$  nanocrystals. However, PL and XANES have shown that there is always a significant amount of  $Eu^{3+}$  in the glass which reduces the performance of these systems as both scintillators and storage phosphors [4, 46]. Specifically, in Ref. [47] it was found that about half of the doped  $Eu$  exists as  $Eu^{3+}$  in the as-made FCZ sample, even though it was added as  $EuF_2$ . XANES measurements showed that one source of oxygen was found to be in the as-bought  $EuF_2$ , in which  $Eu^{2+}$  is oxidized to  $Eu^{3+}$  before and/or during glass melting. In this context, XANES gives detailed information on the electronic structure, chemical valence, and chemical composition of the embedded  $Eu$ .

The glasses containing hexagonal  $BaCl_2$  act as a scintillator while those containing orthorhombic  $BaCl_2$  act as a storage phosphor. In such a complex system, the addition of each new chemical and each change in processing affects the important  $Eu^{2+}$  luminescence efficiency and so must be systematically evaluated.

Taking a closer look at the FCZ glass melt, complex equilibria can occur between all components depending on the process temperature. In particular zirconium and indium provide a fluorine source due to reactions such as



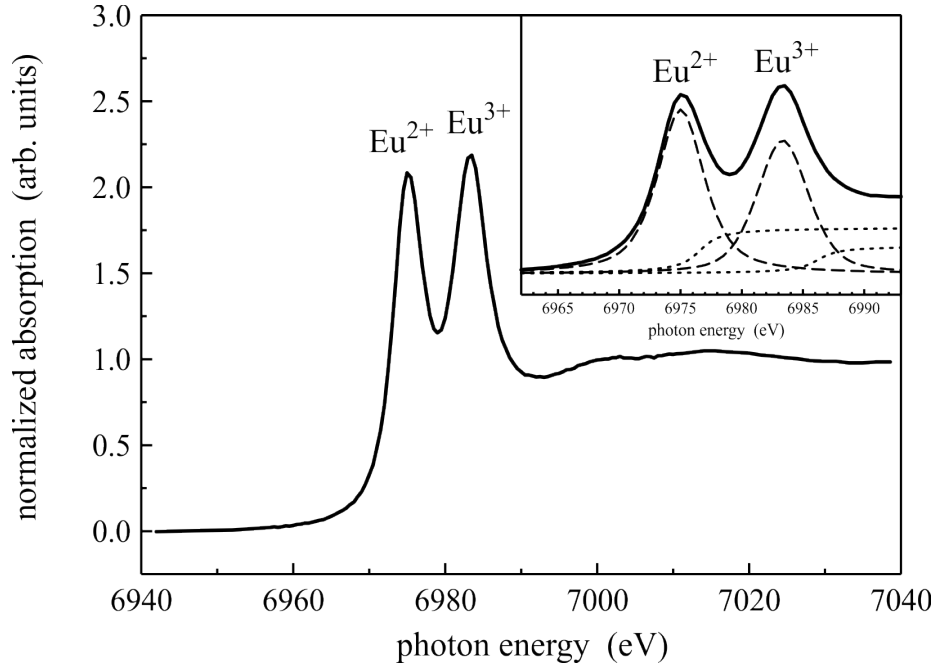


Figure 12: Normalized XANES spectra of the as-made, indium-free, Eu-doped FCZ glass. A pseudo-Voigt function (dashed curve) and an arctangent function (dotted curve) were used to fit each of the characteristic WLs of  $\text{Eu}^{2+}$  and  $\text{Eu}^{3+}$  and the absorption edge, respectively (see inset).

At processing temperatures of around  $700\text{ }^{\circ}\text{C}$ ,  $\text{ZrF}_3$  is more stable than  $\text{ZrF}_4$  [48]. Difluoride, trifluoride and tetrafluoride have free energies of formation of  $-410$ ,  $-418$  and  $-395\text{ kJ/mol}$  at  $725\text{ }^{\circ}\text{C}$  [49] leading to an equilibrium constant,  $K = \exp\left(-\frac{\Delta G_T^{\ominus}}{RT}\right)$ , of  $15.9$ , with the free energy of the reaction,  $\Delta G_T^{\ominus}$ , at the process temperature  $T = 725\text{ }^{\circ}\text{C}$ . Thus at equilibrium the concentration of  $\text{ZrF}_3$  should be around  $16$  times higher than  $\text{ZrF}_4$ . It is known, that reduced  $\text{Zr}^{3+}$  or  $\text{Zr}^{2+}$  result in black inclusions reducing glass performance [50]. However, this is not observed in the readily formed glasses doped with indium trifluoride which appear clear and transparent. Instead of using common methods like corrosive and dangerous halide gases ( $\text{SF}_6$  or  $\text{Cl}_2$ ) for an oxidizing environment [51], it appears that the reduction from  $\text{ZrF}_4$  to  $\text{ZrF}_3$  is also suppressed by the addition of a small amount of  $\text{InF}_3$  in non-dangerous nitrogen or argon working atmospheres [52]. If  $\text{Zr}^{3+}$  does form, the  $\text{In}^{3+}$  oxidizes it back to  $\text{Zr}^{4+}$ , while it is itself reduced to  $\text{In}^{1+}$  (see Equation 11). In this chapter the influence of adding  $\text{InF}_3$  and remelting on the  $\text{Eu}^{2+}$ -to- $\text{Eu}^{3+}$  mole ratio is investigated. Some text and figures have appeared previously in [14, 53].

### 3.1 X-RAY ABSORPTION NEAR EDGE STRUCTURE

Figure 12 shows the normalized Eu  $L_{\text{III}}$  XANES spectrum of the as-made Eu-doped FCZ glass without  $\text{InF}_3$  doping. In the pre-edge region two maxima can be clearly seen: one is located at about  $6,975\text{ eV}$ , and the other is at about  $6,983\text{ eV}$ . These two absorption bands are associated with a dipole-allowed transition from a  $^2\text{P}_{3/2}$  core level into an empty  $5d$  state and are characteristic WLs of  $\text{Eu}^{2+}$  and  $\text{Eu}^{3+}$  [54].

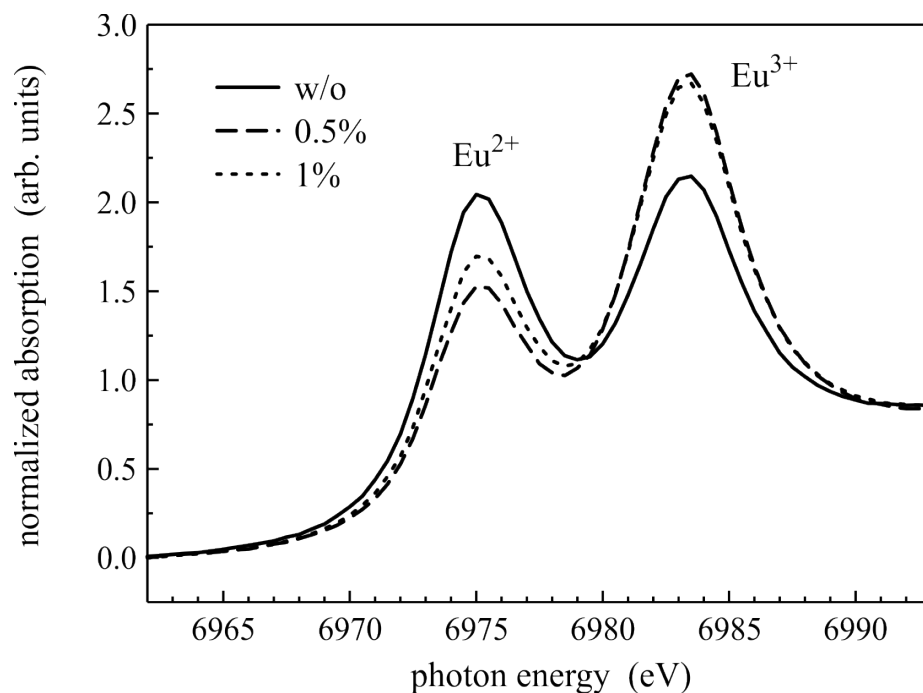


Figure 13: Normalized XANES spectra of the as-made Eu-doped FCZ glasses without (solid curve) and with 0.5 (dashed curve) and 1 mol%  $\text{InF}_3$  (dotted curve).

The WL of the  $\text{Eu}^{2+}$  species is approximately 8 eV lower than the WL of  $\text{Eu}^{3+}$  species. The relative intensity of the two WLs is an indication of the  $\text{Eu}^{2+}$ -to- $\text{Eu}^{3+}$  ratio [55, 56]. To obtain quantitative information about these WLs and to determine the  $\text{Eu}^{2+}$ -to- $\text{Eu}^{3+}$  mole ratio, a pseudo-Voigt function and an arctangent function were used to fit each WL and the absorption edge, respectively. The fitted curve (dashed curve) and the individual fitted components (dotted curves) are shown in the same graph. It is known that the area ratio ( $A_{\text{Eu}}$ ) between the  $\text{Eu}^{2+}$  and  $\text{Eu}^{3+}$  WLs is related to the mole ratio ( $M_{\text{Eu}}$ ) through  $M_{\text{Eu}} = R \cdot A_{\text{Eu}}$ , where  $R$  is a constant that is related to the  $2p \rightarrow 5d$  transition probabilities of  $\text{Eu}^{2+}$  and  $\text{Eu}^{3+}$  [56].

In a dilute system (e.g., an aqueous solution), the  $R$  value for Eu is about 1.5, determined from an in situ XANES analysis of electrochemical conversion between  $\text{Eu}^{2+}$  and  $\text{Eu}^{3+}$  in an  $\text{EuCl}_3$  solution [56]. Since the Eu content is only 3 mol% in the samples (see Table 1), the system can be considered dilute. Therefore, an  $R$  value of 1.5 is used to determine  $M_{\text{Eu}}$ , which is used to calculate the mole fraction of Eu ions.

The XANES spectra depend significantly on the  $\text{InF}_3$  doping. Figure 13 shows the normalized Eu  $L_{\text{III}}$  XANES spectra of as-made FCZ glass ceramics without (solid curve) and with 0.5 (dashed curve) and 1 mol%  $\text{InF}_3$  (dotted curve). A significant shift in the energy of the XANES WLs is not evident in any of the spectra. The height of the  $\text{Eu}^{2+}$  and  $\text{Eu}^{3+}$  WLs and therefore the  $\text{Eu}^{2+}$ -to- $\text{Eu}^{3+}$  mole ratio changes significantly upon increasing the  $\text{InF}_3$  doping level. The  $\text{Eu}^{2+}$  WLs of the  $\text{InF}_3$ -doped samples are less intense than in the indium-free sample, whereas the  $\text{Eu}^{3+}$  WLs are more intense. The  $\text{Eu}^{2+}$  WLs of both the  $\text{InF}_3$ -doped

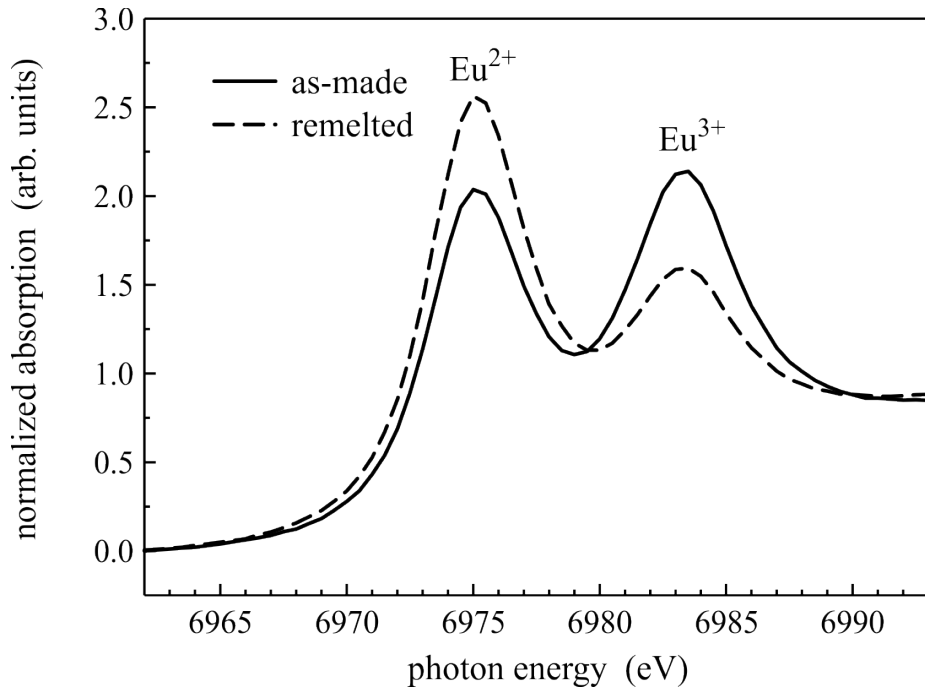


Figure 14: Normalized XANES spectra of the indium-free Eu-doped FCZ glass, as-made (solid curve), and remelted (dashed curve).

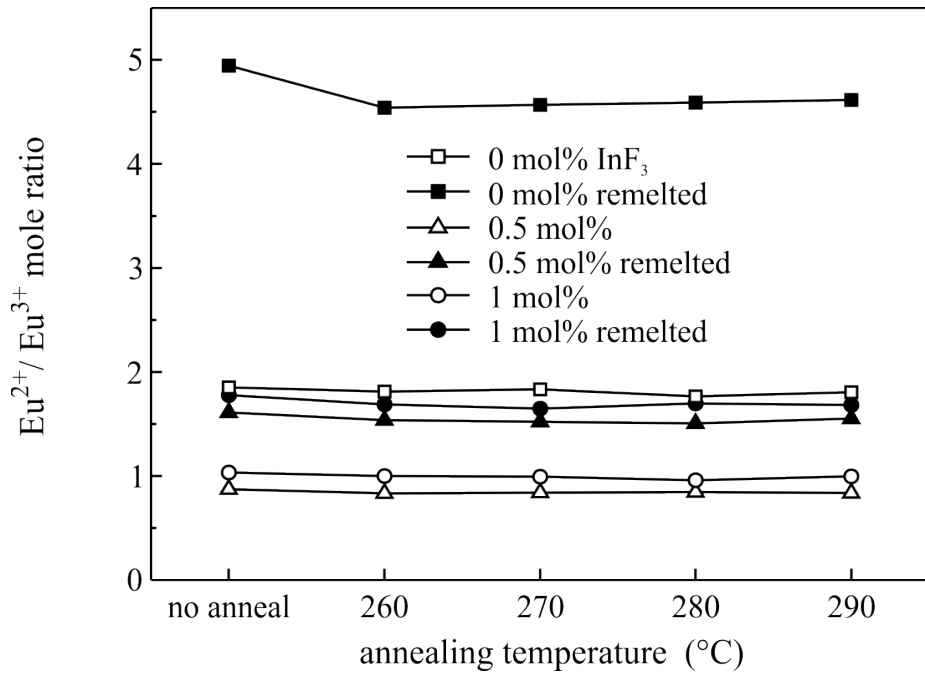


Figure 15:  $\text{Eu}^{2+}$ -to- $\text{Eu}^{3+}$  mole ratio vs annealing temperature for different  $\text{InF}_3$  mole ratios.

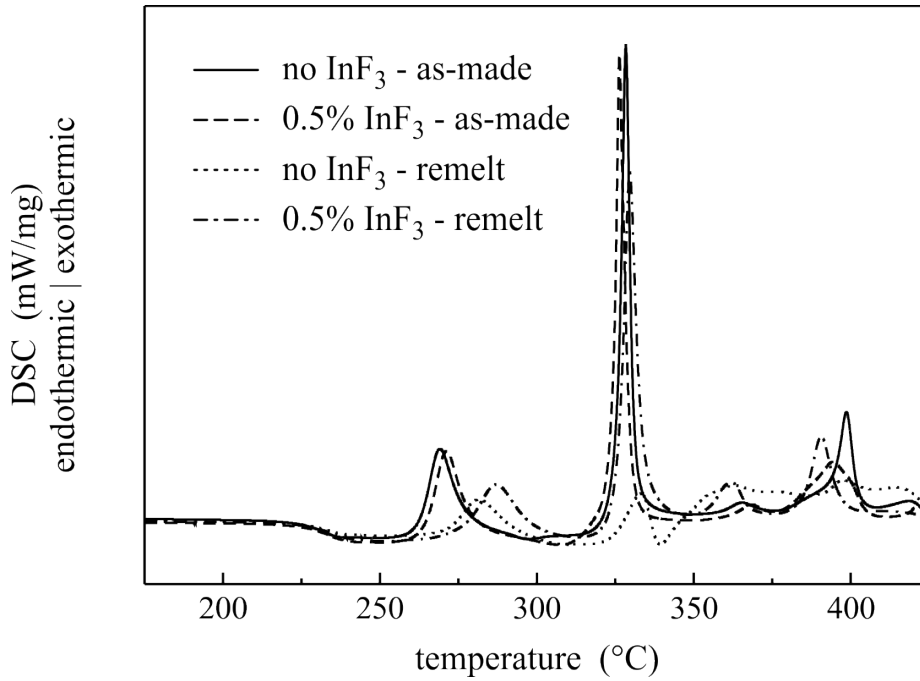


Figure 16: DSC measurements for as-made and remelted Eu-doped FCZ glasses. The heating rate was 10 K/min.

samples have about the same height; The  $\text{Eu}^{2+}$  WL of the 0.5 mol%  $\text{InF}_3$ -doped sample is slightly less intense than the one of the 1 mol% sample.

Remelting the samples without any additional chemicals leads to significant changes in the  $\text{Eu}^{2+}$ -to- $\text{Eu}^{3+}$  mole ratio. The normalized XANES spectra of the indium-free sample before and after a remelting step can be seen in Fig. 14. For the original sample the WLs of  $\text{Eu}^{2+}$  and  $\text{Eu}^{3+}$  are about the same height, whereas after the remelting process the WL of  $\text{Eu}^{2+}$  is significantly higher than the  $\text{Eu}^{3+}$  WL, i.e., the  $\text{Eu}^{2+}$  WL increases in height and the  $\text{Eu}^{3+}$  WL height decreases.

Figure 15 shows the  $\text{Eu}^{2+}$ -to- $\text{Eu}^{3+}$  mole ratio of the Eu-doped FCZ glass ceramics versus the annealing temperature. Thermal annealing under an inert gas atmosphere has no influence on the  $\text{Eu}^{2+}$ -to- $\text{Eu}^{3+}$  mole ratio (XANES spectra are not shown).

### 3.2 DIFFERENTIAL SCANNING CALORIMETRY

As shown in the XANES section, the Eu oxidation state is significantly affected by the addition of indium and subsequent remelting. Further investigation focuses on the influence of indium and/or remelting on the crystallization; this was done using DSC, XRD and PL. DSC provides information on the onset of the  $\text{BaCl}_2$  crystallization [10].

The DSC data of Eu-doped FCZ glasses with and without 0.5 mol%  $\text{InF}_3$  are shown in Fig. 16. The glass transition temperature is approximately 230 °C and

does not change upon increasing  $\text{InF}_3$  content or when the sample is remelted. The first exothermic peak can be found at 271 and 269 °C for glasses with and without 0.5 mol%  $\text{InF}_3$ , respectively. For the glass containing 1 mol%  $\text{InF}_3$ , the first crystallization peak is found at 277 °C (not shown). In Ref. [10] this peak is attributed to the crystallization of  $\text{BaCl}_2$  nanoparticles. For the remelted samples the crystallization peak is smaller and shifted to higher temperatures, i.e., 281, 287, and 293 °C (not shown) for glasses with 0, 0.5, and 1 mol%  $\text{InF}_3$ , respectively. The large crystallization peak at 330 °C is associated with a partial crystallization of the glass matrix, namely the formation of  $\beta\text{-BaZrF}_6$  and  $\text{NaZrF}_5$  [29, 57].

### 3.3 X-RAY DIFFRACTION

Knowing the exact crystallization points and the influence of the addition of indium and subsequent remelting from DSC, similar differences should also be seen in the x-ray diffraction measurements.

Figure 17 shows XRD patterns for the Eu-doped FCZ glasses containing 0.5 mol%  $\text{InF}_3$  annealed at temperatures from 260 °C to 290 °C for 20 min and of an associated remelted glass with 0.5 mol%  $\text{InF}_3$  annealed at 290 °C. The as-poured glass does not show any crystalline phases and is therefore not shown. Post thermal treatment between 260 °C and 280 °C for 20 min leads to x-ray reflections which can be attributed to the formation and growth of  $\text{BaCl}_2$  nanocrystals of hexagonal structure (space group  $P\bar{6}2m$  (189), see bottom bar pattern). For higher annealing temperatures sharper reflections in terms of lower full width at half maximum (FWHM) values as well as better resolved diffraction patterns are obtained. For lower temperatures, i.e., at 260 °C the reflections for  $2\theta$  angles around 39° and 61° overlap due to the small number and small size of the already formed nanocrystals. Higher temperatures, i.e., a larger volume fraction of still growing nanocrystals result in a higher reflection intensity and therefore a better signal to noise ratio and a separation of these overlapped reflections, respectively. Upon annealing at 290 °C a phase transition from hexagonal to the orthorhombic  $\text{BaCl}_2$  structure (space group  $Pnma$  (62), see top bar pattern) and a so far unidentified reflection at 26.3° is observed. Remelting of the as-poured glass followed by an annealing at 290 °C for 20 min leads to a diffraction pattern which can be exclusively attributed to hexagonal  $\text{BaCl}_2$  nanocrystals. Both the unidentified and the orthorhombic  $\text{BaCl}_2$  phases are not observed.

Figure 18 shows XRD patterns for the Eu-doped FCZ glasses without  $\text{InF}_3$ , but also annealed at temperatures from 260 °C to 290 °C for 20 min and of an associated remelted glass without  $\text{InF}_3$  annealed at 290 °C. The crystal growth behavior is similar to that of the  $\text{InF}_3$ -doped sample: higher temperatures result in a higher crystallized  $\text{BaCl}_2$  volume fraction and a higher reflection intensity. However, for the Eu-doped FCZ glass annealed at 290 °C no phase transition from hexagonal to the orthorhombic  $\text{BaCl}_2$  structure is observed as was seen for the corresponding sample doped with  $\text{InF}_3$ . All glasses of the indium-free series contain mainly hexagonal phase  $\text{BaCl}_2$ , but for both the normal and the remelted samples heat treated at 290 °C, the additional unidentified reflection for the 26.3°  $2\theta$  angle occurs.

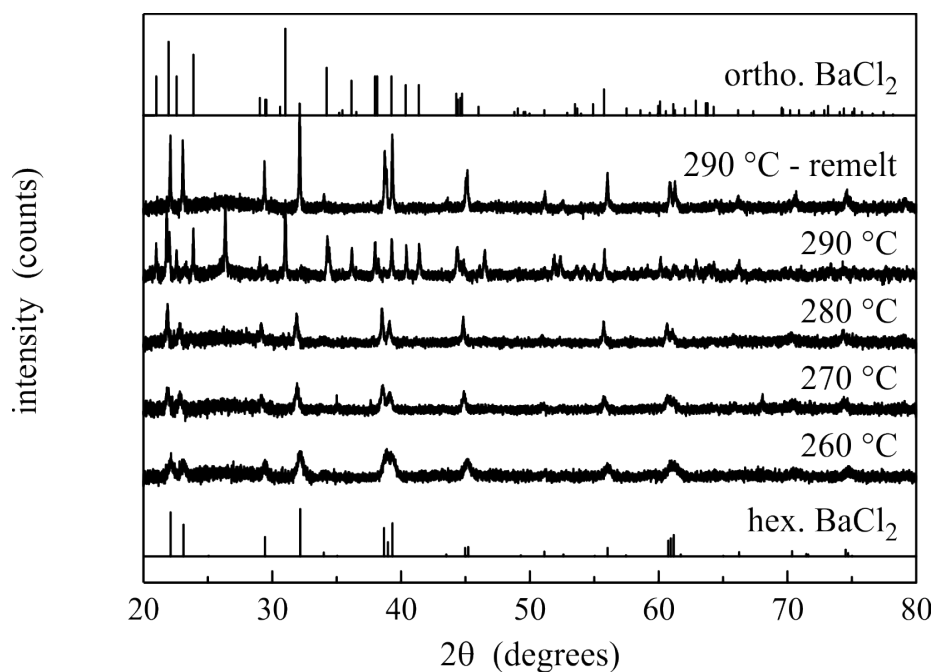


Figure 17: XRD patterns of Eu-doped FCZ glasses with 0.5 mol% InF<sub>3</sub> annealed at temperatures from 260 °C to 290 °C for 20 min and of an associated remelted glass with 0.5 mol% InF<sub>3</sub> annealed at 290 °C. The XRD patterns of hexagonal (bottom, PDF 45-1313) and orthorhombic BaCl<sub>2</sub> (top, PDF 24-0094) are shown for comparison.

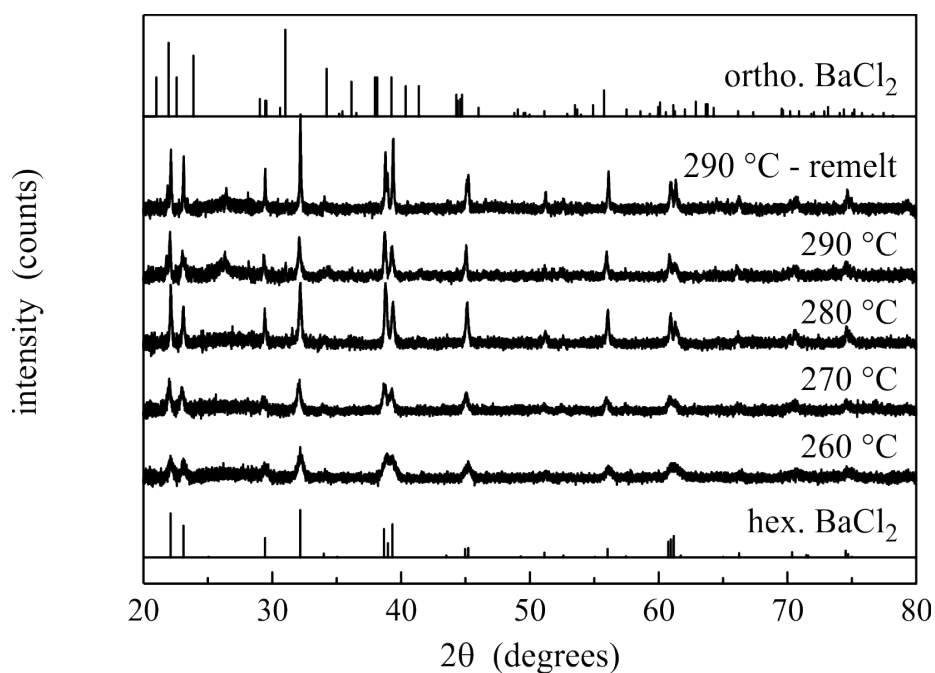


Figure 18: XRD patterns of Eu-doped FCZ glasses without InF<sub>3</sub> annealed at temperatures from 260 °C to 290 °C for 20 min and of an associated remelted glass without InF<sub>3</sub> annealed at 290 °C. The XRD patterns of hexagonal (bottom, PDF 45-1313) and orthorhombic BaCl<sub>2</sub> (top, PDF 24-0094) are shown for comparison.

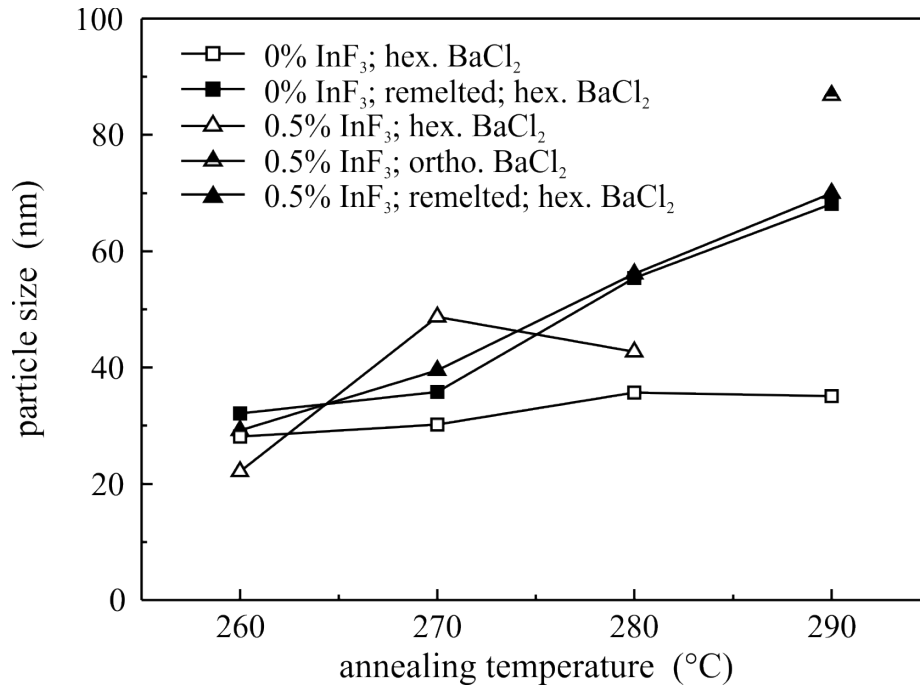


Figure 19: Particle sizes for the (201) (hexagonal BaCl<sub>2</sub> phase) and the (211) (orthorhombic BaCl<sub>2</sub> phase, half open triangle) reflections for the Eu-doped FCZ glasses without (open squares) and with 0.5 mol% InF<sub>3</sub> (open triangles) and their associated remelted glasses (filled symbols) vs annealing temperature.

The XRD reflections are wider than the instrumental linewidth caused by size broadening effects due to the growing nanoparticles. Using the reflection analysis function of the *DIFFRACplus EVA v1.2* XRD software, the particle size can be estimated with the Scherrer formula. Figure 19 shows an overview of the particle sizes for the (201) (hex. phase, squares) and the (211) (ortho. phase, circles) reflections for the Eu-doped FCZ glasses without (open squares) and with 0.5 mol% InF<sub>3</sub> (open triangles) and their associated remelted glasses (filled symbols) versus annealing temperature. At 260 °C the particles for all glasses are of nearly equal diameter ( $d=28\pm4$  nm). As already shown in Ref. [10], in general, an increase of the hexagonal crystallite size with increasing annealing temperature is observed. A comparison of the hexagonal BaCl<sub>2</sub> phase nanocrystal sizes of all glasses leads to the conclusion that the additional remelting step results in larger overall diameters. Both the remelted indium-free and the InF<sub>3</sub>-doped samples show very similar particle sizes from around 30 nm at 260 °C to  $\approx 70$  nm at 290 °C. However, for the non-remelted sample containing InF<sub>3</sub> the BaCl<sub>2</sub> phase transition starts between 280 and 290 °C and is fully completed at 290 °C, since no more reflections of hexagonal BaCl<sub>2</sub> are measurable. The mean particle size of the orthorhombic phase is  $\approx 87$  nm. The particle sizes and crystal growth conditions of the non-remelted indium-free glass are not strongly affected by different annealing temperatures. From 260 °C ( $d=28$  nm) to 290 °C ( $d=35$  nm) the mean size increases only by  $\approx 7$  nm.

### 3.4 PHOTOLUMINESCENCE

Compared to XRD, PL is even more sensitive to the structure of the BaCl<sub>2</sub> nanocrystals. PL spectra of differently annealed FCZ samples, with and without 0.5 mol% InF<sub>3</sub>, are plotted in Fig. 20. The samples were annealed for 20 min at temperatures between 260 and 290 °C. All spectra have been normalized to their most intense emission.

The as-made, indium-free sample annealed at 260 °C (top left, dashed-dotted curve) shows the typical PL spectrum for a glass ceramic containing predominantly hexagonal phase BaCl<sub>2</sub> particles [10]. The peak at 406 nm is attributed to the 5d-4f transition of Eu<sup>2+</sup> in hexagonal BaCl<sub>2</sub>; the origin of the less intense but broader emission at 485 nm is unknown. A similar band near 485 nm was reported in FZ glass ceramics containing small hexagonal phase BaBr<sub>2</sub> crystallites and interpreted to be based on an impurity associated Eu<sup>2+</sup> site with a perturbed crystal field [58, 59]. The 485 nm emission has only been observed in glass ceramics containing hexagonal phase BaCl<sub>2</sub> nanoparticles. When annealing up to 290 °C, the intensity of the 485 nm band lessens but there is no phase transformation from hexagonal to orthorhombic phase BaCl<sub>2</sub>, as was reported in Refs. [9] and [10], even though the heat treatment at 290 °C was well above the temperature of formation of the nanocrystals (see Fig. 16, solid curve).

The 0.5 mol% InF<sub>3</sub> doped sample (top right) shows the hexagonal phase after annealing at 260 °C. Annealing at 290 °C leads to the formation of orthorhombic phase BaCl<sub>2</sub>: the 406 nm band is shifted to 401 nm, i.e., to the bulk BaCl<sub>2</sub> value [60], while the 485 nm band is almost gone. When the as-made sample without indium is remelted and subsequently annealed at different temperatures (bottom left), the 485 nm peak is the most intense one, but the 406 nm peak increases upon heat treatment and after the 290 °C annealing step, both bands have the same intensity. However, it seems that there is also no phase transformation from hexagonal phase to orthorhombic phase BaCl<sub>2</sub> although the annealing temperature of 290 °C is again above the crystallization peak of the BaCl<sub>2</sub> nanocrystals (see Fig. 16, dotted curve). On remelting the as-made sample that contained 0.5 mol% InF<sub>3</sub> (see Fig. 20, bottom right), the 485 nm band is as intense as the 406 nm band after the 260 °C annealing step, but the spectra after the 270, 280, and 290 °C anneal are all very similar with the 485 nm band slightly having less in intensity than the 406 nm one.

### 3.5 DISCUSSION

The results show that the Eu<sup>2+</sup>-to-Eu<sup>3+</sup> ratio in Eu-doped FCZ glasses depends significantly on the quantity of InF<sub>3</sub> added and on the melting process. The glasses containing InF<sub>3</sub> always show a ratio of approximately 0.85 (0.5 mol%) and 1 (1 mol%) Eu<sup>2+</sup>-to-Eu<sup>3+</sup>. Remelting of these glasses leads to an increase in the Eu<sup>2+</sup>-to-Eu<sup>3+</sup> mole ratio to values between 1.5 (0.5 mol%) and 1.7 (1 mol%). Without the InF<sub>3</sub> additive, a higher fraction of Eu<sup>2+</sup> is produced. The indium-free glass has an Eu<sup>2+</sup>-to-Eu<sup>3+</sup> mole ratio of about 1.8 before the remelting process.

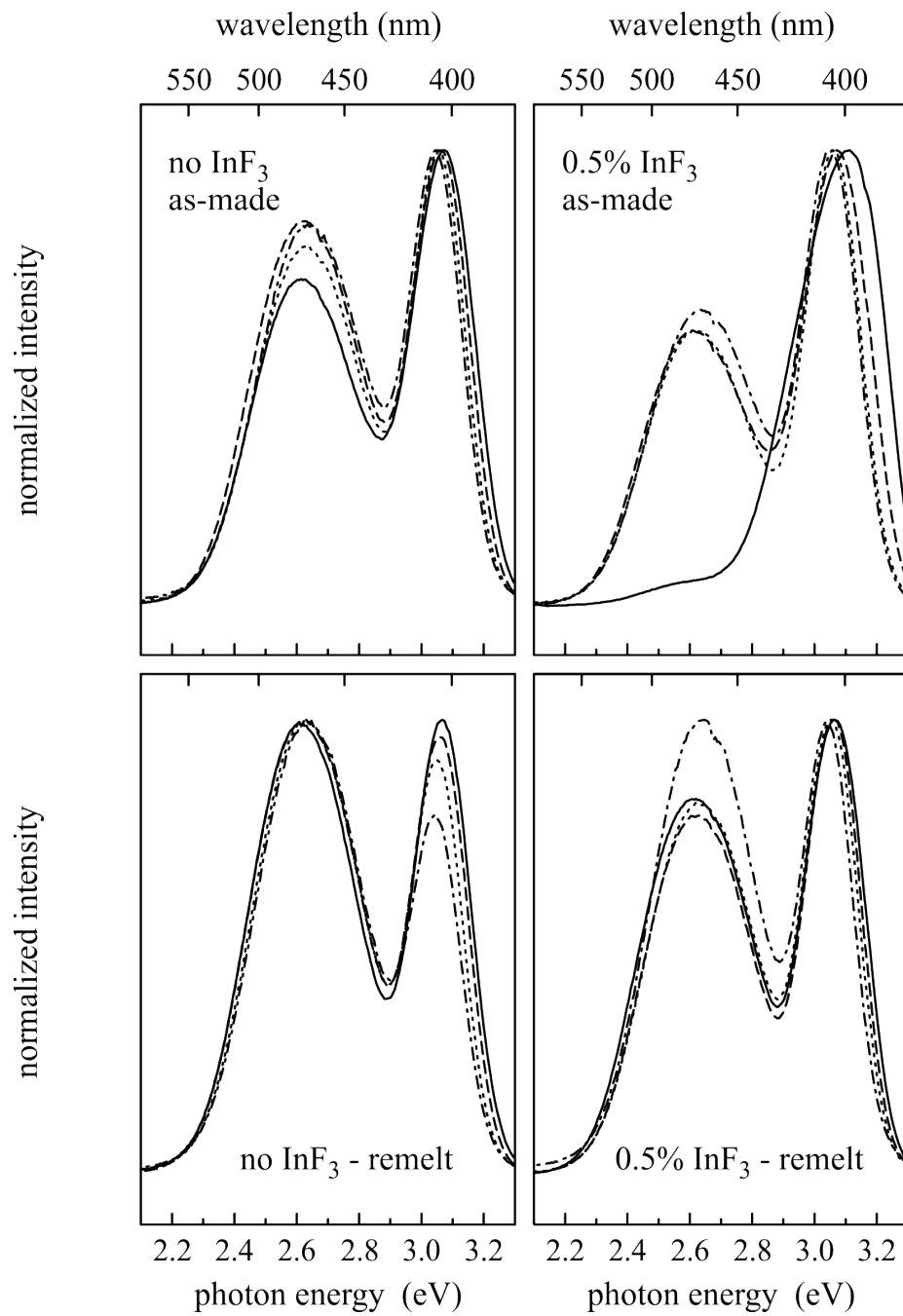


Figure 20: Normalized PL spectra of as-made and remelted Eu-doped FCZ glass ceramics annealed at 260 (dashed-dotted), 270 (dotted), 280 (dashed), and 290 °C (solid curve) for 20 min. The PL was excited at 280 nm.

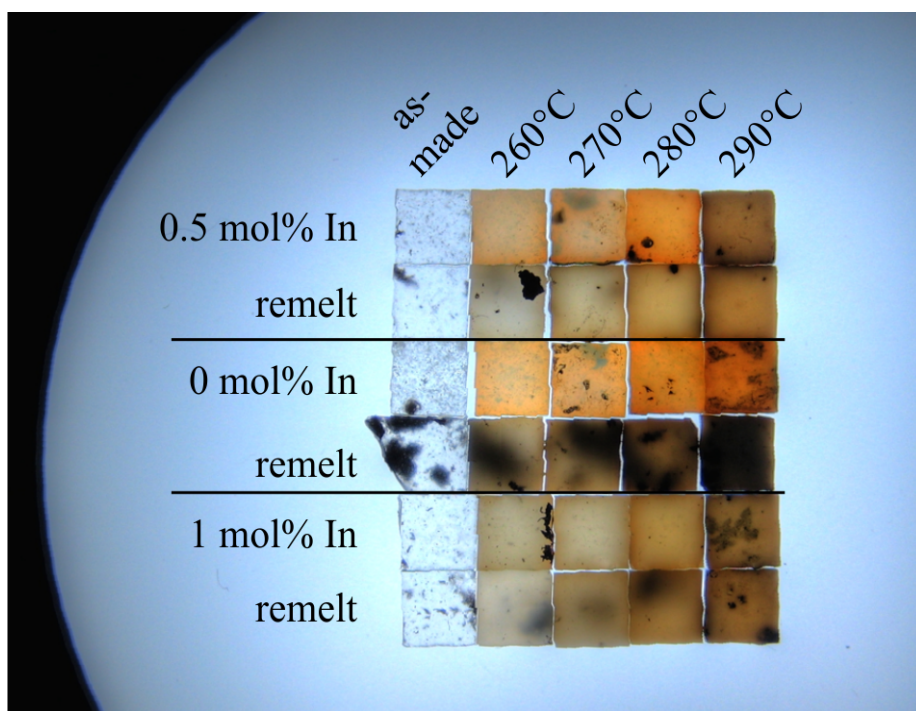


Figure 21: Overview of the  $\text{InF}_3$  glasses, as-made and annealed at different temperatures from 260 °C to 290 °C in steps of 10 °C for 20 minutes.

Interestingly, the  $\text{Eu}^{2+}$  content can be further increased by a factor of about 2 upon remelting the glasses; the ratio increases to about 4.6, i.e., more than 80% of the europium ions are divalent. However, the quality of the glasses also depends on the addition of indium and the melting process. Samples with lower amounts of  $\text{InF}_3$  show a large number of black precipitates (reduced Zr) on the surface (see Fig. 21). After remelting, the number and size of these precipitates increase, in particular for those glasses without  $\text{InF}_3$ .

This problem is alleviated in the presence of  $\text{InF}_3$  as  $\text{InF}_3$  acts as a mild oxidizer. It appears that when  $\text{InF}_3$  is added to maintain Zr in the 4+ state, it also oxidizes some of the  $\text{Eu}^{2+}$  to  $\text{Eu}^{3+}$ . This does not seem to depend on the amount of  $\text{InF}_3$  added to the glass. Both glasses containing  $\text{InF}_3$  have the same  $\text{Eu}^{2+}$ -to- $\text{Eu}^{3+}$  ratio within experimental error.

The interactions within the material between the multiple cations and the halides are very complex. It is known that fluorine and chlorine evaporate during the melting process; ion chromatography results show that this could be up to 25% by weight. In the remelting process, it is likely that further halide is lost and so the redox conditions change as there is less fluorine and chlorine to bond to the cations. The indium additive and the melting process also affect the crystallization properties of the FCZ glasses. The  $\text{BaCl}_2$  crystallization peak shifts to higher temperature upon increasing the amount of  $\text{InF}_3$  and upon remelting. In all annealed samples, crystallization of hexagonal phase  $\text{BaCl}_2$  can be found, but only for as-made  $\text{InF}_3$ -containing glass ceramics a phase transformation to orthorhombic phase  $\text{BaCl}_2$  is observed. Indium is required to produce the

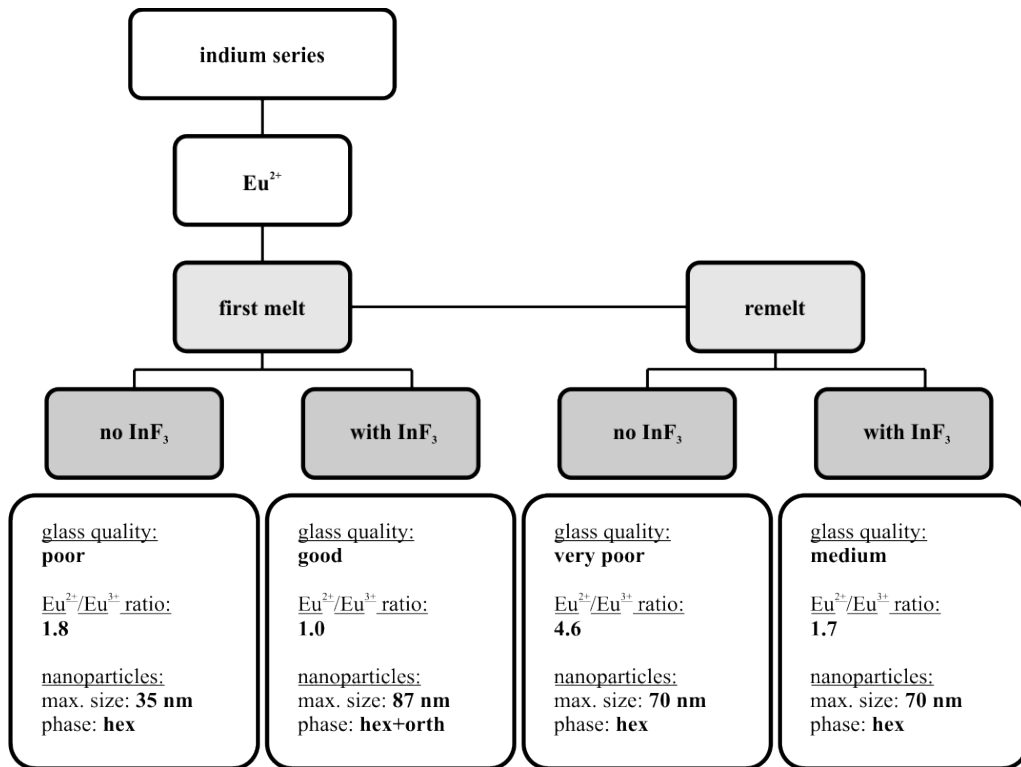


Figure 22: Final overview of the obtained results for the indium series.

desirable orthorhombic phase for the material to work as a storage phosphor. When the as-made glass is heated for the first time, an exothermic peak appears as the nanocrystals form. If the material is cooled to room temperature and heated again the nanoparticles do not precipitate. As the nanocrystals are already crystallized in the first heating and there is no thermodynamic impetus to reverse this reaction upon cooling. Therefore it is plausible that this is why no nanocrystal precipitation takes place on the second heating. The hexagonal phase is formed at temperatures below 290 °C, above this temperature the orthorhombic phase is formed.

Using InF<sub>3</sub> has both advantages and disadvantages. It has proved to be essential to glass quality. Without indium, the quantity of black precipitates (reduced Zr) is unacceptably high. In addition, InF<sub>3</sub> is also important for the storage phosphor applications; without the addition of In, no phase transformation from hexagonal to orthorhombic phase BaCl<sub>2</sub> nanoparticles can be found. While subsequent remelting of the glass has proved to have a detrimental effect on storage properties, the performance of the glass ceramics for scintillator applications, where hexagonal phase BaCl<sub>2</sub> and a high Eu<sup>2+</sup> content are needed, is significantly improved by a remelting step. A final overview of the results is shown in Fig. 22.

## MULTIVALENT EUROPIUM-DOPING

The preceding chapter gave first insights into the complex equilibria of an FCZ glass melt. However, the following chapter will focus on the most important and expensive ingredient of the luminescent glasses and glass ceramics: the fluorescent divalent europium. The high price in the world market is due to a serious shortage of rare-earth minerals, mostly caused by China's export embargoes and price policy in 2010 and 2011. Doubled or tripled costs of rare-earth materials are first signs of an upcoming crisis which is predicted to climax in 2014 and 2015 [11]. Therefore, the  $\text{Eu}^{2+}$  portion of the image plate is the most expensive part. An attempt to overcome this problem is an in situ reduction of the relatively inexpensive  $\text{EuCl}_3$  to introduce divalent europium ions into the glass. Some parts and figures of this chapter have appeared previously in [61].

Several routes are under investigation. MacFarlane *et al.* [62] reduced trivalent europium by using metal hydrides and adding hydrogen to the process atmosphere. Hydrogen reacts with the  $\text{EuCl}_3$  to produce gaseous hydrogen chloride and  $\text{EuCl}_2$ . Unfortunately, melting in a hydrogen-bearing atmosphere can partially reduce  $\text{ZrF}_4$  and form the already mentioned dark gray precipitates in the glass. Phebus *et al.* [63] showed that while trivalent europium was practically all reduced in a 4% hydrogen in nitrogen atmosphere, the resulting glass was of poor quality. Coey *et al.* [64] showed that fluoride glasses made using 10 – 20 mol%  $\text{EuF}_2$  contained a significant proportion of  $\text{EuF}_3$  after processing. Mössbauer spectra had a broad peak centered at  $-14 \text{ mm s}^{-1}$  indicating spin relaxation of the  $\text{Eu}^{2+}$  ions. The  $\text{Eu}^{3+}$  produced a much narrower peak environment at  $0 \text{ mm s}^{-1}$ . Ball *et al.* [49] also used Mössbauer spectroscopy to investigate thermal reduction of  $\text{EuCl}_3$  processed in a vacuum furnace. They discovered that a mixture of  $\text{EuCl}_3$ , a chlorine deficient phase  $\text{EuCl}_{2.8}$ , and  $\text{EuCl}_2$  was formed by treatment at  $300 \text{ }^\circ\text{C}$ .

Glassner compiled thermodynamic data for a variety of metal halides including the components of ZBLAN glass, but not for europium dihalides [48]. The data for Zr show that at all temperatures,  $\text{ZrF}_3$  is the most stable fluoride. The thermodynamic stability of  $\text{ZrF}_3$  in the glasses has not been confirmed. However, MacFarlane *et al.* [62] processed melts in hydrogen-bearing atmospheres and found black precipitates in the glass that were attributed to reduced zirconium species. The precise mechanism of formation of these precipitates is not yet understood. Broer observed black precipitates in ZBLAN glasses and attributed them to partially reduced zirconium halides [51]. Rard reviewed the properties and thermodynamics of RE fluorides and reported reduction of  $\text{Eu}^{3+}$  on heating [12]. Massot *et al.* [13] studied reduction of  $\text{Eu}^{3+}$  in molten salts by using cyclic voltammetry. They reported an equilibrium constant of 0.811 for  $[\text{Eu}^{2+}]/[\text{Eu}^{3+}]$  at  $800 \text{ }^\circ\text{C}$ . This finding is consistent with Rard's assessment and suggests that thermal reduction of  $\text{EuCl}_3$  is a feasible route for synthesizing the divalent salt.

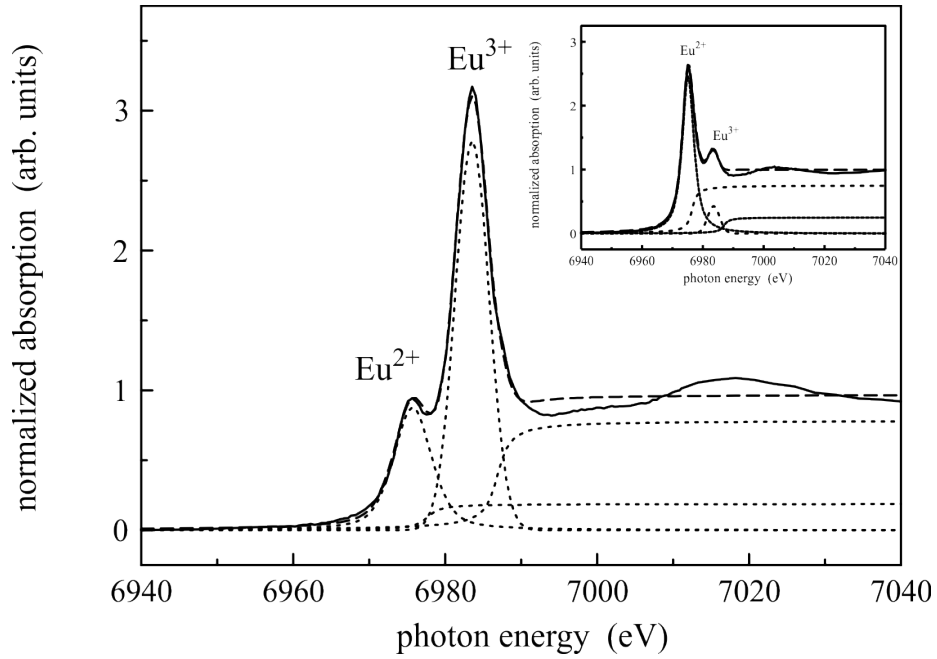


Figure 23: Normalized XANES spectrum of the as-made, nominal 100%  $\text{EuCl}_3$ -doped FCZ glass. A pseudo-Voigt function and an arctangent function (dashed curves) were used to fit each of the characteristic white lines of  $\text{Eu}^{2+}$  and  $\text{Eu}^{3+}$  and their absorption edges, respectively. The inset shows the normalized XANES spectrum of the as-made, nominal 100%  $\text{EuCl}_2$ -doped FCZ glass for comparison.

In the following sections, focus is put on the amount of divalent and trivalent Eu chloride and fluoride additives. The nominal composition of the FCZ glasses investigated is  $51\text{ZrF}_4\text{-}20\text{BaCl}_2\text{-}20\text{NaF}\text{-}3.5\text{LaF}_3\text{-}3\text{AlF}_3\text{-}0.5\text{InF}_3\text{-}x\text{EuCl}_2\text{-}(2-x)\text{EuCl}_3$  ( $x=0, 0.4, 0.8, 1.2, 1.6, 2.0$ ) (values in mol%) for the chloride series, and  $51\text{ZrF}_4\text{-}20\text{BaCl}_2\text{-}20\text{NaF}\text{-}3.5\text{LaF}_3\text{-}3\text{AlF}_3\text{-}0.5\text{InF}_3\text{-}x\text{EuF}_2\text{-}(2-x)\text{EuF}_3$  ( $x=0, 0.4, 0.8, 1.2, 1.6, 2.0$ ) (values in mol%) for the fluoride series. The effect of multivalent Eu doping on the  $\text{BaCl}_2$  crystallization is discussed. XANES, DSC and XRD investigations were performed to evaluate the accurate  $\text{Eu}^{2+}$ -to- $\text{Eu}^{3+}$  ratios, as well as the  $\text{BaCl}_2$  crystal phases.

#### 4.1 X-RAY ABSORPTION NEAR EDGE STRUCTURE

Figure 23 shows the normalized Eu  $L_{\text{III}}$  XANES spectrum of the as-poured, nominal 100%  $\text{EuCl}_3$ -doped FCZ glass. As already mentioned in Chapter 3, the two absorption bands located at approximately 6,975 eV and 6,983 eV are caused by a dipole-allowed transition from a  $2P_{3/2}$  core level into an empty 5d state and can be assigned to the characteristic WLs of  $\text{Eu}^{2+}$  and  $\text{Eu}^{3+}$ , respectively [54]. The  $\text{Eu}^{2+}$ -to- $\text{Eu}^{3+}$  ratios can be determined by building the relative intensity ratios of the two WLs via fitting each WL by a pseudo-Voigt and arctangent function (see Fig. 23).

Figure 24 shows the measured  $\text{Eu}^{2+}$  fractions for different ratios of  $\text{EuCl}_2$ -to- $\text{EuCl}_3$  in FCZ glasses versus annealing temperature. The actual  $\text{Eu}^{2+}$  content

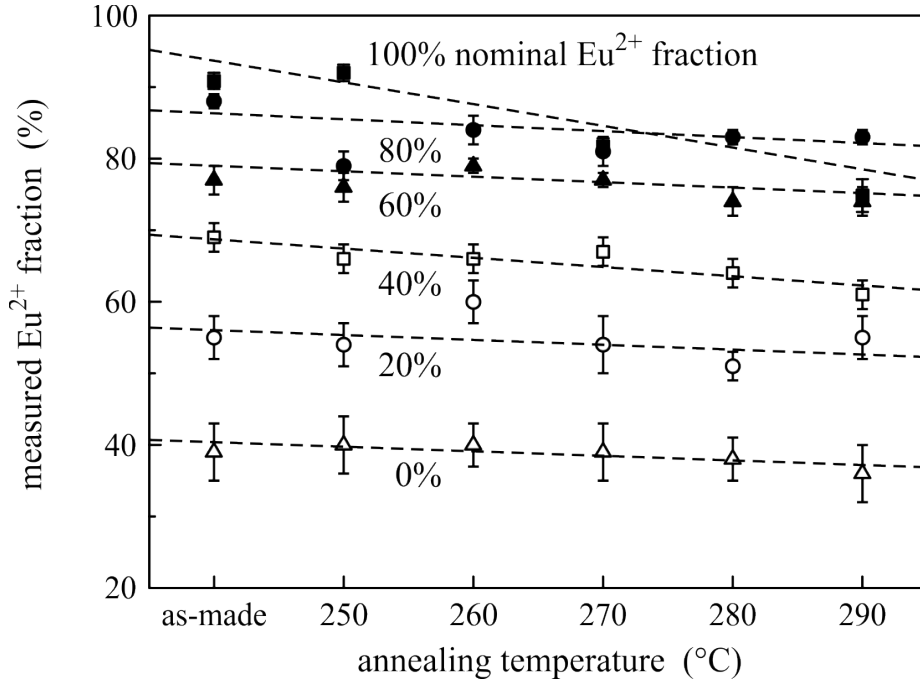


Figure 24: Measured  $\text{Eu}^{2+}$  fraction for differently  $\text{EuCl}_2$ -to- $\text{EuCl}_3$ -doped FCZ glasses vs. annealing temperature. The linear fits are a guide to the eye.

differs from the nominal  $\text{Eu}^{2+}$  doping and also shows a slight decrease when the annealing temperature is increased within each doping series, in contrast to the series in Chapter 3. In this case, the heat treatment was done in an inert-argon atmosphere, whereas it was previously done in nitrogen. Another difference is that the studied samples here were exposed to air for several days before the heat treatment.

Weber *et al.* [14] evaluated Mössbauer measurements on an  $\text{Eu}^{2+}$ - $\text{Eu}^{3+}$  mixed powder and attributed the decrease in  $\text{Eu}^{2+}$ , after 10 weeks exposure in air, to oxidation. The observed behavior here is, therefore, likely caused by a small partial and diffusion-limited oxidation of  $\text{Eu}^{2+}$  on and near the oxygen-contaminated glass surfaces during the annealing step. The diffusion coefficient in solids at different temperatures is well known to be proportional to  $\exp(-E_A/RT)$ , with the activation energy for diffusion  $E_A$ , the universal gas constant  $R$ , and the temperature  $T$  of the solid. Therefore, higher annealing temperatures lead to slightly larger diffusion distances for oxygen and moisture for the same annealing time, leading to a decrease in the actual  $\text{Eu}^{2+}$  content. The melting process has an even bigger influence. When doped with pure  $\text{EuCl}_3$ , about 40% of the  $\text{Eu}^{3+}$  is reduced to  $\text{Eu}^{2+}$ . Looking at the thermodynamics and at the primary-phase equilibrium for changing the Eu oxidation state, this result fits well with theory. The reaction equation during heat treatment above 570 K (297 °C) is given by [65]:



and the corresponding equilibrium constant is given by:

$$K = \exp\left(-\frac{G_T^\ominus}{RT}\right) = \frac{a[\text{EuCl}_2] p^{1/2} [\text{Cl}_2]}{a[\text{EuCl}_3]}, \quad (13)$$

with the free energy of the reaction  $G_T^\ominus$  at process temperature  $T$  and the gas constant  $R$ . As previously mentioned, Massot *et al.* calculated  $K$  to be 0.811 for an operating temperature of 800 °C via an electrochemical study. For pure  $\text{EuCl}_3$  doping, this would result in an equilibrium consisting of 45%  $\text{Eu}^{2+}$  and 55%  $\text{Eu}^{3+}$ , confirming the measured data for the ZBLAN: $\text{EuCl}_3$  melt, i.e., the sample with nominal 0%  $\text{Eu}^{2+}$  fraction in the as-made state.

Doping with pure  $\text{EuCl}_2$  shows the possible  $\text{Eu}^{2+}$  doping limit for the above explained melting process to be slightly more than 90% for the as-made glass (see Fig. 24). It was shown that the  $\text{InF}_3$  additive acts as a mild oxidizer preventing a reduction from  $\text{Zr}^{4+}$  to  $\text{Zr}^{3+}$  for reasons of glass quality, but at the same time also oxidizes some  $\text{Eu}^{2+}$  to  $\text{Eu}^{3+}$ . Moreover, even minimal oxygen contamination in the used raw materials and the above-mentioned long air exposure could lead to this oxidation process and the 90% limit, respectively. Unlike all other series, the nominal pure 2 mol%  $\text{EuCl}_2$ -doped series shows a significant downward trend to lower  $\text{Eu}^{2+}$  fractions with higher annealing temperatures (78% for 20 min annealing at 290 °C) synonymous with an increased conversion from  $\text{Eu}^{2+}$  into  $\text{Eu}^{3+}$ . The reason is not completely understood yet, but could be related to a higher Eu fraction near the surface caused by a not fully homogeneously blended melt and glass, respectively, making an interaction with oxygen during air exposure more probable. Looking at the measured  $\text{Eu}^{2+}$  fractions and their corresponding theoretical  $\text{Eu}^{2+}$  fractions, it is noticeable that the difference between them is not linear in all regions.

Figure 25 shows the measured  $\text{Eu}^{2+}$  fraction for  $\text{Eu}^{2+}$ -to- $\text{Eu}^{3+}$  chloride- (squares) and fluoride- (triangles) doped FCZ glasses. During melting, more  $\text{Eu}^{2+}$  is formed when the glasses are doped with  $\text{EuCl}_3$  as opposed to  $\text{EuF}_3$ . Thus, for the chloride series and from nominal  $\text{Eu}^{2+}$  fractions between 0 and 80%, an even higher  $\text{Eu}^{2+}$  amount is found because of the reduction of the additional  $\text{Eu}^{3+}$  dopant. A saturation is observed at nominal  $\text{Eu}^{2+}$  fractions of more than 80% because of the above-mentioned effects of  $\text{InF}_3$  and oxygen contamination. These effects are confirmed when looking at the fluoride series, where the measured  $\text{Eu}^{2+}$  fraction also saturates at almost the same mean value of about 83% ( $\text{Eu}^{3+}$  fraction of about 17%) for a nominal pure  $\text{EuF}_2$ -doped glass.

#### 4.2 DIFFERENTIAL SCANNING CALORIMETRY

Again, DSC measurements are performed on all glass ceramics to be able to optimize the annealing conditions as well as the respective luminescence yield. Compared to Chapter 3, this section will give a more detailed DSC analysis, because it is known from literature, that  $\text{Eu}^{2+}$  is partially incorporated into the  $\text{BaCl}_2$  nanocrystals, for example by a substitution of a  $\text{Ba}^{2+}$  site, while  $\text{Eu}^{3+}$  is not [10]. Thus, the different Eu doping levels will have a significant impact on the nanocrystallization and phase transformation.

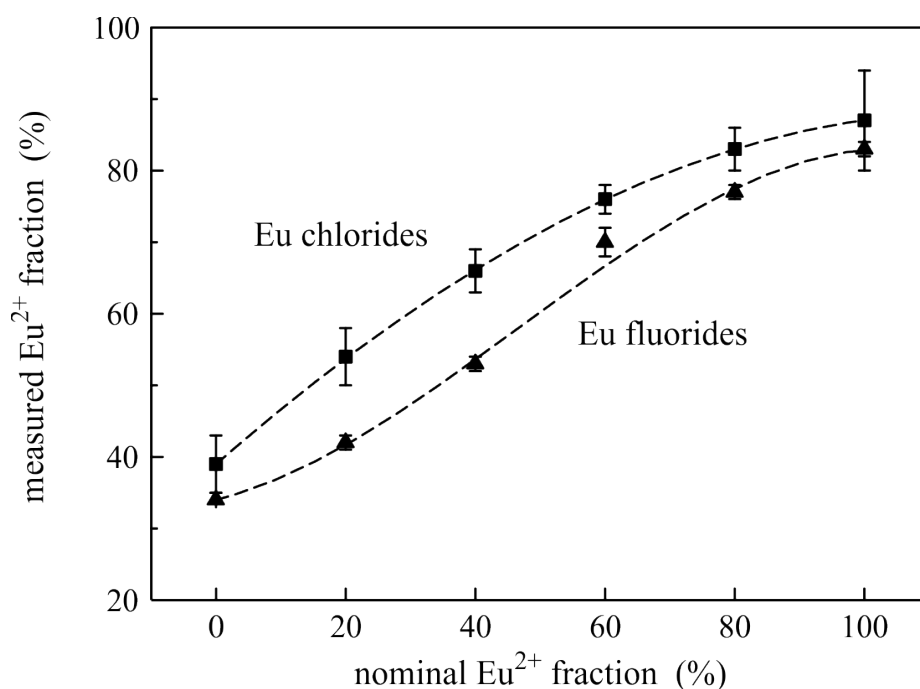


Figure 25: Measured  $\text{Eu}^{2+}$  fraction for  $\text{Eu}^{2+}$ -to- $\text{Eu}^{3+}$  chloride- (squares) and fluoride- (triangles) doped FCZ glasses vs their nominal  $\text{Eu}^{2+}$  fraction. The polynomial fits are a guide to the eye.

The oxidation state's influence on the crystallization is shown by non-isothermal DSC measurements. The important points of interest are marked in Fig. 26 for an FCZ glass with an  $\text{Eu}^{2+}$  fraction of 60%, measured with a heating rate of 10 K/min.  $T_g$  is the glass transition temperature, i.e., the point where glass viscosity and specific heat capacity drop significantly. The crystallization onset,  $T_x$ , and the peak temperature of the first crystallization,  $T_{p1}$ , are attributed to the crystallization of hexagonal  $\text{BaCl}_2$ , while  $T_{p2}$  is attributed to the phase transition from hexagonal to orthorhombic  $\text{BaCl}_2$ .

In the previous section, XANES was used to evaluate the accurate  $\text{Eu}^{2+}$ -to- $\text{Eu}^{3+}$  ratios. Figure 27 shows the peak temperature of both hexagonal and orthorhombic peak maxima as a function of the different  $\text{Eu}^{2+}/\text{Eu}^{3+}$  doping fractions; the heating rate was 5 K/min. A significant shift to lower temperatures is observed for both peaks when increasing the  $\text{Eu}^{2+}$  fraction from 0% to 20%. This trend confirms the behavior of the phase transition temperature obtained from corresponding XRD data of the heat treated samples (see section below): For pure  $\text{EuCl}_3$  doping higher annealing temperatures are required to convert the hexagonal particles into particles with orthorhombic crystal structure. The hexagonal phase is obtained with 20 min heat treatments between 250 to 270 °C; at 280 °C a phase mixture of hexagonal and orthorhombic phase is measured, while the fully crystallized orthorhombic phase is not observed before 290 °C. Crystallization peak positions for a Eu-free ZBLAN glass are additionally shown for comparison. Averaging the peak temperatures of the Eu-doped samples shows that Eu doping leads to higher temperatures for the transformation to the orthorhombic phase ( $T_{p2}=289$  °C for the Eu-free sample to  $\bar{T}_{p2}=294$  °C for

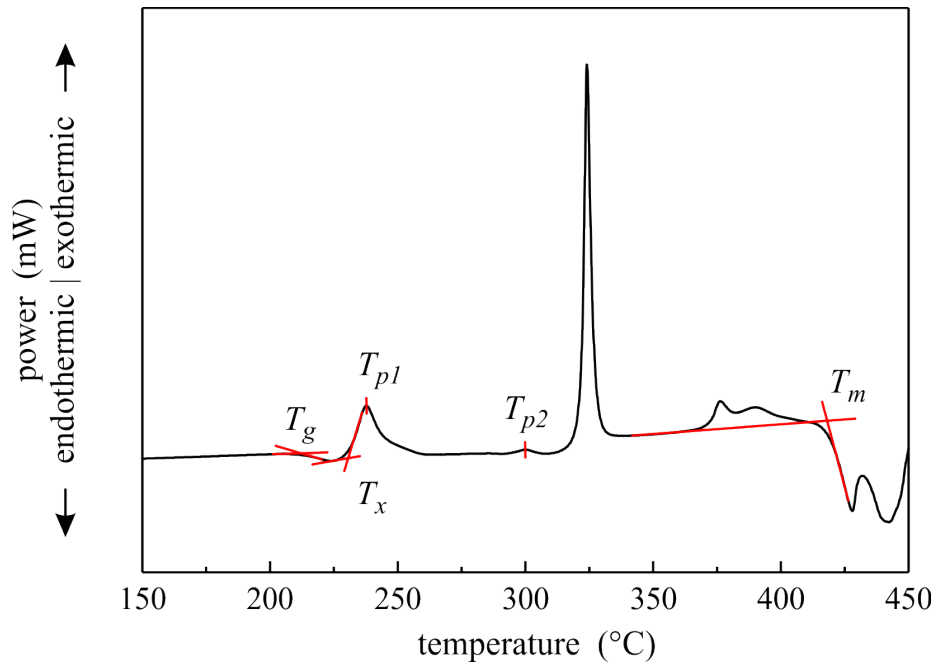


Figure 26: Plot of the DSC data for the FCZ glass with a  $\text{Eu}^{2+}$  fraction of 60%. The heating rate was 10 K/min.

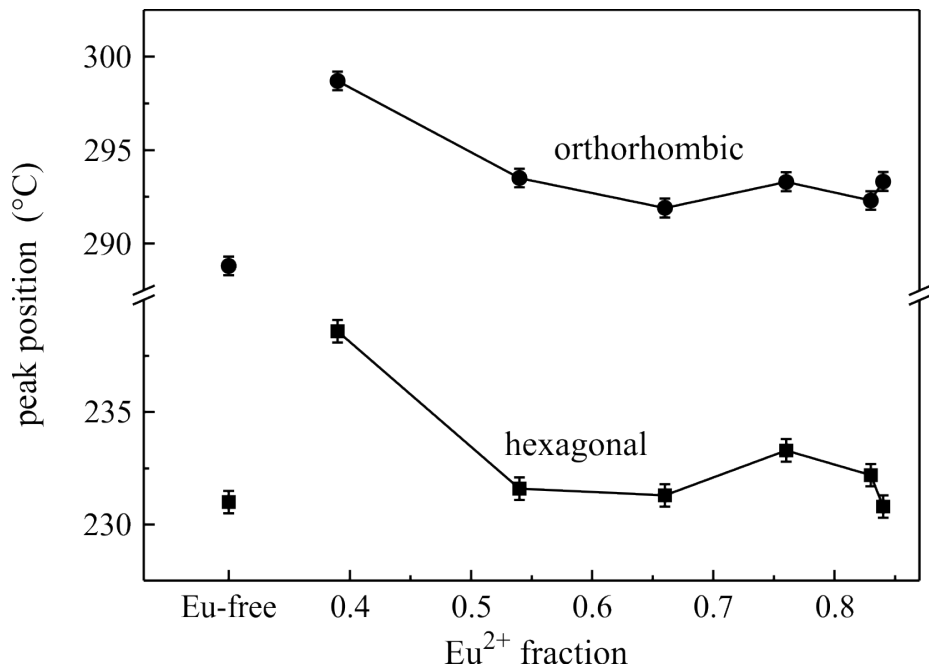


Figure 27: Crystallization peak position,  $T_p$ , for the hexagonal (squares) and the orthorhombic  $\text{BaCl}_2$  crystallization (circles) depending on the different  $\text{Eu}^{2+}$  doping fractions. The heating rate was 5 K/min. Data for a Eu-free ZBLAN glass is shown for comparison.

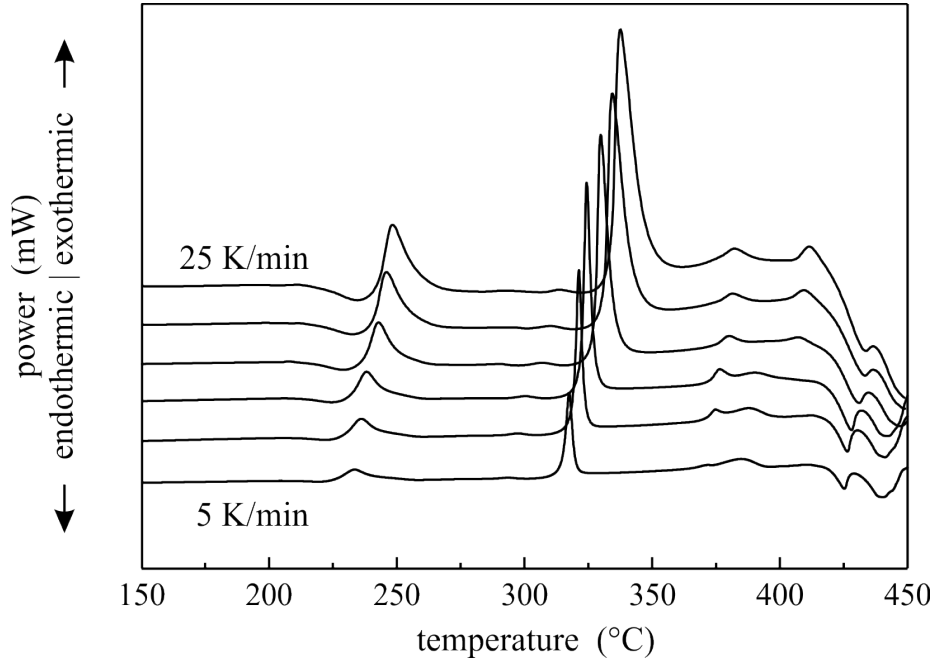


Figure 28: Plot of the DSC data for the FCZ glass with a  $\text{Eu}^{2+}$  fraction of 80%. The different heating rates go from 5, 7.5 and 10 to 25 K/min in steps of 5 K/min. The curves are vertically displaced for clarity.

the Eu-doped samples) than for the hexagonal phase crystallization ( $T_{p1}=231$  °C for the Eu-free sample to  $\bar{T}_{p1}=233$  °C for the Eu-doped samples). This behavior is described in more detail below.

DSC measurements with different heating rates,  $\alpha$ , enable the determination of the  $\text{BaCl}_2$  crystallization activation energy,  $E_a$ , by Kissinger's method [66]:

$$\frac{d \left[ \ln \left( \alpha / T_p^2 \right) \right]}{d \left( 1/T_p \right)} = - \frac{E_{a, \text{Kissinger}}}{R} \quad (14)$$

where  $R$  is the gas constant. With higher heating rates the crystallizations are shifted to higher temperatures; their peak intensities are increased due to an enhanced heat flow  $dH_c/dT$  into the samples (see Fig. 28), which is given by

$$dH_c/dT = m \cdot c_p \cdot \alpha \quad (15)$$

the product of sample mass  $m$ , sample specific heat capacity  $c_p$  and the constant heating rate  $\alpha$ . When plotting  $\ln \left( \alpha / T_p^2 \right)$  vs.  $(1/T_p)$  as shown in Fig. 29,  $E_a$  can be obtained from the slope of the linear fit. As 14 suggests, lower  $E_a$  values correspond to more stable glasses and a larger separation between  $T_p$  and  $T_g$ .

Figure 30 shows  $E_a$  versus varying the  $\text{Eu}^{2+}$  and  $\text{Eu}^{3+}$  doping fraction.  $E_a$  of the hexagonal phase is not sensitive for the different Eu oxidation states, but  $E_a$  of the hexagonal to orthorhombic phase transformation shows an increase with increasing  $\text{Eu}^{2+}$  amount, i. e., more energy is needed to initialize the transformation to orthorhombic crystal structure. However, some points trend

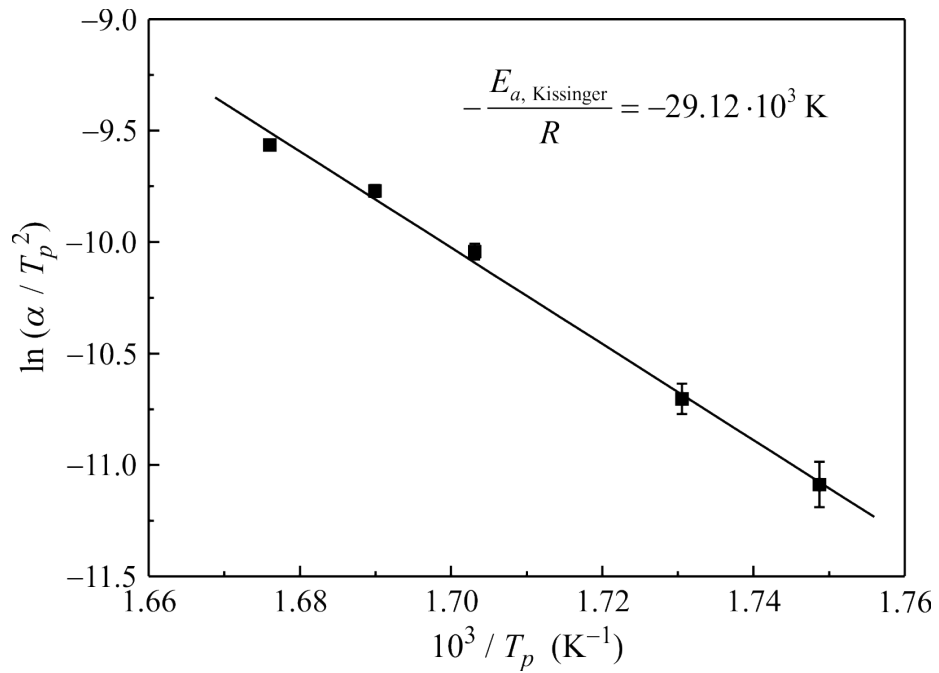


Figure 29: Fit for the pure  $\text{EuCl}_3$ -doped FCZ glass. The slope gives the apparent activation energy,  $E_a$ .

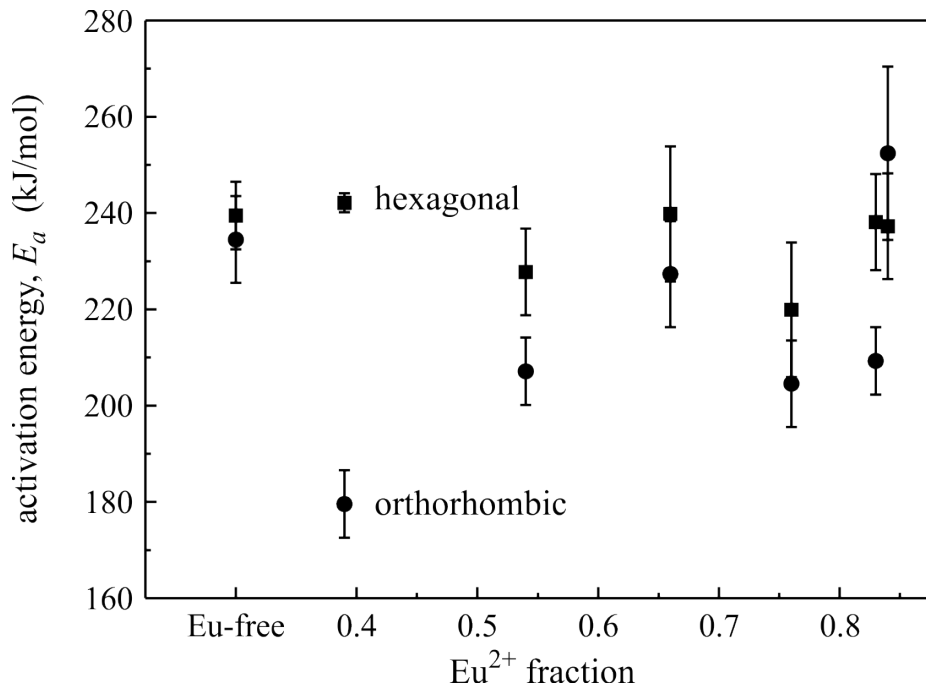


Figure 30: Activation energies,  $E_a$ , for the hexagonal (squares) and the orthorhombic (circles)  $\text{BaCl}_2$  crystallization obtained from the DSC data depending on the different  $\text{Eu}^{2+}$  and  $\text{Eu}^{3+}$  doping fractions. Data for a Eu-free ZBLAN glass is shown for comparison.

down, likely caused by composition inhomogeneities of the pieces coming from different sample positions. Compared to the pure  $\text{EuCl}_2$ -doped FCZ glass ( $\text{Cl}/(\text{Cl}+\text{F})=15.22\%$ ) the available  $\text{Cl}/(\text{Cl}+\text{F})$  amount in the melt is 0.6% higher for pure  $\text{EuCl}_3$  doping (15.81%), i. e., the small increase in the chlorine volume fraction for changing the Eu-doping from  $\text{Eu}^{2+}$  to  $\text{Eu}^{3+}$  might be the reason for the fact that the energy needed for the phase transformation decreases. Furthermore, photoluminescence measurements have shown, inter alia, that  $\text{Eu}^{2+}$  is incorporated into the  $\text{BaCl}_2$  nanocrystals, for example by a substitution of a  $\text{Ba}^{2+}$  site, while  $\text{Eu}^{3+}$  is not [10]. Therefore, another explanation for the phase transition influences will be given in the photoluminescence section later. Looking at the activation energies for the Eu-free ZBLAN, it is striking that the energies for both phases are within the error ( $E_{a,\text{hex.}}=240 \pm 7$  kJ/mol and  $E_{a,\text{ortho.}}=235 \pm 9$  kJ/mol), while there is a huge difference between the hexagonal and the orthorhombic crystallization energy for the various Eu-doped samples (the maximum difference is 63 kJ/mol for a  $\text{Eu}^{2+}$  fraction of 0.39). This difference decreases with increasing  $\text{Eu}^{2+}$  fraction.

### 4.3 X-RAY DIFFRACTION

Figure 31 shows a typical XRD pattern for a 2 mol%  $\text{EuCl}_3$ -doped FCZ glass. The as-poured glass does not show any crystalline phases, whereas annealing at 250 °C for 20 min leads to the formation of hexagonal phase  $\text{BaCl}_2$  nanocrystals (space group  $P\bar{6}2m$  (189), see bottom bar pattern). Whereas up to an annealing temperature of 270 °C only diffraction peaks related to hexagonal  $\text{BaCl}_2$  are detectable, a phase transition to the orthorhombic  $\text{BaCl}_2$  structure (space group  $Pnma$  (62), see top bar pattern) can be observed upon annealing at 290 °C. In addition, two reflections arise at 26.3° and 50.1°, which are not yet identified.

Figure 32 focuses on the crystalline phases and their transition temperatures for different  $\text{Eu}^{2+}$  fractions. It can be seen that the temperature at which the phase transition from hexagonal to orthorhombic structure occurs, depends on the Eu valence, i.e., a higher amount of divalent Eu leads to a less stable hexagonal  $\text{BaCl}_2$  phase. When doped with nominally pure  $\text{EuCl}_2$ , a phase transition from hexagonal to orthorhombic structure is completed at 270 °C. For  $\text{Eu}^{2+}$  fractions between 54% and 83% the transition takes place at 280 °C, whereas, for pure 2 mol%  $\text{EuCl}_3$  doping, a fully transformed orthorhombic  $\text{BaCl}_2$  phase is not found before annealing at 290 °C for 20 min. In comparison to the chlorides, the fluorides (not shown for reasons of clarity) show that the phase transition takes place at a higher temperature.

Figure 33 shows XRD patterns of an  $\text{Eu}^{2+}$ - $\text{Eu}^{3+}$  fluoride FCZ glass series annealed at 270 °C for 20 min. Compared to the nominal 100%  $\text{EuCl}_2$ -doped sample, which already shows a completely orthorhombic  $\text{BaCl}_2$  phase at 270 °C, the nominal 100%  $\text{EuF}_2$ -doped glass still contains a clear measurable amount of both phases. Furthermore, within the fluoride series a phase mixture at 270 °C is not observed prior to 40%  $\text{Eu}^{2+}$  being present, whereas it is observed at 20% within the chloride series. Because the base-glass compositions (except  $\text{Eu}^{2+}$  and

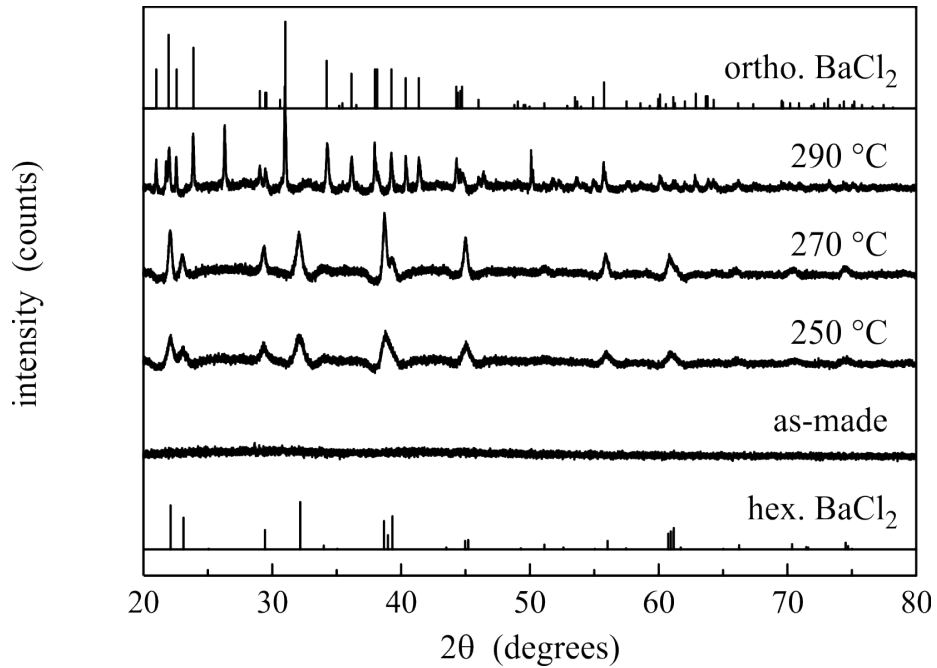


Figure 31: XRD patterns of a pure 2 mol% EuCl<sub>3</sub>-doped FCZ glass as-made and annealed at temperatures from 250 °C to 290 °C for 20 min. The XRD patterns of hexagonal (bottom, PDF 00-45-1313) and orthorhombic BaCl<sub>2</sub> (top, PDF 00-24-0094) are shown for comparison.

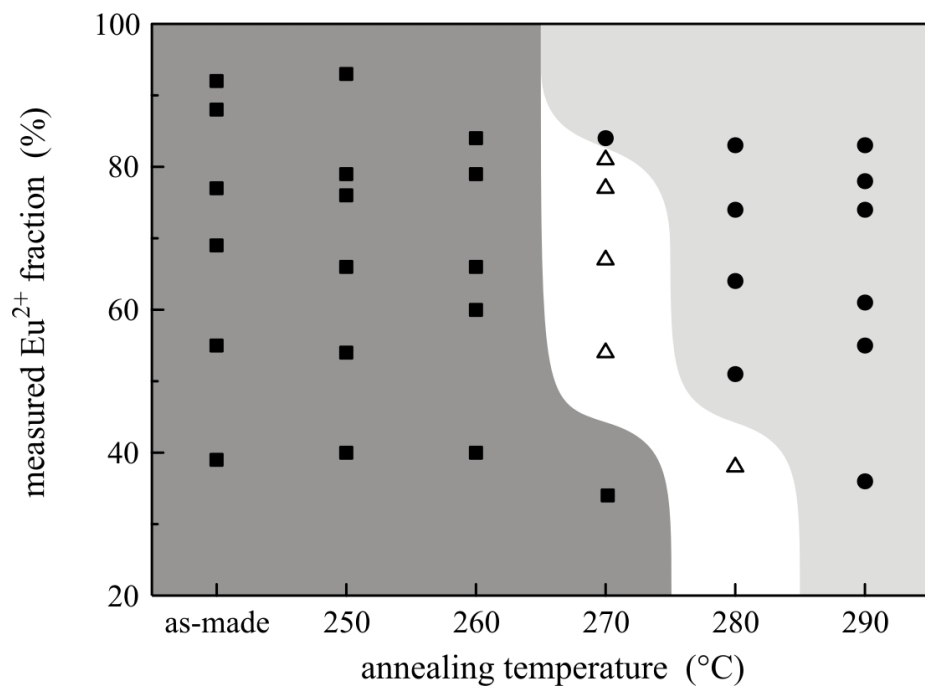


Figure 32: BaCl<sub>2</sub> nanocrystal phases depending on the Eu valence fraction and annealing temperature of the chloride (solid symbols) series: hexagonal phase (squares), mixed phase (open triangles), and orthorhombic phase (circles).

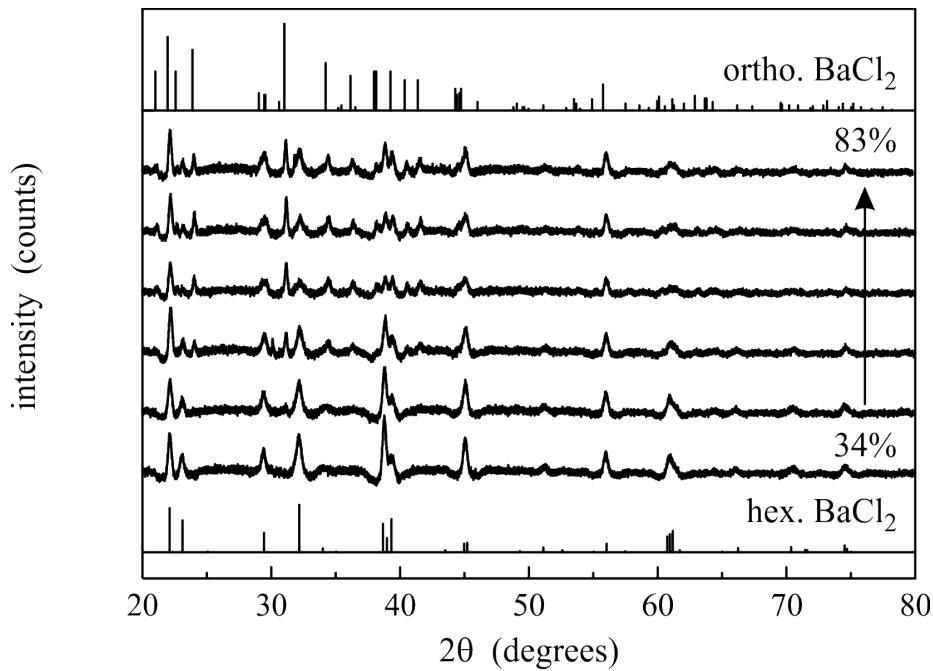


Figure 33: XRD patterns of an  $\text{Eu}^{2+}$ - $\text{Eu}^{3+}$  fluoride FCZ glass series annealed at  $270\text{ }^{\circ}\text{C}$  for 20 min. The percentages correspond to the measured  $\text{Eu}^{2+}$  fraction of the total Eu doping. The XRD patterns of hexagonal (bottom, PDF 00-45-1313) and orthorhombic  $\text{BaCl}_2$  (top, PDF 00-24-0094) are shown for comparison.

$\text{Eu}^{3+}$  chlorides and fluorides) remain constant, there are two possible reasons for this behavior: First, because of the slightly decreased chlorine content in the Eu fluoride series, higher energies and temperatures are needed, respectively, to initiate the nucleation and phase transition. Second, the XANES measurements show that, compared to the chloride series, the  $\text{Eu}^{3+}$  in the fluoride series is more stable for the same melting process. From the previous results on chlorides (see Fig. 25) it is known that a lower amount of  $\text{Eu}^{2+}$  leads to a more stable hexagonal  $\text{BaCl}_2$  phase, explaining the later phase transition at higher temperatures for the fluoride series.

As already introduced in the previous chapter, the reflection analysis function of the *DIFFRACplus EVA v1.2* XRD software is used to estimate the particle size with the Scherrer formula. Figure 34 shows an overview of the particle sizes for the (201) (hex. phase, squares) and the (211) (ortho. phase, circles) reflections and the unknown phase reflection at  $2\theta \approx 26.3^{\circ}$  (triangles) for the different FCZ glass doping ratios and annealing temperatures. As already shown in Ref. [10] an increase of the hexagonal crystallite size with increasing annealing temperature is observed for temperatures between  $250\text{ }^{\circ}\text{C}$  ( $d=13\pm 2\text{ nm}$ ) and  $270\text{ }^{\circ}\text{C}$  ( $d=26\pm 4\text{ nm}$ ). Different  $\text{Eu}^{2+}$ -to- $\text{Eu}^{3+}$  fractions do not influence the hexagonal  $\text{BaCl}_2$  nanocrystal sizes in between their respective annealing temperatures. However, for the pure  $\text{EuCl}_2$  sample annealed at  $270\text{ }^{\circ}\text{C}$ , the hexagonal phase completely disappears in favor of the orthorhombic proportion (for  $260\text{ }^{\circ}\text{C}$  no XRD data was available). A phase mixture is observed for  $\text{Eu}^{2+}$  fractions between 0.54 and 0.83; for a 0.39 fraction (maximum  $\text{Eu}^{3+}$  amount) only hexagonal phase particles are found. While the orthorhombic particle sizes fluctuate widely

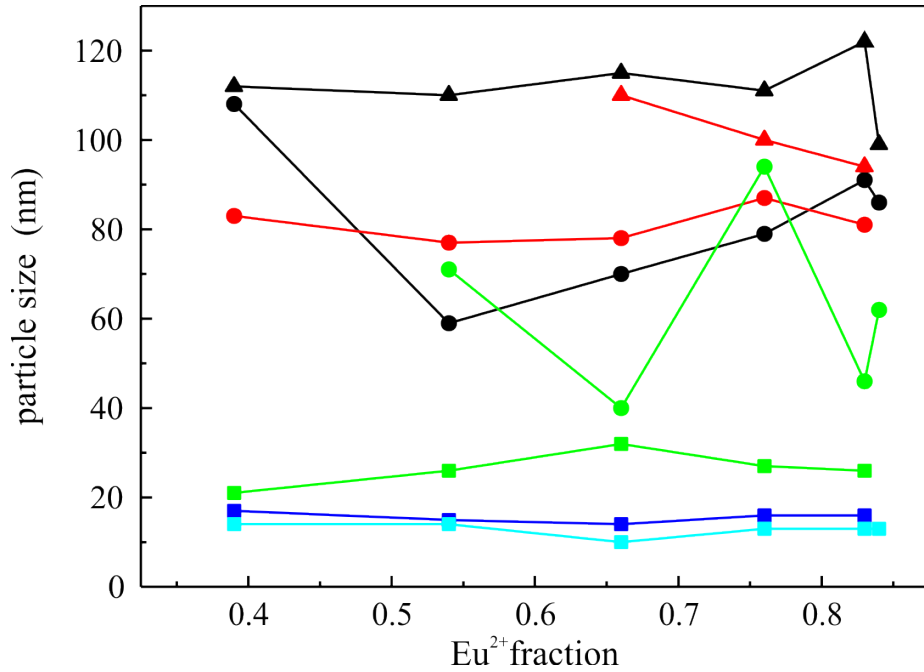


Figure 34: Particle sizes for the (201) (hexagonal  $\text{BaCl}_2$  phase, squares), the (211) (orthorhombic  $\text{BaCl}_2$  phase, circles) reflections and the unknown phase peak at  $2\theta \approx 26.3^\circ$  (triangles) for the different FCZ glass Eu valence fractions (chloride series) and annealing temperatures: 250 °C (cyan), 260 °C (blue), 270 °C (green), 280 °C (red) and 290 °C (black).

with an average diameter of  $d=70\pm 22$  nm, annealing at 280 °C for 20 min leads to a stable orthorhombic phase from 0.39 to 0.83  $\text{Eu}^{2+}$  fraction with an average diameter of  $d=81\pm 4$  nm (again for the pure  $\text{EuCl}_2$  sample no XRD data was available). No more hexagonal particles are found for this annealing condition, but the already mentioned unknown phase shows up for  $\text{Eu}^{2+}$  fractions above 0.66 with particle sizes of around 110 nm, which decrease with increasing  $\text{Eu}^{2+}$  amount to 94 nm for the 0.83 fraction. Since the unknown phase is not observed for low  $\text{Eu}^{2+}$  doping levels (fractions of 0.39 and 0.54), it looks like the Eu ions act as nucleation centers triggering the crystallization. However, the decrease in size with higher doping concentrations suggests that more crystal nuclei are produced during crystallization leading to smaller particles in greater quantities. Annealing at 290 °C for 20 min allocates enough energy for the unknown phase to precipitate with very small  $\text{Eu}^{2+}$  amounts. The particle size is nearly stable for  $\text{Eu}^{2+}$  fractions between 0.39 and 0.83 with an average diameter of  $d=114\pm 5$  nm implying a fully crystallized phase under these conditions. For nominal pure  $\text{EuCl}_2$  doping (fraction of 0.84) a decrease to 99 nm is observed. This may be caused by an energetically preferred orthorhombic phase due to a lower  $\text{BaCl}_2$  crystallization activation energy for the pure  $\text{EuCl}_2$ -doped FCZ glass. At the same time, this could mean that the unknown phase consists of barium and/or chlorine compounds with a crystal structure other than the orthorhombic one.

In addition to the unknown crystals, orthorhombic  $\text{BaCl}_2$  particles are present for all Eu-doped samples held at 290 °C. The averaged diameter is  $d=82\pm 17$  nm, which is smaller than the value of the unknown phase. However, the size

develops differently with increased  $\text{Eu}^{2+}$  content: for fractions between 0.39 and 0.54, a rapid decrease from 108 to 59 nm occurs and after that a monotonic increase for  $\text{Eu}^{2+}$  fractions between 0.54 and 0.83 up to 91 nm is observed. For the nominally pure  $\text{EuCl}_2$ -doped FCZ glass, the averaged size stagnates or slightly decreases to 86 nm. It appears that a few  $\text{Eu}^{2+}$  ions acts as nucleation sites and thus larger crystals can grow due to inert surroundings and volume quenching effects, respectively. Again the rapid decrease in size for the  $\text{Eu}^{2+}$  fraction of 0.54 may be caused by more available nucleation grains for crystallization, leading to a higher number of smaller particles. The size monotonically increases with higher  $\text{Eu}^{2+}$  content caused later by the decreasing distance between individual particles resulting in the so-called Ostwald ripening effect, where small crystals dissolve and redeposit onto larger crystals. The slight decrease in size for the nominal pure  $\text{Eu}^{2+}$  glass can be correlated with the decrease in the  $\text{BaCl}_2$  crystallization activation energy, leading to many more nucleation sites from the metastable phase, which on average reduce the mean crystal size.

#### 4.4 PHOTOLUMINESCENCE

$\text{BaCl}_2$  nanocrystal structure sensitive PL spectra of differently annealed and differently  $\text{Eu}^{2+}/\text{Eu}^{3+}$ -doped FCZ samples are plotted in Fig. 35. The samples were annealed for 20 min at temperatures between 250 and 290 °C. Again the samples were excited in the ultraviolet spectral range at 280 nm and all spectra were normalized to their most intense emission. All samples annealed at 250 °C (dashed-dotted curves) show the typical 5d-4f transition PL peak of  $\text{Eu}^{2+}$  incorporated into hexagonal phase  $\text{BaCl}_2$  particles and the less intense emission at 475 nm, even the nominally 100%-doped  $\text{Eu}^{3+}$  sample which confirms the already discussed conversion mechanism from  $\text{Eu}^{3+}$  to  $\text{Eu}^{2+}$  during melting. When annealing up to 290 °C, the 475 nm band disappears for all different doping fractions as a result of the phase transformation from hexagonal to orthorhombic phase  $\text{BaCl}_2$ . However, there are differences in the emission spectra for the differently heat-treated samples such as peak position of the main PL peak and intensity of the second peak, which are in good correlation to the obtained nanocrystal phases:

The spectra of the nominally 100%-doped  $\text{Eu}^{3+}$  sample with measured 39%  $\text{Eu}^{2+}$  fraction (top left) show no significant differences between 250 °C and 270 °C annealing, both show the typical  $\text{Eu}^{2+}$  PL of the hexagonal nanocrystal phase. XRD has shown that annealing at 290 °C leads to the formation of orthorhombic phase  $\text{BaCl}_2$ . Here, the 405 nm band for 250 °C is shifted to 399 nm, the typical  $\text{Eu}^{2+}$  PL when embedded into orthorhombic bulk  $\text{BaCl}_2$ , while the 475 nm band disappears. At 394 nm a small dip in the  $\text{Eu}^{2+}$  emission band is observed, which is assigned to an  $\text{Eu}^{3+}$  absorption from the ground state  $^7\text{F}_0$  to state  $^5\text{L}_6$  [67]. Increasing the divalent doping fraction, this absorption decreases due to less  $\text{Eu}^{3+}$  in the glass. Furthermore, a higher  $\text{Eu}^{2+}$  fraction leads to a decrease in the peak intensity ratio  $I(475 \text{ nm})/I(405 \text{ nm})$ . The 475 nm peak of the 250 °C spectra is rising from 39%  $\text{Eu}^{2+}$  to 84%  $\text{Eu}^{2+}$  fraction. This confirms the theory of the impurity associated  $\text{Eu}^{2+}$  sites or clusters, which are more probable to form with higher  $\text{Eu}^{2+}$  amount.

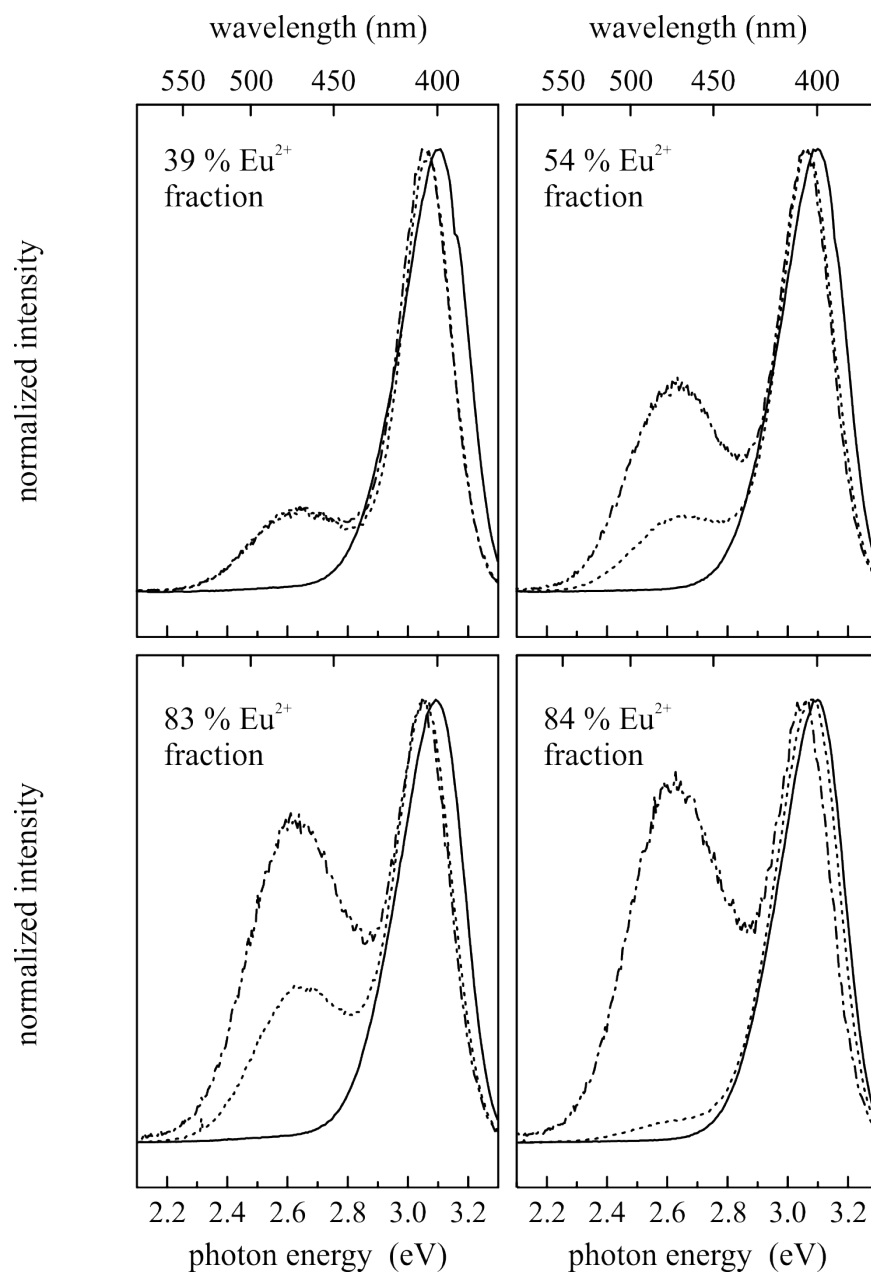


Figure 35: Normalized PL spectra for different  $\text{Eu}^{2+}$  fractions (measured with XANES) in FCZ glass ceramics and annealed at 250 (dashed-dotted), 270 (dotted), and 290 °C (solid curve) for 20 min. The PL was excited at 280 nm.

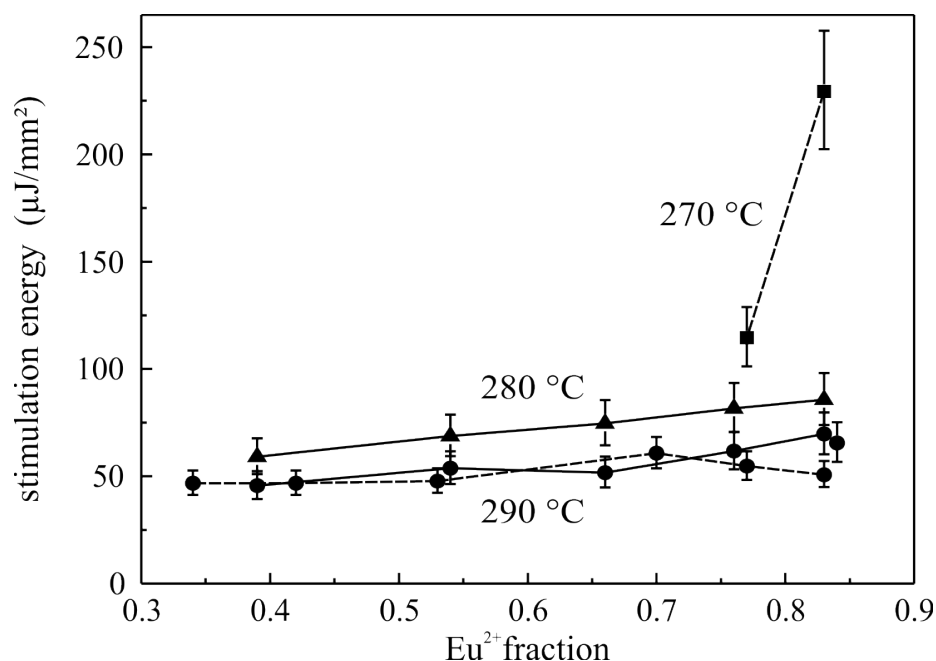


Figure 36: Stimulation energy for different  $\text{Eu}^{2+}$  fractions in FCZ glass ceramics doped with  $\text{EuF}_2$  (dashed lines) or  $\text{EuCl}_2$  (solid lines) and annealed at 270 (squares), 280 (triangles), and 290 °C (circles) for 20 min.

The approximately 5 nm PL peak shift for the phase transition is also observed for the 84%  $\text{Eu}^{2+}$  sample (bottom right). However, in contrast to the lower  $\text{Eu}^{2+}$ -doped glass ceramics, here the 475 nm band is almost gone for 270 °C annealing, meaning that the hexagonal phase undergoes the phase transition to orthorhombic form at lower temperatures. This is also verified by the already discussed XRD results showing a higher amount of divalent Eu leads to a less stable hexagonal  $\text{BaCl}_2$  phase (see Fig. 32). The higher  $\text{Eu}^{2+}$  doping fraction probably results in a higher  $\text{Eu}^{2+}$  concentration in the nanocrystals causing an earlier hexagonal to orthorhombic phase transformation. At the same time, the larger number of impurities associated with  $\text{Eu}^{2+}$  sites or clusters disturbs the crystal transformation and is a possible explanation for the increase of the activation energy measured via DSC.

#### 4.5 PHOTOSTIMULATED LUMINESCENCE

To test the multivalent Eu series for its applicability as a storage phosphor, PSL measurements were performed at SUNY-Stony Brook, NY, USA. Figure 36 focuses on the SEs for different  $\text{Eu}^{2+}$  fractions in FCZ glass ceramics doped with  $\text{EuF}_2$  (dashed lines) or  $\text{EuCl}_2$  (solid lines) and annealed at 270 (squares), 280 (triangles), and 290 °C (circles) for 20 min. The error calculation can be found in the Appendix A. In order to detect PSL signals, annealing temperatures of at least 270 °C and high  $\text{Eu}^{2+}$  fractions above 77% are needed. For these 270 °C  $\text{EuF}_2$ -doped samples the highest energies ( $230 \mu\text{J}/\text{mm}^2$ ) are required to reduce the PSL intensity to  $1/e$  of its initial value, because in this samples the volume fraction of orthorhombic  $\text{BaCl}_2$  is still small compared to the ZBLAN glass matrix. With consistent annealing conditions, a higher  $\text{Eu}^{2+}$  fraction results in even higher required SEs.

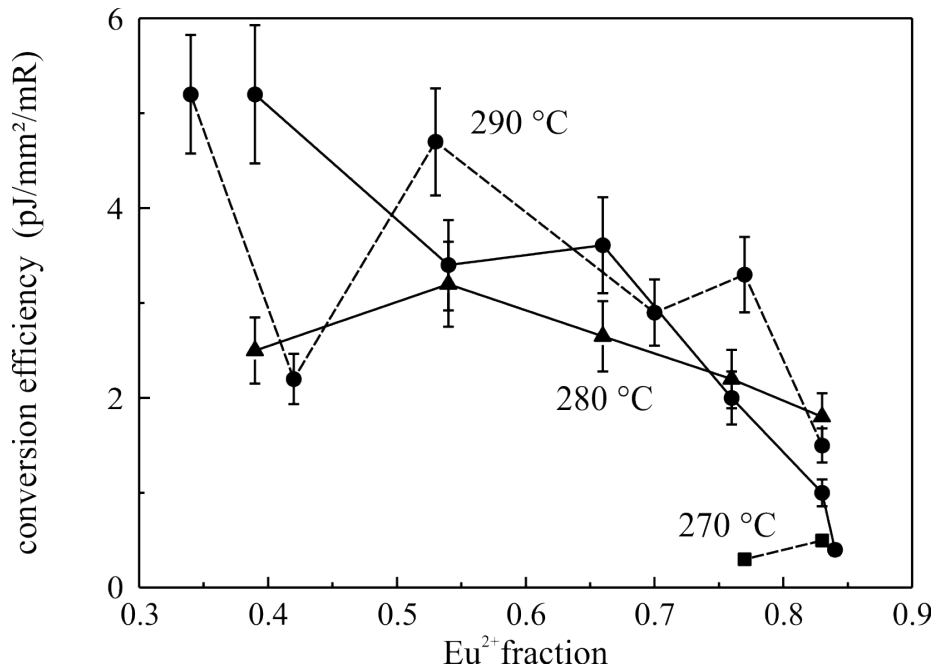


Figure 37: Conversion efficiency for different  $\text{Eu}^{2+}$  fractions in FCZ glass ceramics doped with  $\text{EuF}_2$  (dashed lines) or  $\text{EuCl}_2$  (solid lines) and annealed at 270 (squares), 280 (triangles), and 290 °C (circles) for 20 min.

All  $\text{EuCl}_2$ -doped samples annealed at 280 °C are PSL active and thus contain a sufficient amount of orthorhombic  $\text{BaCl}_2$ . In comparison to the  $\text{EuF}_2$ -doped glasses annealed at 270 °C, they already need significantly less SE, but also show a slight increase in SE (from 59 to 86  $\mu\text{J}/\text{mm}^2$ ) with an increasing  $\text{Eu}^{2+}$  fraction.

In the case of glasses annealed at 290 °C for 20 min, no significant differences are observed between the different materials,  $\text{EuF}_2$  and  $\text{EuCl}_2$ . Again, higher temperature leads to an overall decrease in SE, whereas an increasing  $\text{Eu}^{2+}$  fraction results in an energy increase. However, small negative slopes are observed at higher fractions above 70% for the  $\text{EuF}_2$  and above 80% for the  $\text{EuCl}_2$  series.

Figure 37 shows the calculated CEs for different  $\text{Eu}^{2+}$  fractions in FCZ glass ceramics doped with  $\text{EuF}_2$  (dashed lines) or  $\text{EuCl}_2$  (solid lines) and annealed at 270 (squares), 280 (triangles), and 290 °C (circles) for 20 min. The highest SE observed for the sample annealed at 270 °C and with the high  $\text{Eu}^{2+}$  fraction of 77% leads to the smallest CE of 0.3  $\text{pJ}/\text{mm}^2/\text{mR}$ . Vice versa, a lower SE leads to higher CE values for the multivalent Eu-doped FCZ glasses. Therefore, the CE increases with increasing annealing temperature from 270 (squares) to 290 °C. However, there is a decrease in CE observed for higher  $\text{Eu}^{2+}$  fractions. In particular, for fractions above 80% the CE of the samples being annealed at 290 °C drop below the values of the lower annealed samples. The outstanding value at 42%  $\text{Eu}^{2+}$  fraction belonging to the 290 °C (circles)  $\text{EuF}_2$  sample is considered to be a measurement artifact, because it does not fit into the trend. A comparison between fluoride and chloride series yields slightly higher CE values for the series doped with  $\text{EuF}_2$ .

## 4.6 DISCUSSION

XANES measurements show that, during the glass-melting process,  $\text{Eu}^{3+}$  is partially reduced to  $\text{Eu}^{2+}$ . Because the measured  $\text{Eu}^{2+}$  fraction in the glass saturates with higher doping ratio (only 13% difference between nominal 60% and 100%  $\text{Eu}^{2+}$  fraction), usage of the cheaper  $\text{EuCl}_3$  for this region would reduce costs without lowering the  $\text{Eu}^{2+}$  luminescence significantly. These results also show that europium chloride converts more  $\text{Eu}^{3+}$  into the divalent valence state than their fluoride counterparts. Furthermore, a slight oxidation of  $\text{Eu}^{2+}$  during annealing was observed. Therefore, it is recommended to heat treat the samples soon after the cutting and polishing steps.

The different chemical equilibria of the multivalent Eu-doped FCZ glass melts significantly influence the  $\text{BaCl}_2$  crystallization, which is important for luminescence output. XRD, PL and PSL measurements show that a higher amount of divalent Eu leads to an earlier (in terms of temperature) phase transition from hexagonal to orthorhombic  $\text{BaCl}_2$ . As XANES results suggest, the phase transition takes place at higher temperatures for Eu-fluoride compounds than for their chloride equivalents.

Examining the applicability of the multivalent Eu-doped ZBLAN glasses as storage phosphor imaging plates and comparing the gained SE and CE values with the most commercially used x-ray storage phosphor,  $\text{BaFBr:Eu}^{2+}$ , the FCZ glasses still cannot compete with the reference. The best working sample out of the series is the lowest  $\text{EuCl}_2$ -doped (39%) FCZ glass providing a SE of  $45.9 \mu\text{J}/\text{mm}^2$  which is a factor 3.4 higher than for BFB, and a CE of  $5.2 \text{ pJ}/\text{mm}^2/\text{mR}$ , which is a factor 4.6 worse. However, a very interesting observation is that for the multivalent Eu-doped FCZ glasses the conversion efficiency decreases with increasing  $\text{Eu}^{2+}$  fraction and decreasing  $\text{Eu}^{3+}$ , respectively. There are two possible explanations: The most likely one is that hole defects which are acting as localized electron traps for the meta stable e-h pairs are probably associated with  $\text{Eu}^{3+}$ . For bulk crystalline  $\text{BaCl}_2:\text{Eu}^{2+}$ , it was shown that the photostimulatable electron traps are  $F$  centers [68]. In Ref. [9] Schweizer *et al.* claim that  $F$  centers are also the photostimulatable traps in the glass ceramics, because the PSL stimulation spectra recorded in the FCZ glass ceramics and in  $\text{BaCl}_2$  powder occur in the same spectral range. However, they also found that a different or a perturbed  $F$  center is involved in the glass ceramic case, which probably is associated with  $\text{Eu}^{3+}$ . Therefore, a higher  $\text{Eu}^{3+}$  fraction causes more defects to be present in the glass matrix, leading to an increase in storage phosphor conversion. That phenomenon is also the reason for the  $\text{EuF}_2$  series providing the better conversion efficiency, because it is known from XANES that the  $\text{EuF}_2$  series contains a higher fraction of  $\text{Eu}^{3+}$  than the  $\text{EuCl}_2$  series.

The second possibility for the CE decrease with increasing  $\text{Eu}^{2+}$  fraction and decreasing  $\text{Eu}^{3+}$  is an energy self-quenching effect with too much  $\text{Eu}^{2+}$  similar to the  $\text{Eu}^{2+}$  quenching mechanism in as-made glasses without  $\text{BaCl}_2$  nanoparticles [9]. Increasing the  $\text{EuF}_2$  or  $\text{EuCl}_2$  content leads to smaller distances between neighbored  $\text{Eu}^{2+}$  ions making interactions and in particular a non-radiative

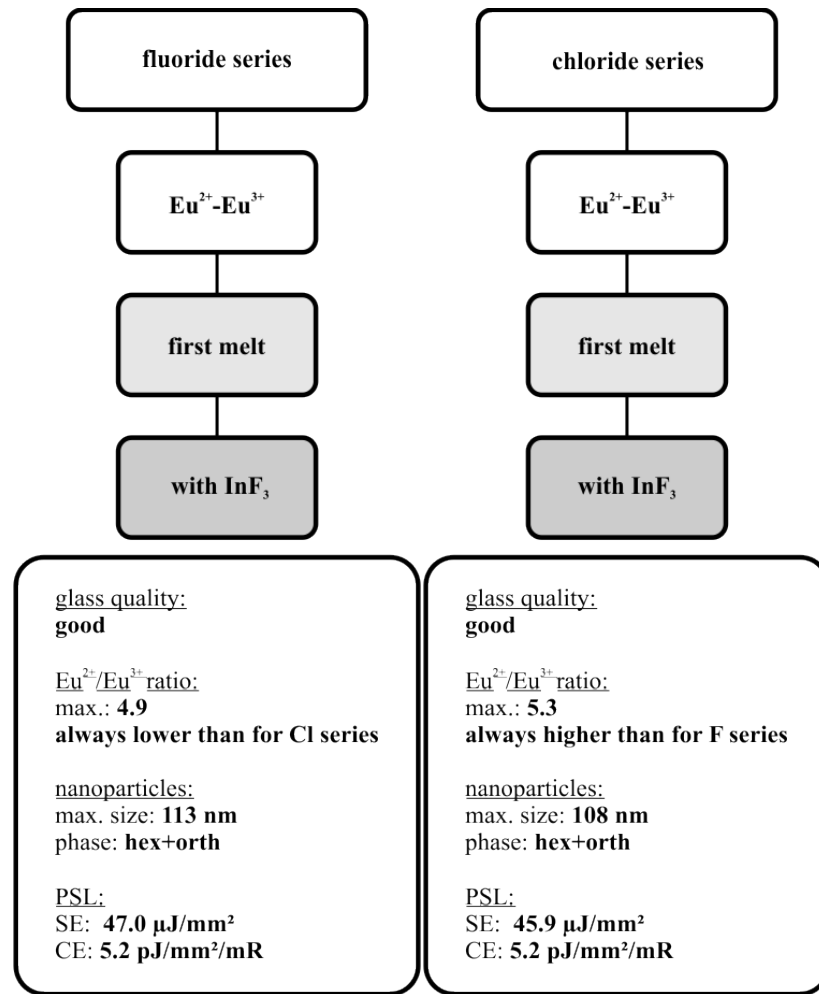


Figure 38: Final overview of the obtained results for the multivalent europium series.

energy transfer between the ions more probable. Less energy is stored and therefore the CE decreases.

In conclusion, in terms of a price reduction for image plates for medical diagnostics, multivalent Eu doping of ZBLAN glasses and glass ceramics could be a technically and financially feasible route. A final overview of the results is shown in Fig. 38.

$\text{Eu}^{2+}$  is not the only RE capable of being incorporated into  $\text{BaCl}_2$  nanocrystals leading to an enhanced fluorescence. Fluorescence investigations on  $\text{Nd}^{3+}$ -doped FCZ glasses indicate that some trivalent RE ions like  $\text{Nd}^{3+}$  ions can also be incorporated into the nanocrystals [69].

In an attempt to enhance light output, the  $\text{Eu}^{2+}$  glasses are additionally doped with a further RE, namely Gd, Nd, Yb, or Tb, to study possible energy transfer between the RE dopants and potential effects on the optical and structural properties. Preliminary investigations have shown that RE doping has a significant influence on the  $\text{BaCl}_2$  crystallization behavior: In  $\text{Eu}^{2+}$ -doped FCZ glasses, the  $\text{BaCl}_2$  crystallization energy is about 260 kJ/mol [70], while preliminary DSC work on 5 mol%  $\text{Nd}^{3+}$ -doped FCZ glasses yielded a crystallization energy of about 200 kJ/mol. Thus, a further RE may also affect the  $\text{BaCl}_2$  crystallization which is investigated in detail below. The RE doping level was 1 mol% for all glasses. XANES measurements were done to evaluate the influence of the RE co-dopants on the Eu valency. DSC experiments were performed to obtain thermal stability parameters and the activation energies of the dopant dependent  $\text{BaCl}_2$  crystallization. Some parts and figures of this chapter have appeared previously in [70, 71].

### 5.1 X-RAY ABSORPTION NEAR EDGE STRUCTURE

In order to investigate a possible influence of the different RE co-dopants on the Eu valency, XANES spectra of all samples were recorded around the Eu  $L_{\text{III}}$  edge and the  $\text{Eu}^{2+}$ -to- $\text{Eu}^{3+}$  ratios determined by building the relative intensity ratios of the two characteristic WLs of  $\text{Eu}^{2+}$  and  $\text{Eu}^{3+}$ . Figure 39 shows the  $\text{Eu}^{2+}$  fractions for the different RE co-dopants in FCZ glasses versus annealing temperature. All fractions lie in between 88 and 96%; for the untreated glasses the values differ only by 5%, which is probably caused by slight variations of the glass composition. Within all different annealing temperatures,  $\text{YbCl}_3$  doping shows the smallest  $\text{Eu}^{2+}$  fractions. Similar to the multivalent Eu series, the  $\text{Eu}^{2+}$  content shows a slight decrease when the annealing temperature is increased. Since these samples were also exposed to air before being heat treated, the decrease in the cases of Yb, Tb and Nd can be explained again by a small partial and diffusion-limited oxidation of  $\text{Eu}^{2+}$  on and near the oxygen-contaminated glass surfaces during the annealing step. However, Gd interestingly shows an opposite trend; the  $\text{Eu}^{2+}$  content increases from 90% for the untreated glass to 96% when the temperature is increased to 260 °C.

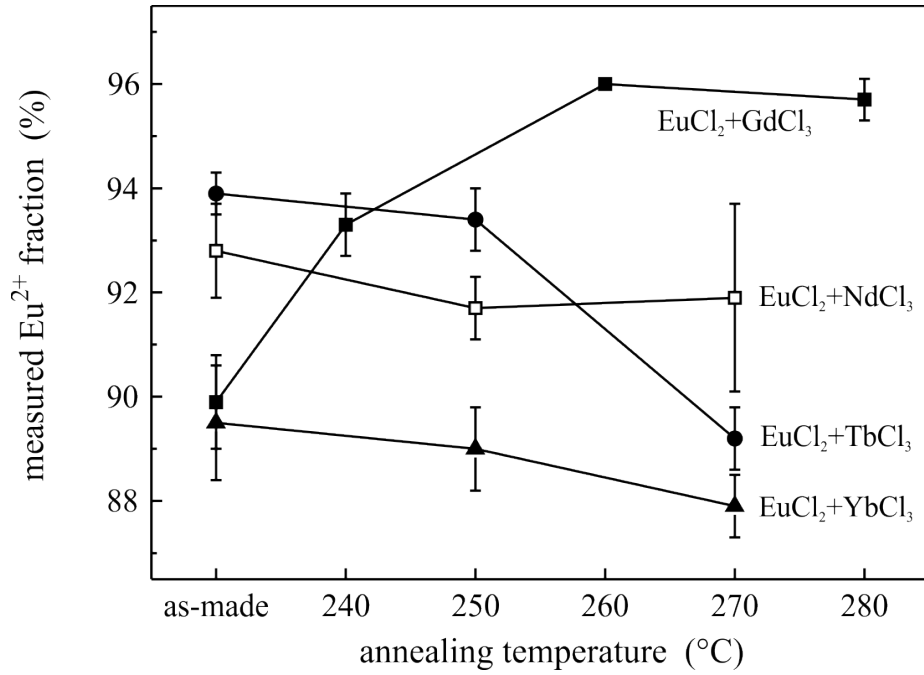


Figure 39: Measured  $\text{Eu}^{2+}$  fraction of the 1 mol%  $\text{XCl}_3$  ( $\text{X}=\text{Yb}$  (triangles),  $\text{Tb}$  (circles),  $\text{Nd}$  (open squares),  $\text{Gd}$  (filled squares))-1 mol%  $\text{EuCl}_2$ -doped FCZ glasses vs annealing temperature.

## 5.2 DIFFERENTIAL SCANNING CALORIMETRY

### 5.2.1 Preliminary Investigations

To investigate the influence of different trivalent rare-earths as potential co-dopant for  $\text{Eu}^{2+}$  on the  $\text{BaCl}_2$  crystallization,  $\text{Eu}^{3+}$ ,  $\text{Er}^{3+}$ ,  $\text{Gd}^{3+}$ ,  $\text{Nd}^{3+}$ , and  $\text{Tb}^{3+}$  single-doped FCZ glasses are studied first. The composition of these glasses consists of  $52\text{ZrF}_4\text{-}20\text{BaCl}_2\text{-}20\text{NaF}\text{-}3.5\text{LaF}_3\text{-}3\text{AlF}_3\text{-}0.5\text{InF}_3\text{-}1\text{REF}_3$  ( $\text{RE} = \text{Eu}^{3+}$ ,  $\text{Er}^{3+}$ ,  $\text{Gd}^{3+}$ ,  $\text{Tb}^{3+}$ ,  $\text{Nd}^{3+}$ ) (values in mole percent).

#### *Thermal Stability Parameters*

Figure 40 shows the DSC data for all trivalent RE dopants at a heating rate of 10 K/min. The results are assembled in Table 3 and show that the dopants have only a small effect on  $T_g$ , i.e.,  $\text{Gd}^{3+}$ -doped glass has the lowest value at 211 °C, while the glass transition temperatures for  $\text{Er}^{3+}$ - or  $\text{Tb}^{3+}$ -doped glasses are approximately the same as the undoped glass at 213 °C.  $\text{Nd}^{3+}$  has a  $T_g$  of 214 °C, while  $\text{Eu}^{3+}$  has the highest value at 216 °C. However, the onset and peak of the  $\text{BaCl}_2$  crystallization, as well as the melting temperature of the glass itself, show significant changes between the undoped and the RE-doped FCZ glasses: No doping leads to a  $T_x$  of  $\approx 234$  °C, while the values for the glasses with dopants are generally  $\approx 10$  °C higher (244 °C for  $\text{Er}^{3+}$  and 249 °C for  $\text{Nd}^{3+}$  and  $\text{Gd}^{3+}$ ). Similarly, the RE doping also leads to about a 10 °C shift of  $T_p$  from 239 °C to around 250 °C.

Table 3: Thermal stability parameters of RE-doped FCZ glasses for a heating rate of 10 K/min.  $T_g$ ,  $T_x$ ,  $T_p$ , and  $T_m$  are taken in Kelvin for the calculation of the thermal stability parameters. Furthermore the covalent radii [72] of the different RE ions are listed.

dopant	$T_g$ (°C)	$T_x$ (°C)	$T_p$ (°C)	$T_m$ (°C)	$T_g/T_m$	$H_r$	covalent radius (Å)
none	$212.7 \pm 0.5$	$234.3 \pm 0.5$	$239.2 \pm 0.5$	$418.5 \pm 0.5$	$0.703 \pm 0.001$	$0.117 \pm 0.006$	-
Nd <sup>3+</sup>	$214.2 \pm 0.5$	$248.8 \pm 0.5$	$254.4 \pm 0.5$	$435.5 \pm 0.5$	$0.688 \pm 0.001$	$0.185 \pm 0.006$	1.64
Eu <sup>3+</sup>	$215.6 \pm 0.5$	$245.0 \pm 0.5$	$250.7 \pm 0.5$	$435.0 \pm 0.5$	$0.690 \pm 0.001$	$0.157 \pm 0.006$	1.85
Gd <sup>3+</sup>	$211.4 \pm 0.5$	$248.8 \pm 0.5$	$252.6 \pm 0.5$	$435.4 \pm 0.5$	$0.684 \pm 0.001$	$0.198 \pm 0.006$	1.61
Tb <sup>3+</sup>	$212.2 \pm 0.5$	$246.7 \pm 0.5$	$251.4 \pm 0.5$	$435.6 \pm 0.5$	$0.685 \pm 0.001$	$0.183 \pm 0.006$	1.59
Er <sup>3+</sup>	$212.5 \pm 0.5$	$244.0 \pm 0.5$	$248.8 \pm 0.5$	$435.4 \pm 0.5$	$0.685 \pm 0.001$	$0.164 \pm 0.006$	1.57

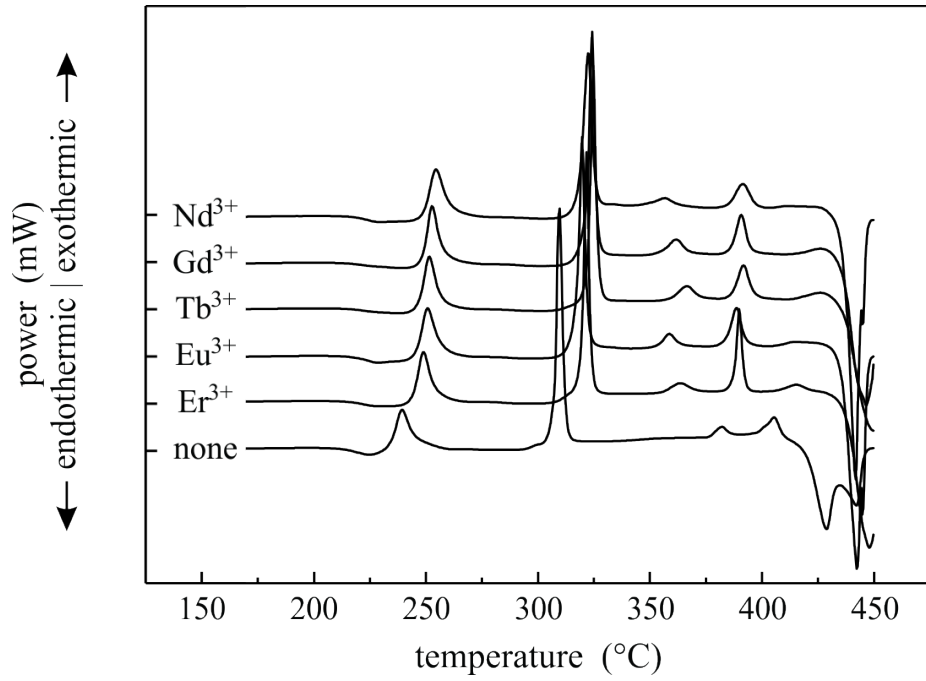


Figure 40: Plot of the DSC data for FCZ glasses with different RE doping. The heating rate was 10 K/min. The curves are vertically displaced for clarity.

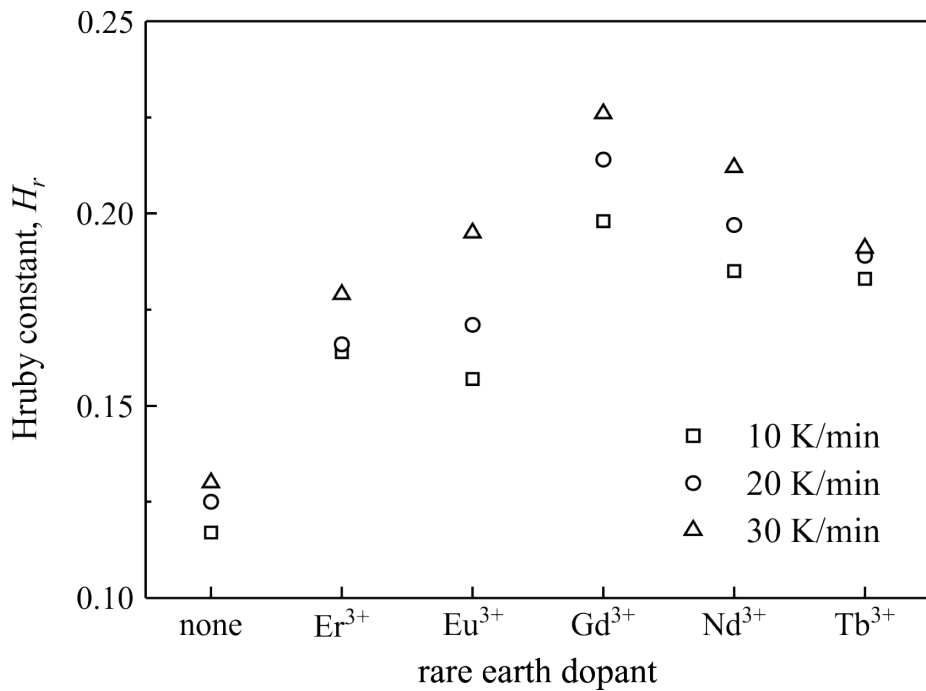


Figure 41: Hruby constant for differently RE-doped FCZ glasses and different heating rate  $\alpha$ .

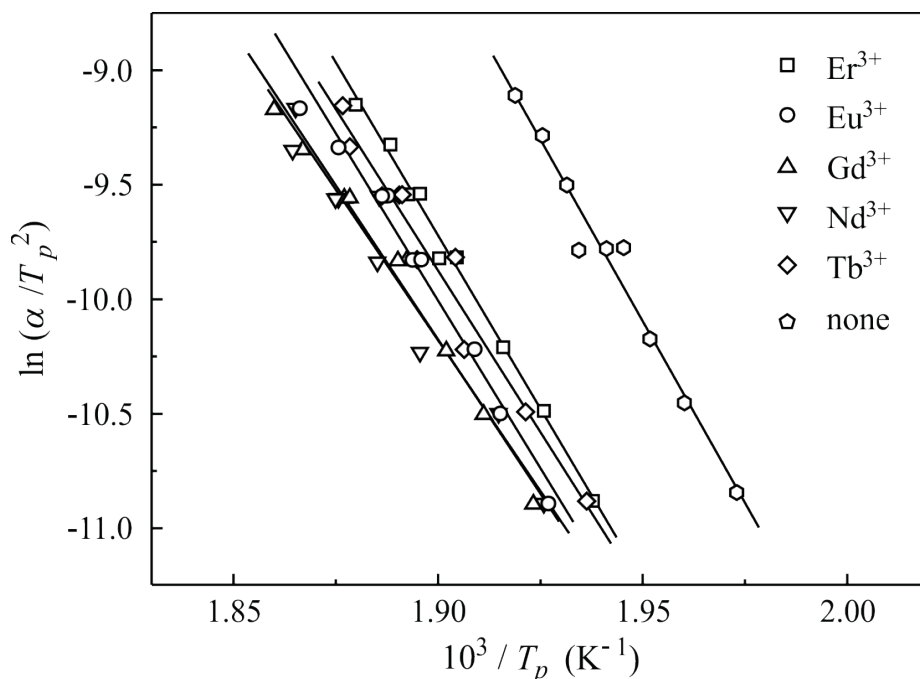


Figure 42:  $\ln(\alpha/T_p^2)$  vs.  $1/T_p$  for the differently RE-doped FCZ glasses. The slopes give the apparent activation energies  $E_a$ .

In addition, the individual dopant affects the position of  $T_p$ , i.e.  $\text{BaCl}_2$  crystallization starts at 249 °C in the  $\text{Er}^{3+}$ -doped glass, while for  $\text{Nd}^{3+}$  the peak position is reached at 254 °C. In contrast, doping results in a  $T_m$  of 435-436 °C, which is the same within error, and higher than the 419 °C observed in the undoped sample.

Figure 41 shows the Hruby constant  $H_r$  for the RE-doped FCZ glasses for different heating rates,  $\alpha$ . For all heating rates a significant gap is observed between the values of the undoped and the dopant-doped samples. In summary,  $\text{Gd}^{3+}$  has the highest  $H_r$  around 0.23, followed by  $\text{Nd}^{3+}$ ,  $\text{Tb}^{3+}$ ,  $\text{Eu}^{3+}$ , and lastly,  $\text{Er}^{3+}$ , with the lowest values between 0.16 and 0.18. The  $H_r$  mean value of 0.12 for the undoped glass is even smaller and therefore an indication that RE doping leads to higher glass stability against crystallization on heating, which is in good agreement with the higher values for  $T_x$  and  $T_p$  for the RE-doped glasses.

#### Apparent Activation Energies

Upon increasing heating rates from 5 to 25 K/min, shifts of the crystallization peak maxima of about 10 to 20 °C (depending on the dopant) to higher temperatures are observed from which the activation energy,  $E_a$ , of the  $\text{BaCl}_2$  crystallization can be determined by Kissinger's method (see 14).  $E_a$  is obtained from the slopes of the linear fits by plotting  $\ln(\alpha/T_p^2)$  vs.  $1/T_p$  as shown in Fig. 42. The results for all RE dopants are summarized in Fig. 43. Compared to the undoped FCZ glass, the addition of a RE decreases the activation energy from 264 kJ/mol to 219 kJ/mol for  $\text{Nd}^{3+}$  doping. Between these values  $\text{Gd}^{3+}$  has the second lowest value of 224 kJ/mol, followed by  $\text{Tb}^{3+}$  (235 kJ/mol) and  $\text{Eu}^{3+}$  (244 kJ/mol).  $\text{Er}^{3+}$  has the highest  $\text{BaCl}_2$  crystallization activation energy of the dopants at a value of 252 kJ/mol.

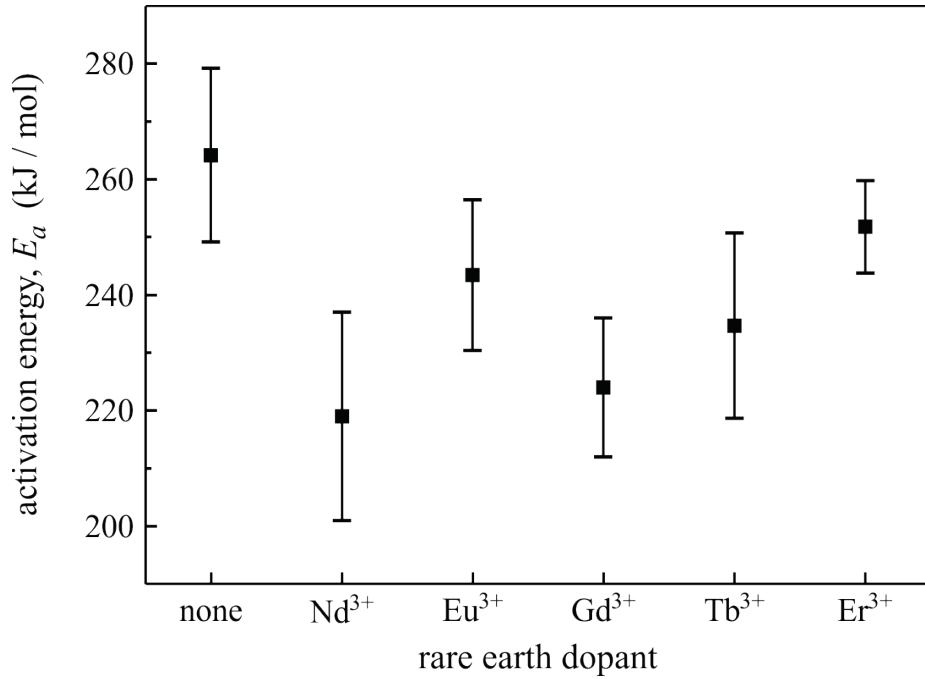


Figure 43: Activation energy  $E_a$  diagram for the  $\text{BaCl}_2$  crystallization for differently RE-doped FCZ glasses.

The ionic radius in RE atoms decreases with atomic number and activation energy increases as the ionic radius decreases, with the exception of europium. Covalent radius (the size of the atom that forms part of a covalent bond), also decreases with atomic number but in this case europium is the exception, having a larger covalent radius than the other dopants studied here, see Table 3 on page 59 or [72]. A covalent bond needs a bond dissociation energy (BDE) to be broken by homolysis (high frequency light or in our case heat treatment). Generally, a larger covalent radius results in a lower BDE. Previous investigations on RE-doped FCZ glasses showed that  $\text{Eu}^{2+}$  and  $\text{Nd}^{3+}$  ions are partially incorporated into the  $\text{BaCl}_2$  nanoparticles upon annealing, subsequent to pouring. In this step, a Ba ion is replaced by the RE ion, which was previously incorporated into the glass network or 'free' in the glass. It was shown in [73] that trivalent Eu is incorporated in the fluorozirconate glass network, but it is not clear that other RE ions behave in the same way. However, as  $\text{Eu}^{3+}$ -doped FCZ glasses yielded a much higher  $\text{BaCl}_2$  crystallization activation energy, it is possible that the other REs studied here are not bound to the glass network and therefore need less energy to diffuse and to act as a nucleation center.

### 5.2.2 Co-Doping Investigations

Figure 44 shows DSC data for the RE co-doped series and an undoped glass for comparison; the heating rate was 10 K/min. Beside the outstanding crystallization peaks for the  $\text{Gd}^{3+}$ -doped glass (see below), the shift of the  $\beta\text{-BaZrF}_6$  and  $\text{NaZrF}_5$  crystallization peak of the undoped sample to lower temperatures is striking. It confirms the recently found behavior that higher fluorine content (lower fluorine evaporation during the melting process) leads to a decrease in

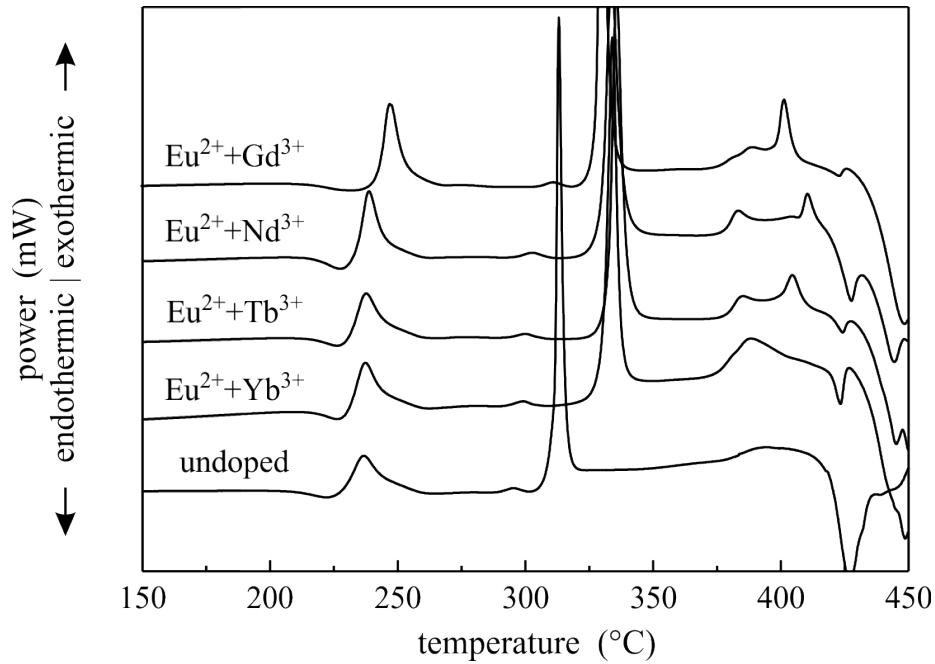


Figure 44: Plot of the DSC data for FCZ glasses with different RE co-dopants. The heating rate was 10 K/min. Data for an undoped ZBLAN glass is shown for comparison and the curves are vertically displaced for clarity.

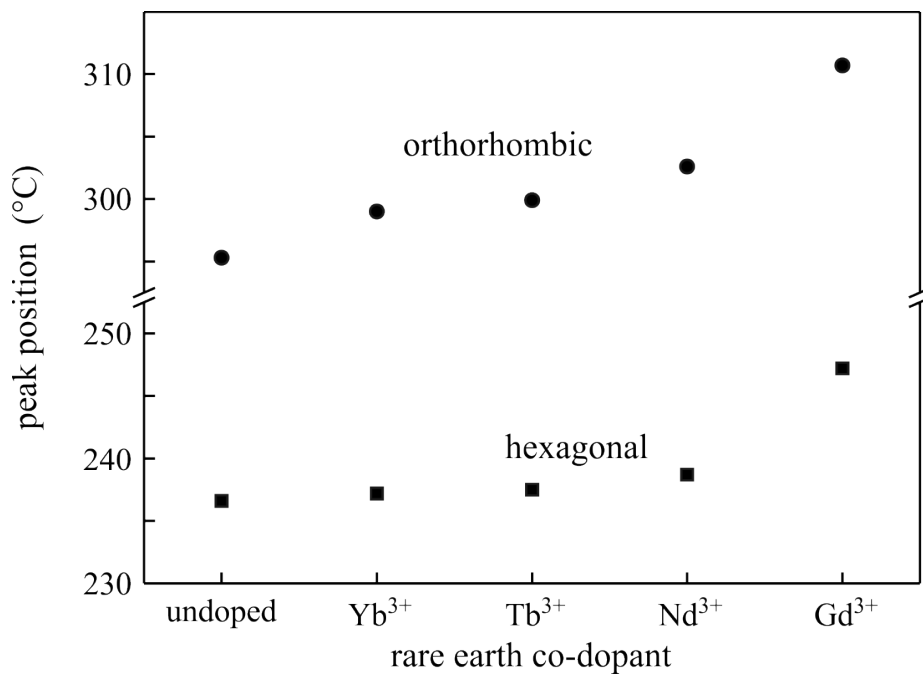


Figure 45: Crystallization peak position,  $T_p$ , for the hexagonal (squares) and the orthorhombic  $\text{BaCl}_2$  crystallization (circles) depending on the different RE co-dopants. The heating rate was 10 K/min. Data for an undoped ZBLAN glass is shown for comparison.

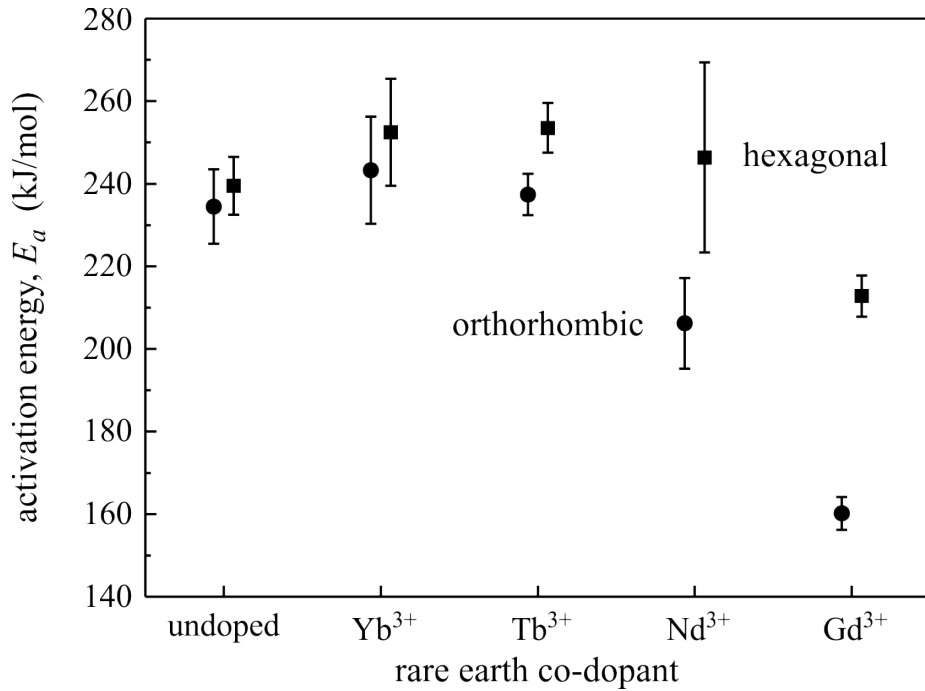


Figure 46: Hexagonal (squares) and orthorhombic (circles) BaCl<sub>2</sub> crystallization activation energies,  $E_a$ , obtained by Kissinger's method [66] for different RE co-dopants. Data for an undoped ZBLAN glass is shown for comparison.

peak temperature and an earlier crystallization, because more fluorine increases the probability for the crystals to form. Since the undoped sample was made as the only 20 g batch (the others were 10 g batches) less mass% of fluorine was lost during the same melting process. This was established by ion chromatography measurements. The averaged crystallization temperature is 334 °C for the RE-co-doped samples, while it is 313 °C for the undoped sample, i. e., the crystallization temperature is reduced by 21 °C. To give a clearer picture, the peak positions for hexagonal and orthorhombic phase crystallizations are also shown in Fig. 45. As mentioned earlier for the multivalent Eu series, the temperature difference between both crystallization peaks slightly increases when the sample is doped with RE ions. GdCl<sub>3</sub> as a co-dopant for EuCl<sub>2</sub> retards the nucleation and growth of BaCl<sub>2</sub> nanocrystals the most, as both crystal phases crystallize at the highest temperatures ( $T_{p1}(\text{Gd}^{3+})=247$  °C,  $T_{p2}(\text{Gd}^{3+})=311$  °C).

Looking at the crystallizations activation energies in Fig. 46, Gd<sup>3+</sup> is once again outlying: Both hexagonal and orthorhombic crystallization show a much lower activation energy than the undoped sample, especially for the orthorhombic crystallization with 160 kJ/mol compared to 235 kJ/mol for the undoped sample. Also the difference in the activation energy of the hexagonal and orthorhombic crystallization is considerable larger: For Gd<sup>3+</sup> it is 53 kJ/mol, while it is only 5 kJ/mol for the undoped sample. The difference decreases for the row Nd<sup>3+</sup> (40 kJ/mol) via Tb<sup>3+</sup> (17 kJ/mol) to Yb<sup>3+</sup> (10 kJ/mol).

## 5.3 X-RAY DIFFRACTION

Comparing the XRD patterns of all trivalent dopants for a fixed 20 min annealing at 270 °C (see Fig. 47),  $\text{Tb}^{3+}$  and  $\text{Yb}^{3+}$  show no significant differences concerning reflection position, height or FWHM, confirming the similar crystallization peak positions (see Fig. 45) and activation energies (see Fig. 46) obtained from the previously discussed DSC measurements and assuming a very similar  $\text{BaCl}_2$  orthorhombic crystal structure in both glasses. The diffraction pattern of  $\text{Nd}^{3+}$  shows less intense reflections, but an almost crystallized orthorhombic  $\text{BaCl}_2$  phase, while a retarded phase transformation is observed in case of  $\text{Gd}^{3+}$ . Here, the phase transition did not yet occur for the given heat treatment at 270 °C; all reflections can still be attributed to the hexagonal  $\text{BaCl}_2$  phase (bottom bar pattern PDF 00-45-1313). A more detailed view on the temperature dependent crystal structure is shown in Fig. 48 for the outstanding  $\text{Gd}^{3+}$ -doped FCZ glass. No crystalline  $\text{BaCl}_2$  reflections are observed for the glass as made, but annealing at 240 to 270 °C for 20 minutes leads to nucleation and growth of the hexagonal  $\text{BaCl}_2$  nanoparticles. Between 270 °C and 280 °C, the phase transformation begins and the XRD pattern for 280 °C shows a mixture of a small hexagonal and high orthorhombic  $\text{BaCl}_2$  fraction.

The reflection analysis function of the *DIFFRACplus EVA v1.2* XRD software is used to estimate the particle size. An overview of the particle sizes for the (201) (hexagonal  $\text{BaCl}_2$  phase, red) and the (211) (orthorhombic  $\text{BaCl}_2$  phase, blue) reflections for the 1 mol%  $\text{XCl}_3$  ( $\text{X}=\text{Yb}$  (triangles),  $\text{Tb}$  (circles),  $\text{Nd}$  (open squares),  $\text{Gd}$  (filled squares))-1 mol%  $\text{EuCl}_2$ -doped FCZ glasses is shown in Fig. 49. For all samples the typical increase of the crystallite size is observed for increasing annealing temperatures between 230 °C and 270 °C. Here, for  $\text{Yb}^{3+}$ ,  $\text{Tb}^{3+}$  and  $\text{Gd}^{3+}$  the mean particle sizes are nearly equal within the lower annealing temperatures from 230 °C to 250 °C and increase from 14 nm (230 °C) to 17 nm (250 °C). Increasing the temperature further to 260 °C,  $\text{Tb}^{3+}$  and  $\text{Yb}^{3+}$  again show a similar size increase for the hexagonal  $\text{BaCl}_2$  particles to 32 nm, while the particles for the glass doped with  $\text{Gd}^{3+}$  grow at a lower rate (22 nm at 260 °C). However, the  $\text{Nd}^{3+}$ -doped samples stand out resulting in 10-20 nm larger mean particle sizes for the hexagonal  $\text{BaCl}_2$  phase between 240 °C and 260 °C. Furthermore, from 250 °C to 260 °C the phase transformation from hexagonal to orthorhombic crystal structure appears for  $\text{Yb}^{3+}$ ,  $\text{Tb}^{3+}$  and  $\text{Nd}^{3+}$ , whereas for  $\text{Gd}^{3+}$  the orthorhombic phase is not observed before 270 °C.

While the samples doped with  $\text{Yb}^{3+}$ ,  $\text{Tb}^{3+}$  show slightly different particle sizes for the orthorhombic phase at 260 °C (55 nm for  $\text{Tb}^{3+}$  and 66 nm for  $\text{Yb}^{3+}$ ), the sizes are again similar for the samples annealed at 270 °C for 20 min (72 nm in case of  $\text{Tb}^{3+}$  and 75 nm in case of  $\text{Yb}^{3+}$  doping). The  $\text{Nd}^{3+}$ -doping leads to a huge diameter increase up to 99 nm for 260 °C and 113 nm for 270 °C annealing. In case of  $\text{Gd}^{3+}$  the size of the orthorhombic  $\text{BaCl}_2$  particles increases from 62 nm for 270 °C to 108 nm for 280 °C. Beside the orthorhombic  $\text{BaCl}_2$  phase, the higher annealed  $\text{Gd}^{3+}$ -doped samples are the only ones out of the co-doping series containing a still measurable and evaluable amount of hexagonal  $\text{BaCl}_2$  with mean particle sizes of 30 nm for 270 °C and 25 nm for 280 °C annealing. The reduced size could be associated to a dissolution or transformation of some hexagonal phase particles for building the orthorhombic phase structure.

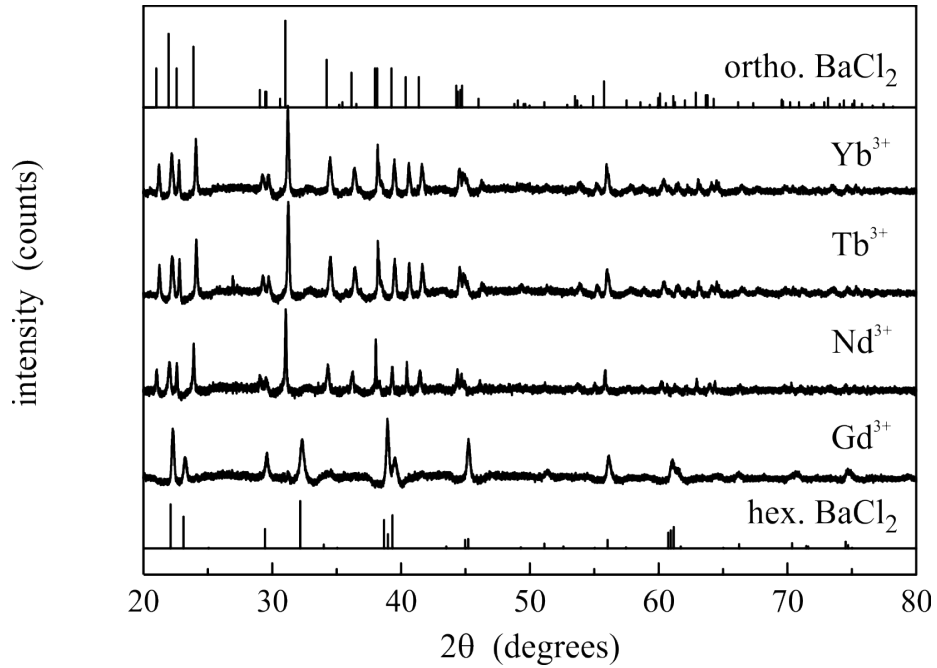


Figure 47: XRD patterns of a 1 mol% XCl<sub>3</sub> (X=Yb, Tb, Nd, Gd)-1 mol% EuCl<sub>2</sub>-doped FCZ glass annealed at 270 °C for 20 min. The XRD patterns of hexagonal (bottom, PDF 00-45-1313) and orthorhombic BaCl<sub>2</sub> (top, PDF 00-24-0094) are shown for comparison.

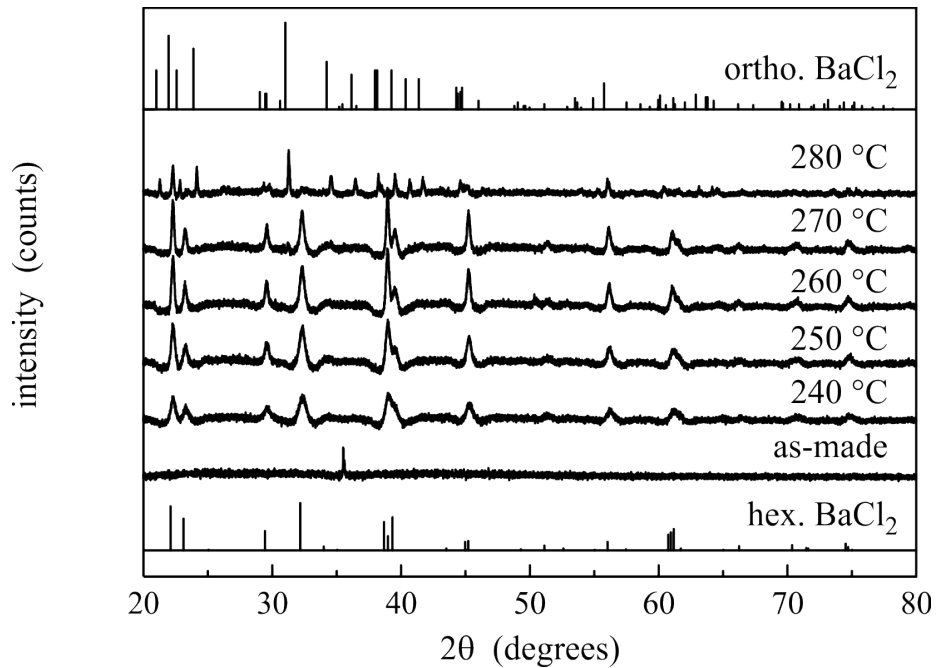


Figure 48: XRD patterns of a 1 mol% GdCl<sub>3</sub>-1 mol% EuCl<sub>2</sub>-doped FCZ glass as-made and annealed at temperatures from 230 °C to 270 °C for 20 min. The XRD patterns of hexagonal (bottom, PDF 00-45-1313) and orthorhombic BaCl<sub>2</sub> (top, PDF 00-24-0094) are shown for comparison.

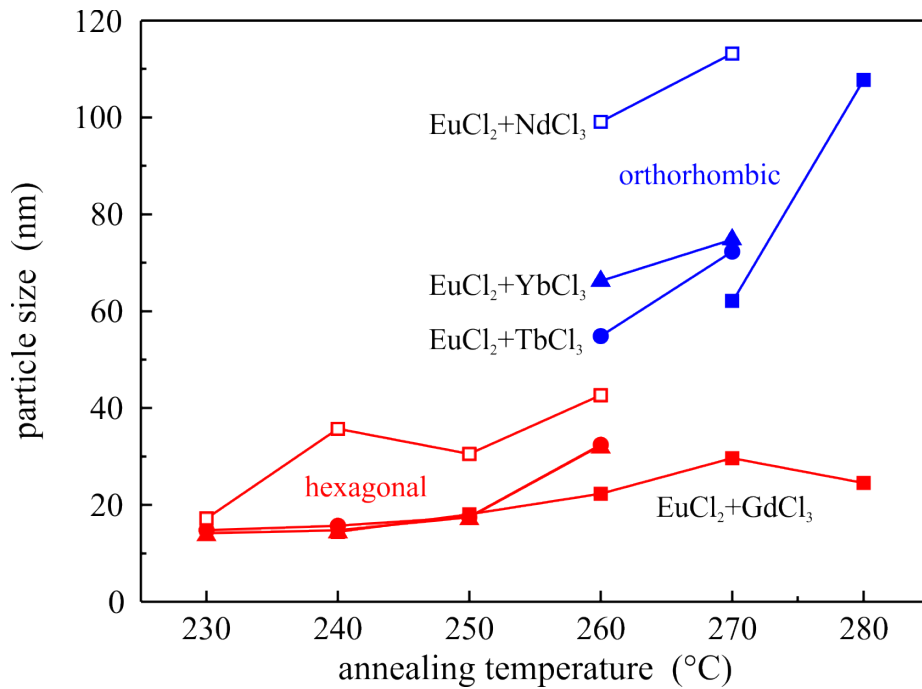


Figure 49: Particle sizes for the (201) (hexagonal  $\text{BaCl}_2$  phase, red) and the (211) (orthorhombic  $\text{BaCl}_2$  phase, blue) reflections for the 1 mol%  $\text{XCl}_3$  ( $\text{X}=\text{Yb}$  (triangles),  $\text{Tb}$  (circles),  $\text{Nd}$  (open squares),  $\text{Gd}$  (filled squares))-1 mol%  $\text{EuCl}_2$ -doped FCZ glasses.

#### 5.4 PHOTOLUMINESCENCE

Figure 50 shows an overview of the co-doped FCZ glasses annealed for 20 min at temperatures from 230 °C to 280 °C. The samples were excited at 254 nm with an UVGL-25 Compact UV Lamp from *UVP* and show strong luminescence in the blue spectral region.

As stated before, PL measurements are even more sensitive to the crystal structure and hence also used for this series to analyze the  $\text{BaCl}_2$  phase transformation in more detail. Normalized PL spectra of the RE co-doped FCZ glasses are plotted in Fig. 51. The samples were annealed for 20 minutes at temperatures between 250 and 280 °C. The  $\text{Eu}^{2+}$  luminescence was excited in the UV spectral range at 280 nm resulting in the typical 5d-4f luminescence at around 406 nm of  $\text{Eu}^{2+}$  incorporated into hexagonal phase  $\text{BaCl}_2$  particles and the less intense emission at 475 nm. In the upper two diagrams of Fig. 51 the co-dopants  $\text{Yb}^{3+}$  and  $\text{Tb}^{3+}$  show a very similar luminescence behavior over the whole annealing temperature range. The peak intensity ratios  $I(475 \text{ nm})/I(406 \text{ nm})$ , as well as the integrated signals, are almost equal within the same heat treatment setting. The decrease of the 475 nm peak at 260 °C is an indication for the phase change from hexagonal to orthorhombic phase  $\text{BaCl}_2$ . Again, the 406 nm band occurring for a 20 minute annealing at 250 °C is shifted to lower wavelengths and even below 400 nm when the phase transformation is completed at 270 °C; additionally the 475 nm band disappears.

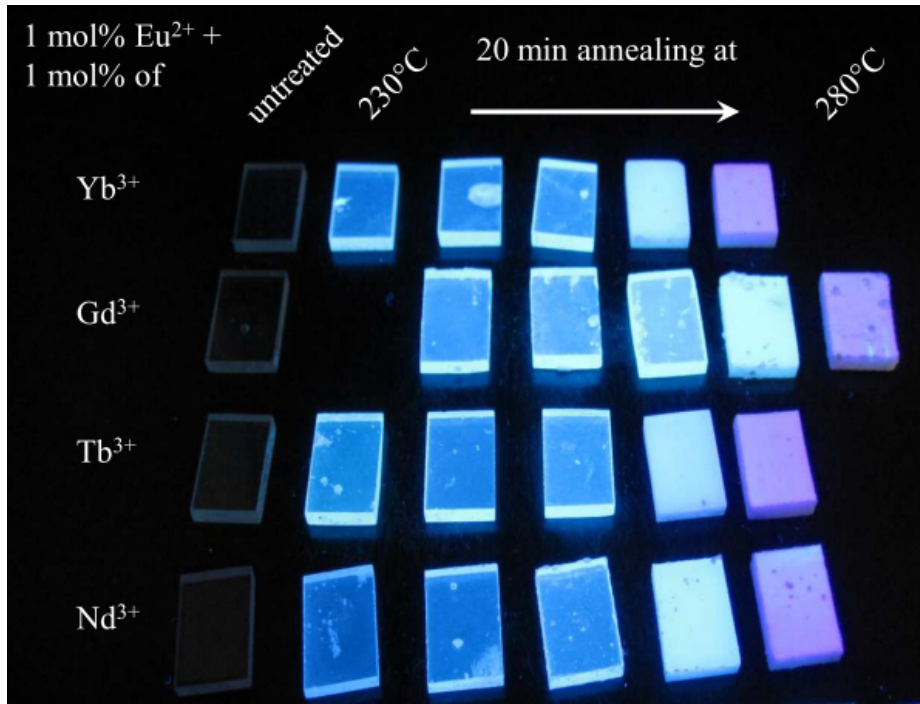


Figure 50: Overview of the co-doped FCZ glasses annealed for 20 min at temperatures from 230 °C to 280 °C in steps of 10 °C. The samples were excited at 254 nm with an UVGL-25 Compact UV Lamp from UVP.

The exchange of the trivalent Yb and Tb with Nd ions (bottom left) results in a decrease of the peak intensity ratios  $I(475 \text{ nm})/I(5d-4f)$ , being, with respect to the PL analysis in Chapter 4.4, a hint for a higher  $\text{Eu}^{2+}$  fraction inside the  $\text{BaCl}_2$  nanocrystals. The typical decrease in peak intensity ratio as well as the respective shift of the luminescence band to lower wavelength at higher annealing temperatures corresponding to the phase transformation from hexagonal to orthorhombic, is observed. Comparing the PL curve of the Nd-doped sample annealed at 270 °C with the curves for Yb and Tb (solid curves), there is still a weak signal of the 475 nm fluorescence band measurable assuming a small amount of hexagonal  $\text{BaCl}_2$  particles left; already small enough to not being recognized by the XRD measurements for the given integration time (see Fig. 47). However, this small difference in the signal between Yb/Tb and Nd can be explained by the slightly retarded crystallization and phase transformation of  $\text{Nd}^{3+}$  measured by DSC (see Fig. 45).

The luminescence of the  $\text{Gd}^{3+}$ -doped FCZ glass ceramics supports the outstanding discussed DSC and XRD data of this sample. The intensity of the 475 nm fluorescence band is comparable to that of  $\text{Nd}^{3+}$ , but the intensity decrease and the  $\text{BaCl}_2$  phase transformation at higher annealing temperatures, respectively, is more abrupt: The 475 nm band rapidly disappears for the sample annealed at 280 °C (dashed-double dotted curve), while no significant decrease is observed at temperatures below. Moreover, the 5d-4f luminescence band of the sample containing mainly orthorhombic particles has a noticeably higher FWHM value.

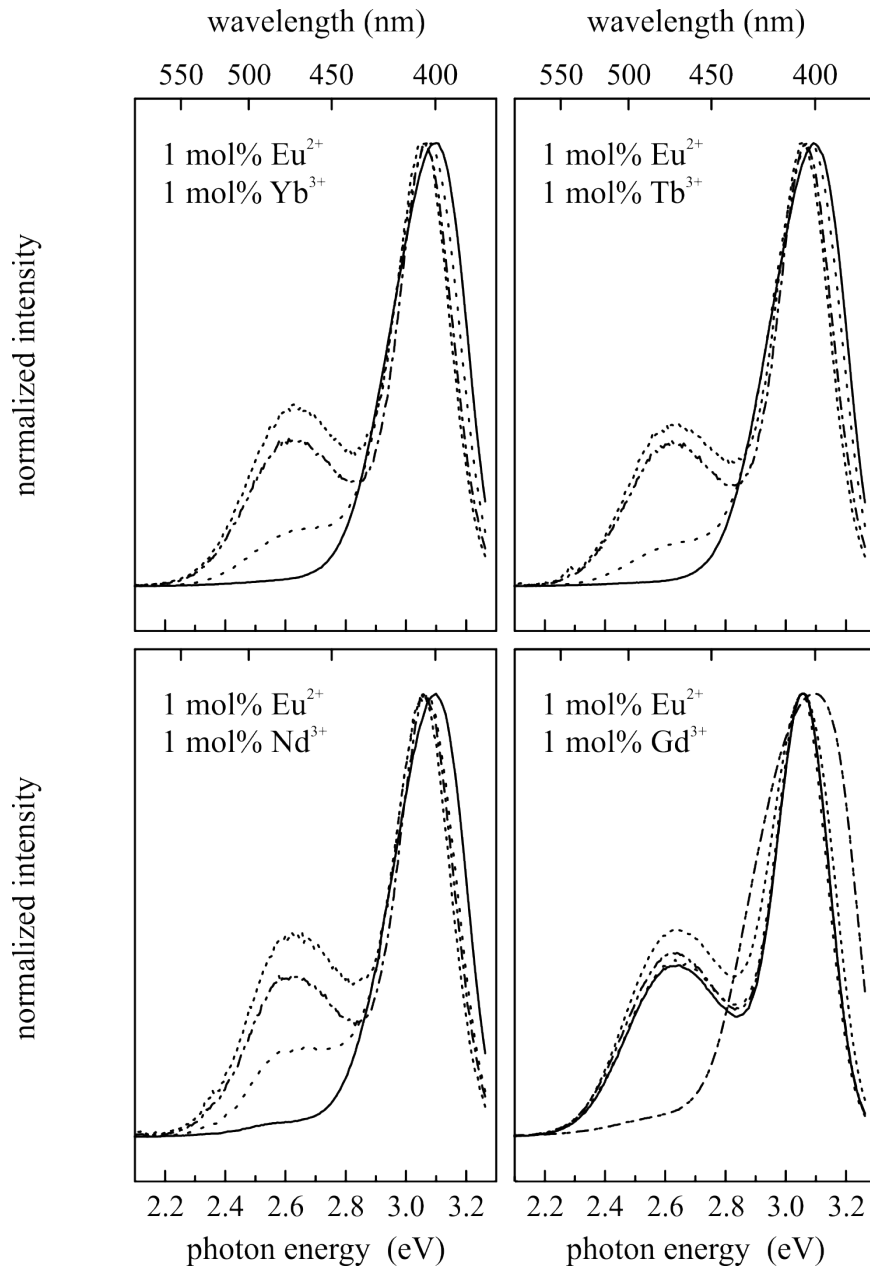


Figure 51: Normalized PL spectra for FCZ glasses with different RE co-dopants annealed at 240 (narrow dotted), 250 (dashed-dotted), 260 (wide dotted), 270 °C (solid curve) and at 280 °C (dashed-double dotted curve) for the  $Gd^{3+}$ -co-doped glass for 20 min. The PL was excited at 280 nm.

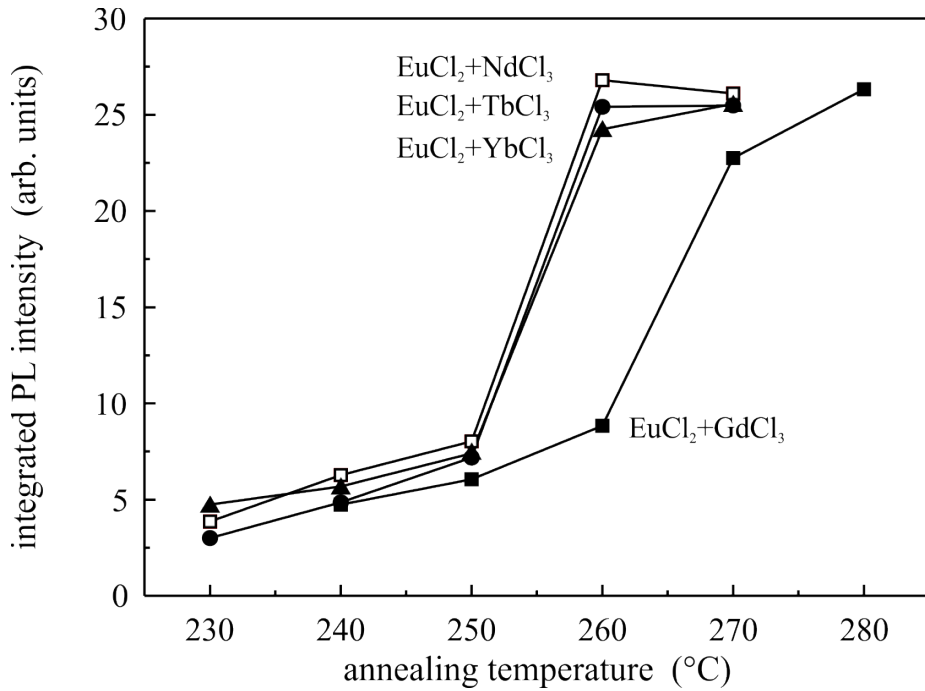


Figure 52: Integrated PL intensity between 370 and 700 nm for different post thermal treatments of the 1 mol%  $XCl_3$  ( $X=Yb$  (triangles),  $Tb$  (circles),  $Nd$  (open squares),  $Gd$  (filled squares))-1 mol%  $EuCl_2$ -doped FCZ glasses. The lines are a guide to the eye.

Figure 52 presents the above explained PL results in a more comparable way. The PL intensity of the RE co-doped FCZ glasses in Fig. 45 is integrated between 370 and 700 nm and then plotted for the different post thermal treatments. The integrals for  $Yb^{3+}$  (triangles),  $Tb^{3+}$  (circles) and  $Nd^{3+}$  (open squares)-doped samples are nearly of the same values and also show the same trend when the annealing temperature is increased from 230 °C to 270 °C: First, the integrated PL intensity increases with a slight positive slope from 230 °C to 250 °C, then the integrated intensities increase significantly by a factor of  $\approx 4$  from 250 °C to 260 °C, whereas from 260 °C to 270 °C a saturation for the  $Yb^{3+}$  and  $Tb^{3+}$ -doped FCZ glasses or even a small reduction of the integrated signal for the  $Nd^{3+}$ -doped FCZ glass is observed.

The integrated PL of the  $Eu^{2+}$ -doped samples co-doped with  $Gd^{3+}$  (filled squares) follows a different curve. It rises from 240 °C to 260 °C with a similar slope compared to the other co-dopants. Increasing the temperature further to 270 °C the slope steepens, but the integrated PL signal is still lower than the signal of the other co-dopants for this temperature. From 270 °C to 280 °C the integrated intensity increases to values which are similar to the intensities of the other co-dopants at 260 °C. Beside that, the slope lessens assuming a beginning saturation. In summary,  $Eu^{2+}$ -doped FCZ glasses which are additionally co-doped with  $Gd^{3+}$  need higher annealing temperatures to reach the same integrated PL intensity of the  $Yb^{3+}$ ,  $Tb^{3+}$  and  $Nd^{3+}$  co-dopants.

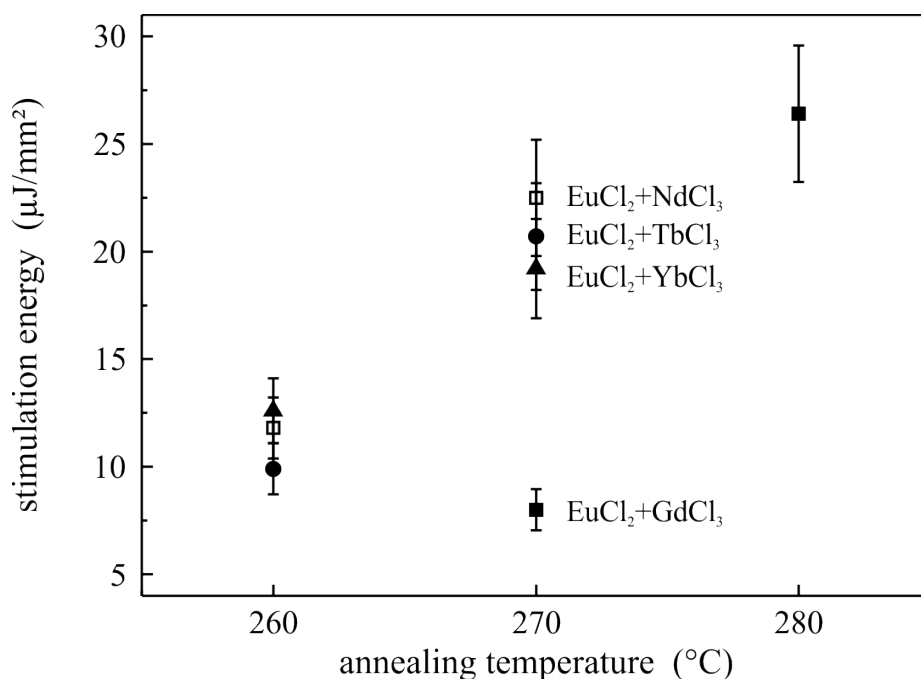


Figure 53: Stimulation energy for different post thermal treatments of the 1 mol%  $XCl_3$  ( $X=Yb$  (triangles),  $Tb$  (circles),  $Nd$  (open squares),  $Gd$  (filled squares))-1 mol%  $EuCl_2$ -doped FCZ glasses.

## 5.5 PHOTOSTIMULATED LUMINESCENCE

For imaging applications, the storage phosphor and PSL parameters, respectively, were measured and calculated for this series at SUNY-Stony Brook, NY, USA. Figure 53 shows the SEs for different post thermal treatments of the 1 mol%  $XCl_3$  ( $X=Yb$  (triangles),  $Tb$  (circles),  $Nd$  (open squares),  $Gd$  (filled squares))-1 mol%  $EuCl_2$ -doped FCZ glasses. A 20 minute heat treatment at 260 °C in case of  $Yb$ ,  $Tb$  and  $Nd$  co-doped glasses and at 270 °C in case of  $Gd$  as co-dopant, is required to obtain signal levels which are high enough compared to the noise to produce reliable results for the SE parameters. At 260 °C the SEs for the  $Yb$ ,  $Tb$  and  $Nd$  co-doped samples show no significant differences and are lying in the range of 10  $\mu J/mm^2$  and 13  $\mu J/mm^2$ . Similar values are also observed at 270 °C between 19  $\mu J/mm^2$  and 23  $\mu J/mm^2$ . However, the  $Gd$  co-doped glass annealed at 270 °C for 20 min shows a factor of 2 lower SE than for the other co-dopants. The sample annealed at 280 °C peaks at 26  $\mu J/mm^2$ . For this temperature no comparable data was available for the other REs.

Figure 54 shows the calculated CEs for different post thermal treatments of the 1 mol%  $XCl_3$  ( $X=Yb$  (triangles),  $Tb$  (circles),  $Nd$  (open squares),  $Gd$  (filled squares))-1 mol%  $EuCl_2$ -doped FCZ glasses. The weak PSL signals at 250 °C in case of  $Yb$ ,  $Tb$  and  $Nd$  co-doped glasses and at 260 °C in case of  $Gd$  as co-dopant result in CEs of about 0.03  $pJ/mm^2/mR$ . The CE generally increases with increasing annealing temperature caused by higher orthorhombic  $BaCl_2$  fractions in the glass matrix. At 260 °C the CEs of  $Yb$ ,  $Tb$  and  $Nd$  co-doped glasses lie between 1.2  $pJ/mm^2/mR$  and 1.6  $pJ/mm^2/mR$  and at 270 °C between

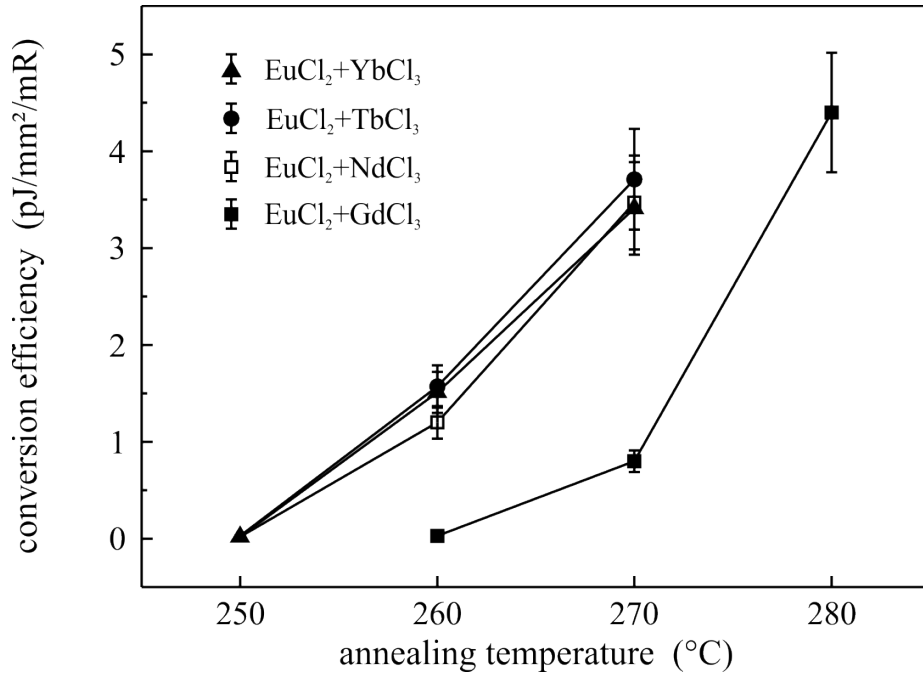


Figure 54: Conversion efficiency for different post thermal treatments of the 1 mol% XCl<sub>3</sub> (X=Yb (triangles), Tb (circles), Nd (open squares), Gd (filled squares))-1 mol% EuCl<sub>2</sub>-doped FCZ glasses. The lines are a guide to the eye.

3.4 pJ/mm<sup>2</sup>/mR and 3.7 pJ/mm<sup>2</sup>/mR. The Gd co-doped glasses annealed at the same temperatures show a significant lower CE than the other co-dopants with 0.03 pJ/mm<sup>2</sup>/mR at 260 °C and 0.8 pJ/mm<sup>2</sup>/mR at 270 °C. At the highest temperature of 280 °C the highest CE of this series is reached with 4.4 pJ/mm<sup>2</sup>/mR.

## 5.6 DISCUSSION

Prior DSC measurements of each glass ceramic were essential to be able to optimize the annealing conditions as well as the respective luminescence output. The measurements have shown that GdCl<sub>3</sub> as a co-dopant for EuCl<sub>2</sub> retards the nucleation and growth of BaCl<sub>2</sub> nanocrystals the most. Compared to the other RE co-dopants the cause of this is thought to be the larger atomic radius of Gd<sup>3+</sup> of about 233 pm ( $r_{Tb}=225$  pm,  $r_{Yb}=222$  pm and  $r_{Nd}=206$  pm) [74] resulting in a higher electro-negativity and higher probability to attract electrons towards the nucleus. Therefore, more energy is needed to break the bond between the Gd and Cl ions or to split off Cl ions, which can then contribute to the crystallization and growth of more and larger BaCl<sub>2</sub> nanocrystals. However, Nd<sup>3+</sup> does not fit into this trend, since its crystallization peak temperatures are located between the peaks of Gd<sup>3+</sup> and Tb<sup>3+</sup> and not, as one would suppose from the atomic radius, at the lowest temperature of all co-dopants. This effect can be explained by former studies on Nd<sup>3+</sup>-doped FCZ glasses and glass ceramics which have shown that the optical transitions of the Nd ions are affected by the BaCl<sub>2</sub> nanocrystal size leading to the conclusion that some of the Nd<sup>3+</sup> ions, similar to Eu<sup>2+</sup>, are sitting in close proximity to the nanocrystals or possibly incorporated into them [69]. Thus, the interactions between Nd ions and BaCl<sub>2</sub> crystal lattice may lead to the higher BaCl<sub>2</sub> crystallization temperature.

Taking a look onto the XRD measurements and mean particle sizes of all samples one can see similarities between the increasing particle sizes from 250 °C to 260 °C and the increasing integrated PL signal for Yb<sup>3+</sup>, Tb<sup>3+</sup> and Nd<sup>3+</sup>-doped samples in the corresponding annealing temperature regime. In case of Nd<sup>3+</sup>, a slightly higher integrated PL signal is always observed. One reason could be that the larger particles are able to incorporate more Eu<sup>2+</sup> leading to a slightly enhanced luminescence. On the other hand, it is known from transmission measurements that the opacity increases with increasing crystallite size and therefore the reflectance and scattering from the glass surface will increase and possibly lead to such a slightly higher signal at the detector. Increasing opacity and scattering further also results in a reduction of excitation volume and penetration depth of the excitation light, respectively. As a consequence, the increase of the PL signal with higher annealing temperatures will first weaken, saturate and then decrease, as it is probably the case for Nd<sup>3+</sup> from 260 °C to 270 °C.

The PSL evaluation shows, that SE and CE parameters behave similar for the different co-dopants Yb<sup>3+</sup>, Tb<sup>3+</sup> and Nd<sup>3+</sup>. All SEs lie in the range of 10 to 30  $\mu\text{J}/\text{mm}^2$ , which is even lower than the lowest value for the 39% EuCl<sub>2</sub>-doped FCZ glass (45.9  $\mu\text{J}/\text{mm}^2$ ) and already comparable to BFB. However, the CEs still lie below 5  $\text{pJ}/\text{mm}^2/\text{mR}$ , which is again around a factor 5 worse than BFB.

The structural and optical results for the Gd<sup>3+</sup> samples are in good correlation to each other. The retarded nucleation and crystal growth measured with DSC and XRD, probably caused by the larger atomic radius of Gd<sup>3+</sup>, makes higher annealing temperatures necessary to reach the same orthorhombic BaCl<sub>2</sub> nanocrystal sizes, as well as the same total luminescence output and CE of the other investigated co-dopants. A final overview of the results is shown in Fig. 55.

In conclusion, the RE co-dopant additives do not significantly enhance the total Eu PL and PSL output. Therefore, the next chapter will introduce borate glasses as a promising matrix material for a possible improvement of the Eu<sup>2+</sup> luminescence.

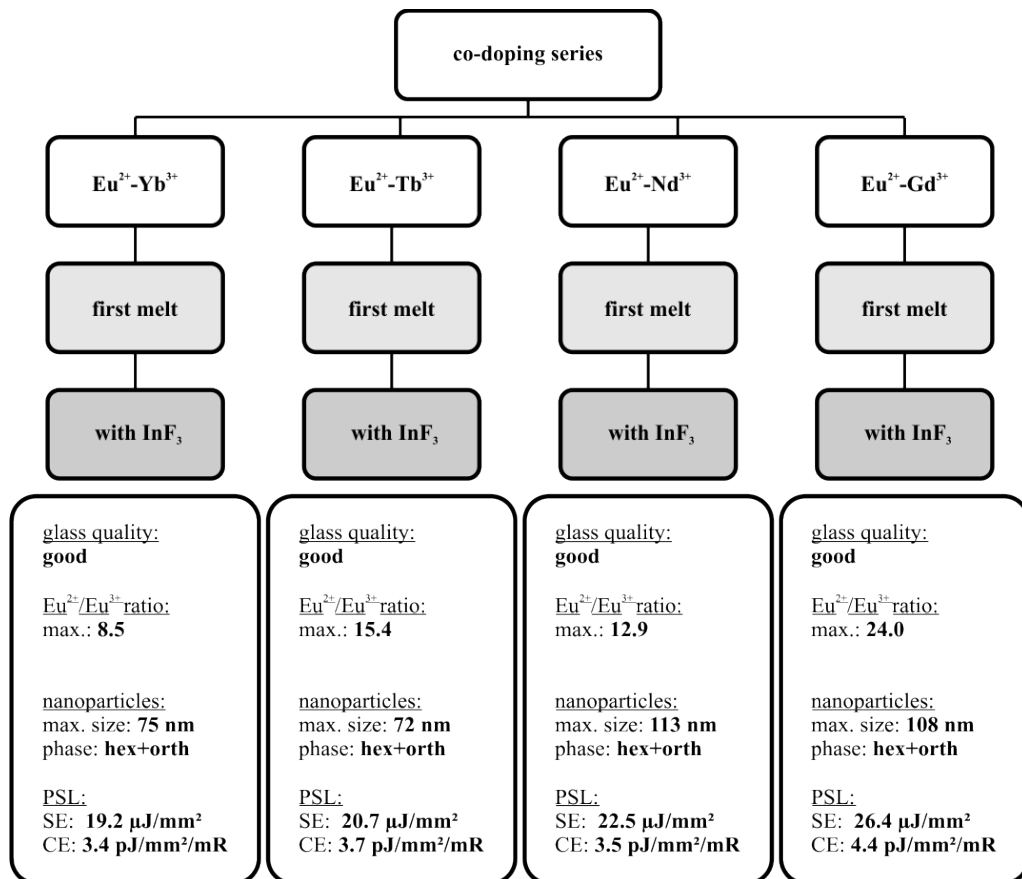


Figure 55: Final overview of the obtained results for the rare-earth co-doping series.

## EU-DOPED BORATE GLASS CERAMICS

Another way to improve the total luminescence output as well as glass homogeneity and reproducibility is the selection of a different glass matrix such as borate glasses. Borate glasses are known as highly optically transparent and inexpensive matrix materials for fluorescent ions. Appleby *et al.* [75, 76] developed similar  $\text{Eu}^{2+}$ -doped glass-ceramics for use as thermal neutron imaging plates for neutron radiography. They reported their excellent thermal neutron imaging properties and PSL-activity, but at the same time the difficulty to grow small semitransparent  $\text{BaCl}_2$  crystallites with high PSL conversion efficiency. Therefore, this chapter deals with the structural and optical characterization of the material and should give some further insights as to whether or not borate glass is applicable as a host for luminescent  $\text{Eu}^{2+}$  ions incorporated into  $\text{BaCl}_2$  nanocrystals.

Figure 56 shows an overview of the  $\text{Eu}^{2+}$ -doped lithiumchloroborate (LCB) glasses investigated consisting of  $53\text{B}_2\text{O}_3\text{-}24\text{Li}_2\text{O}\text{-}5\text{LiF}\text{-}3\text{SiO}_2\text{-}14\text{BaCl}_2\text{-}1\text{EuCl}_2$  (values in mol%). The whitish opaque appearance is due to an instant ceramization of the glass when pouring the melt into the pre-heated brass mold for the quenching step. Three samples were investigated, with the sample process varying in mold temperature: 100 °C (left sample), 200 °C (middle sample) and 300 °C (right sample).

## 6.1 X-RAY ABSORPTION NEAR EDGE STRUCTURE

Figure 57 shows the normalized Eu  $L_{\text{III}}$  XANES spectrum of the as-made  $\text{Eu}^{2+}$ -doped LCB glass poured into a 100 °C hot brass mold and cooled to 25 °C room temperature over 4 hours. Similar to the Eu-doped FCZ glasses, the two characteristic WL energies of  $\text{Eu}^{2+}$  and  $\text{Eu}^{3+}$  are located at about 6,976 eV and 6,984 eV and are associated with the dipole-allowed transition from a  $2^2\text{P}_{3/2}$  core

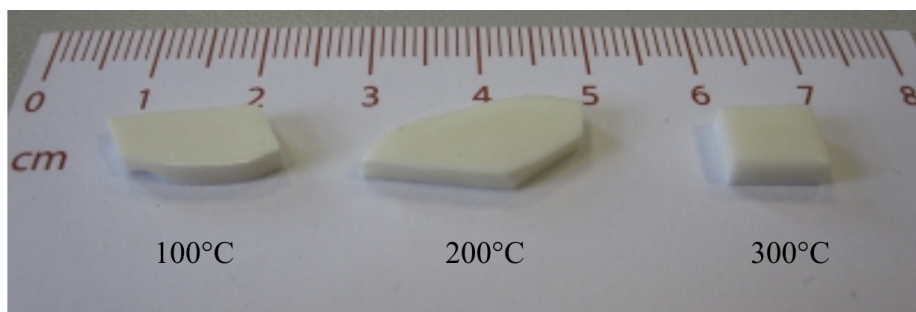


Figure 56: Overview of  $\text{Eu}^{2+}$ -doped chloroborate glasses poured into a 100 °C, 200 °C and 300 °C hot brass mold and cooled to 25 °C room temperature over 4 hours.

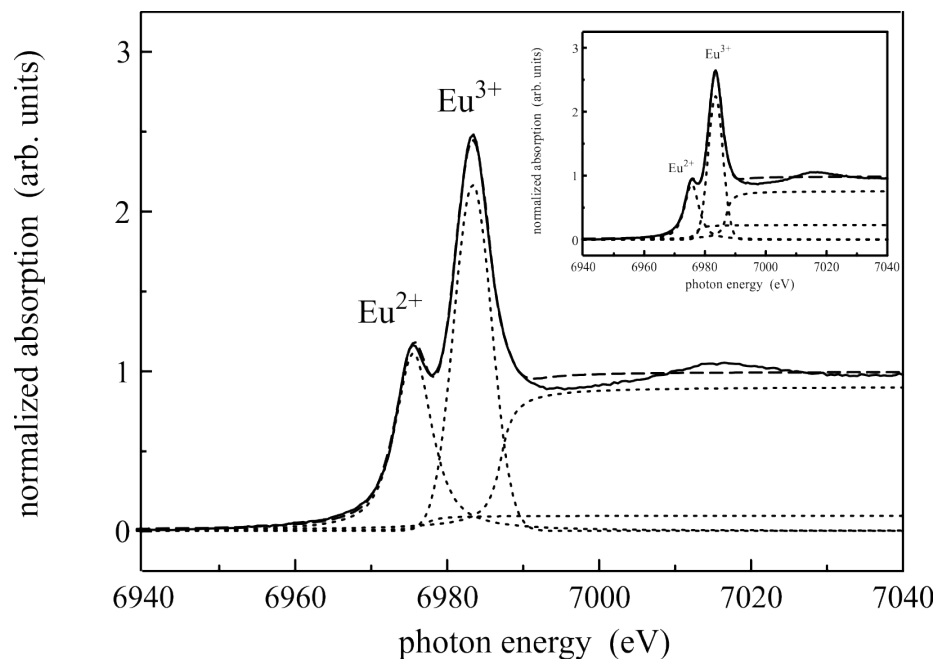


Figure 57: Normalized XANES spectrum of the as-made  $\text{Eu}^{2+}$ -doped LCB glass poured into a  $100\text{ }^\circ\text{C}$  hot brass mold. A pseudo-Voigt function and an arctangent function (dashed curves) were used to fit each of the characteristic white lines of  $\text{Eu}^{2+}$  and  $\text{Eu}^{3+}$  and their absorption edges, respectively. The inset shows the normalized XANES spectrum of the as-made  $\text{Eu}^{2+}$ -doped LCB glass poured into a  $300\text{ }^\circ\text{C}$  hot brass mold for comparison.

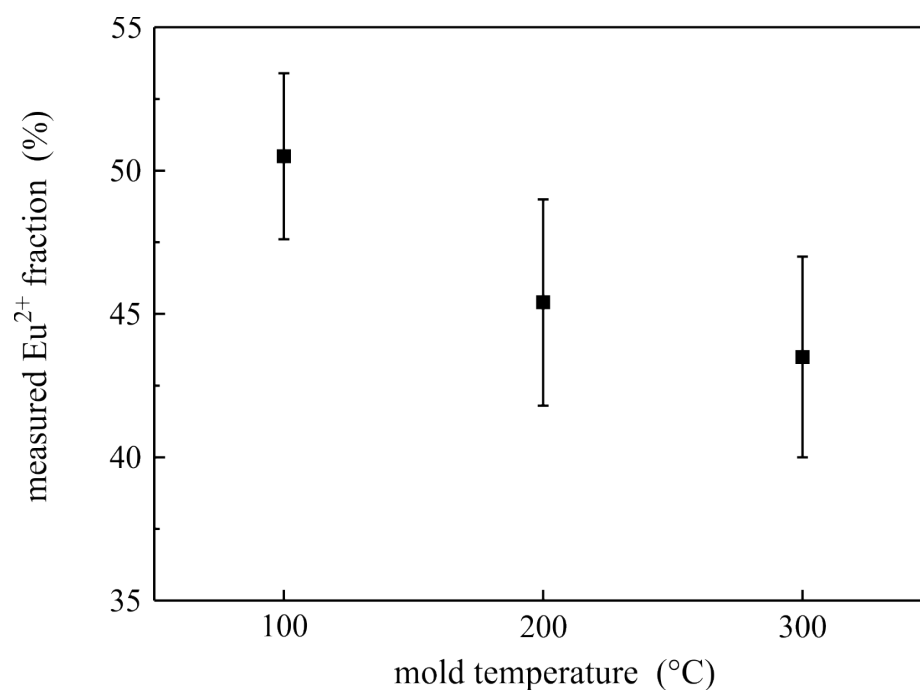


Figure 58: Measured  $\text{Eu}^{2+}$  fraction of the  $\text{Eu}^{2+}$ -doped LCB glass vs mold temperature.

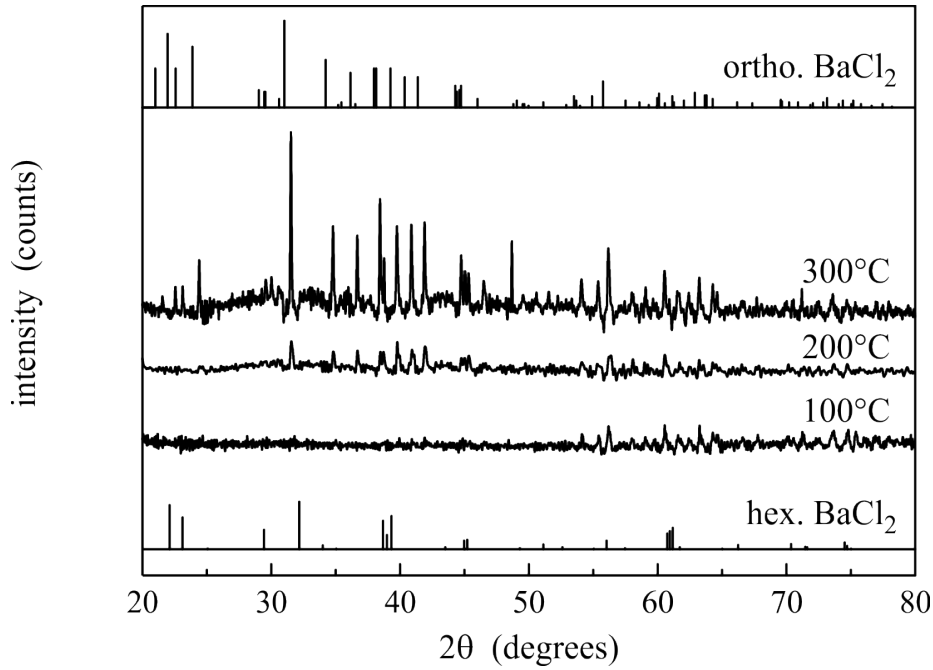


Figure 59: XRD patterns of  $\text{Eu}^{2+}$ -doped LCB glass poured into a 100 °C, 200 °C and 300 °C hot brass mold. The XRD patterns of hexagonal (bottom, PDF 00-45-1313) and orthorhombic  $\text{BaCl}_2$  (top, PDF 00-24-0094) are shown for comparison.

level into an empty 5d state [54]. The determination of the  $\text{Eu}^{2+}$ -to- $\text{Eu}^{3+}$  ratios is done as described in Chapter 3.

Figure 58 shows the measured  $\text{Eu}^{2+}$  fractions of the  $\text{Eu}^{2+}$ -doped LCB glasses for three different mold temperatures. Taking the measurement error into account, the fractions of all samples remain nearly constant:  $(51 \pm 3)\%$  for the sample which was poured into the 100 °C pre-heated mold,  $(45 \pm 4)\%$  for 200 °C and  $(44 \pm 4)\%$  for 300 °C mold temperature. However, a trend to lower temperatures is becoming evident.

## 6.2 X-RAY DIFFRACTION

Figure 59 shows the XRD patterns of the  $\text{Eu}^{2+}$ -doped LCB glasses poured into the 100 °C, 200 °C and 300 °C hot brass mold. The patterns for 200 °C and 300 °C show crystalline reflections which can be attributed to orthorhombic  $\text{BaCl}_2$  nanocrystals (top bar pattern of PDF 00-24-0094), so that during casting of the glass melt  $\text{BaCl}_2$  instantly crystallizes in its orthorhombic crystal structure. This occurs even for mold temperatures lying below the typical crystallization annealing temperatures of hexagonal  $\text{BaCl}_2$  in FCZ glasses (see Section 4.2). However, the sample which was poured into the 200 °C mold shows significantly less intense reflections than the sample which was cast into the 300 °C hot mold suggesting that only a partial crystallization took place in case of the lower temperature. For the 100 °C mold temperature the  $\text{BaCl}_2$  reflections are not intense enough for an analysis. The longer cool down time and the higher tem-

perature and energy, respectively, in conjunction with longer diffusion lengths for free ions in the glass matrix leads to the crystallization of a larger BaCl<sub>2</sub> amount and thus to higher XRD reflection intensities.

The *DIFFRACplus EVA v1.2* XRD software estimated the mean diameter of the orthorhombic particles for the (211) reflection to 45 nm for the sample which was poured into the 200 °C mold. In case of the 300 °C mold, a size increase to 85 nm was calculated.

### 6.3 PHOTOLUMINESCENCE

As mentioned in the chapters before, the luminescence of the Eu<sup>2+</sup> ions adjacent to or incorporated into the BaCl<sub>2</sub> is extremely sensitive to the BaCl<sub>2</sub> nanocrystal phase and size. Therefore, it is possible to observe also very small amounts of crystallized material with the PL technique. Figure 60 shows a PL excitation-emission map of the 1 mol% Eu<sup>2+</sup>-doped LCB glass which was poured into the 100 °C hot mold. Whereas in the XRD measurements only weak crystalline BaCl<sub>2</sub> reflections were observed for this temperature, the PL map clearly shows a broad emission band belonging to the 5d-4f transition of Eu<sup>2+</sup> ions incorporated into orthorhombic BaCl<sub>2</sub>. This is also a hint for a strong crystal field coupling of the 4f<sup>6</sup>5d orbital suspending states below the <sup>6</sup>P<sub>7/2</sub> level of the 4f<sup>7</sup> configuration, also seen in the case of FCZ glasses before.

The radiative transitions occur for UV excitation wavelengths above 269 nm and show maximum intensities for 307 nm and 357 nm excitation. The corresponding emission wavelengths are 408 nm and 430 nm, respectively. While the 357 nm excitation maximum can be attributed to the <sup>6</sup>P<sub>7/2</sub> level, the first level above the <sup>8</sup>S<sub>7/2</sub> ground state of the 4f<sup>7</sup> configuration, the other excitation maximum (307 nm; 4.04 eV) lies energetically in between the <sup>6</sup>D (lowest level at 4.21 eV above the ground state) and the <sup>6</sup>I (lowest level at 3.83 eV above the ground state) states, which are causing the left edges of the two stronger luminescence intensity spots in Fig. 60 (yellow and red areas).

Note that the relatively sharp luminescence cut-off at 380 nm emission wavelength is caused by the usage of a KV 370 filter between the sample and the emission monochromator to prevent an interfering second order signal from the excitation light. The corresponding spectral internal transmittance curve of the KV 370 can be found in the Appendix C.1.

Figure 61 shows a similar PL map for higher excitation and corresponding emission wavelengths. The presence of Eu<sup>3+</sup> ions is confirmed by the observed emission bands for 393 nm (<sup>7</sup>F<sub>0</sub> → <sup>5</sup>L<sub>6</sub> transition) and 464 nm (<sup>7</sup>F<sub>0</sub> → <sup>5</sup>D<sub>2</sub> transition) excitation light. Higher intensities are obtained when exciting at 464 nm. The small number of absorption bands is a reason of the selection rules for electrical dipole transitions in the RE ions. Electron transitions from the ground state <sup>7</sup>F<sub>J</sub> to <sup>5</sup>D<sub>J'</sub> with J = 0 to J' = 0 are not allowed and hence <sup>7</sup>F<sub>0</sub> → <sup>5</sup>D<sub>0</sub> transitions are not observed in the PL map. Furthermore, <sup>7</sup>F<sub>0</sub> → <sup>5</sup>D<sub>1</sub> and <sup>7</sup>F<sub>0</sub> → <sup>5</sup>D<sub>3</sub> transitions do not occur, because transitions from J = 0 to uneven J' are improbable [67].

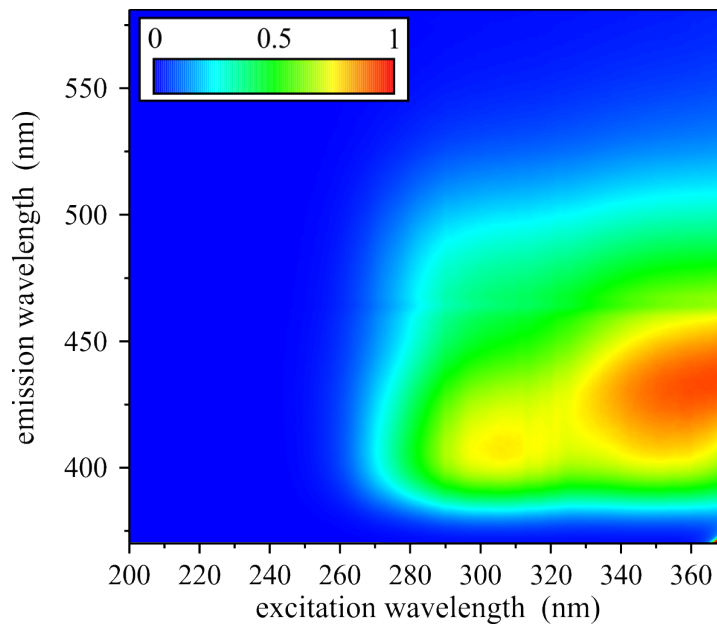


Figure 60: PL excitation-emission map of a 1 mol%  $\text{Eu}^{2+}$ -doped LCB glass poured into a 100 °C hot brass mold. A KV 370 filter was used between the sample and the emission monochromator.

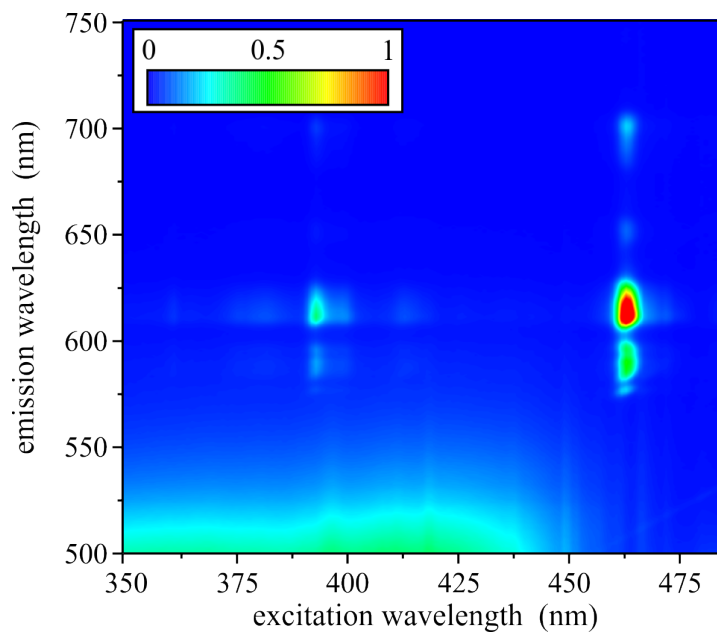


Figure 61: PL excitation-emission map of a 1 mol%  $\text{Eu}^{2+}$ -doped LCB glass poured into a 100 °C hot brass mold. A KV 370 filter was used between the sample and the emission monochromator.

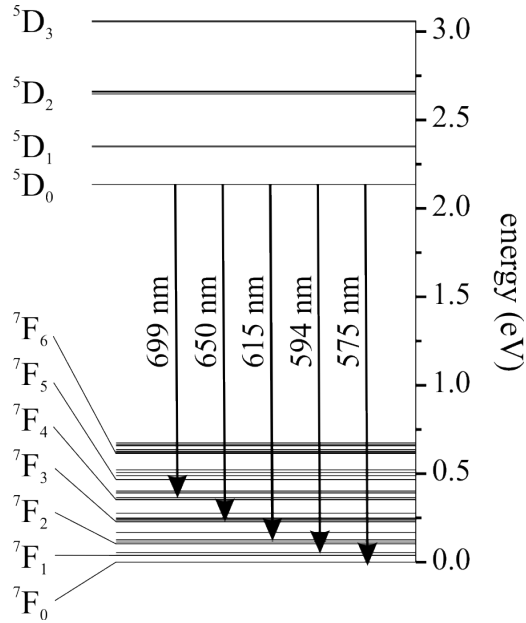


Figure 62: Measured emission lines corresponding to the electron transitions of  $\text{Eu}^{3+}$  of the 1 mol%  $\text{Eu}^{2+}$ -doped LCB glass. The ground state is  ${}^7\text{F}_0$ . The energy level diagram corresponds to data of Ref. [25, 26].

Figure 62 summarizes the  $\text{Eu}^{3+}$  emissions observed at 699, 650, 615, 594 and 575 nm, which can be attributed to the radiative  ${}^5\text{D}_0 \rightarrow {}^7\text{F}_J$  ( $J=4, 3, 2, 1, 0$ ) transitions [26, 67].

In order to investigate the influence of the mold temperature on the luminescence behavior, a PL map for the 1 mol%  $\text{Eu}^{2+}$ -doped LCB glass poured into the higher temperature mold at 200 °C is shown in Fig. 63. Again, the typical broad  $\text{Eu}^{2+}$  5d-4f emission band is observed, but with much higher intensities than the sample which was poured into the lower tempered mold at 100 °C leading to the conclusion that more  $\text{Eu}^{2+}$  ions are incorporated into or sitting near a higher number of larger nanocrystals. Due to the stronger signals a small intensity decrease is visible at an emission wavelength of 464 nm, which is not dependent on the excitation wavelength. Thus, this band is attributed to the  $\text{Eu}^{3+}$  absorption belonging to the  ${}^7\text{F}_0 \rightarrow {}^5\text{D}_2$  transition already discussed above.

Similar observations are made for the  $\text{Eu}^{3+}$  luminescence bands shown in Fig. 64. The peak positions are not influenced by the higher temperature mold, but again the intensities of all bands increase.

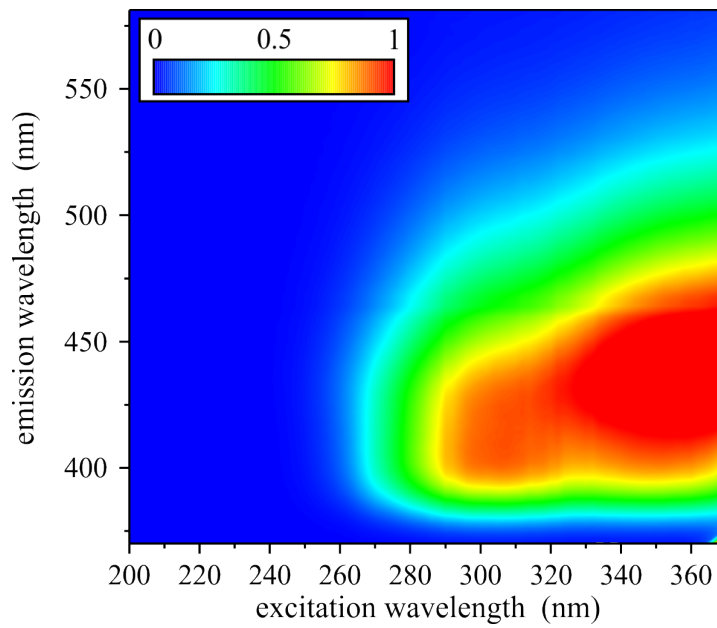


Figure 63: PL excitation-emission map of a 1 mol%  $\text{Eu}^{2+}$ -doped LCB glass poured into a 200 °C hot brass mold. A KV 370 filter was used between the sample and the emission monochromator.

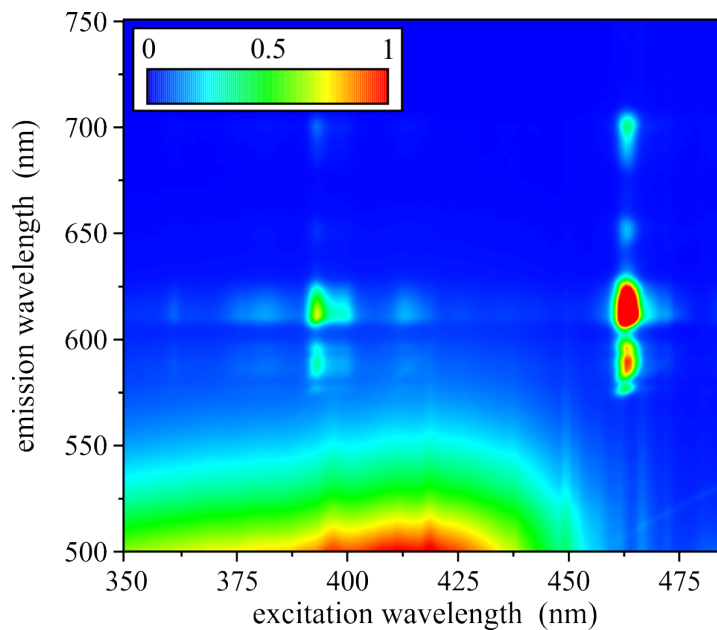


Figure 64: PL excitation-emission map of a 1 mol%  $\text{Eu}^{2+}$ -doped LCB glass poured into a 200 °C hot brass mold. A KV 370 filter was used between the sample and the emission monochromator.

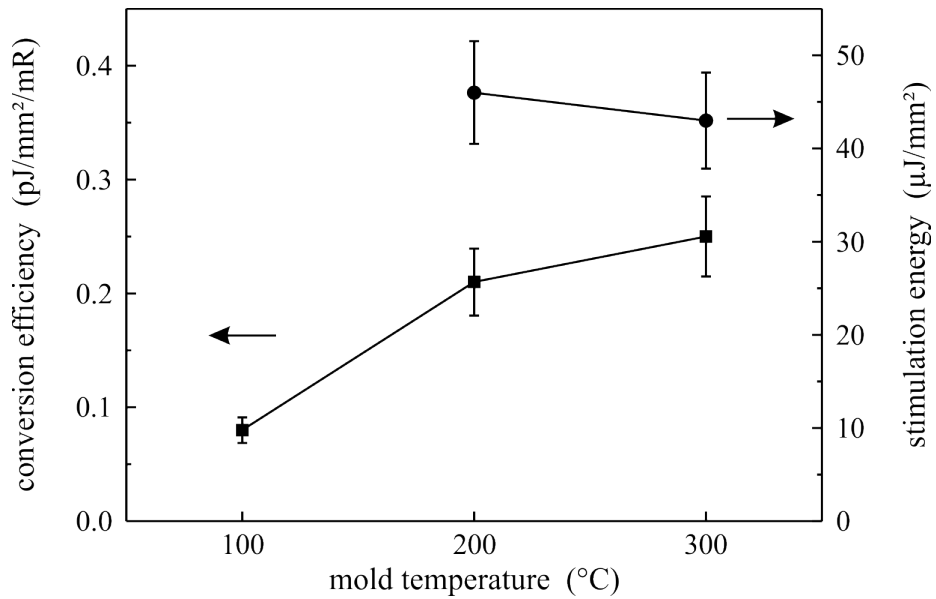


Figure 65: Conversion efficiencies (squares) and stimulation energies (circles) of  $\text{Eu}^{2+}$ -doped chloroborate glasses poured into differently heated brass molds.

#### 6.4 PHOTOSTIMULATED LUMINESCENCE

PSL measurements were performed to evaluate the storage phosphor properties of the  $\text{Eu}^{2+}$ -doped LCB glass ceramics. Figure 65 shows the CEs (squares) and the corresponding SEs (circles) for different mold temperatures. Only weak PSL signals are obtained for all samples. In case of the sample which was poured into the 100 °C tempered mold the signal is not high enough to calculate the SE. The CE increases with increasing temperature from 0.08  $\text{pJ}/\text{mm}^2/\text{mR}$  at 100 °C to 0.25  $\text{pJ}/\text{mm}^2/\text{mR}$  at 300 °C, while the SE remains nearly constant at 46  $\mu\text{J}/\text{mm}^2$  at 200 °C and 43  $\mu\text{J}/\text{mm}^2$  at 300 °C within the experimental error.

#### 6.5 DISCUSSION

Comparing the XANES results of the investigated pure  $\text{Eu}^{2+}$ -doped LCB glasses with the results from the pure  $\text{Eu}^{2+}$ -doped FCZ based glasses discussed before, LCB glasses show significantly lower  $\text{Eu}^{2+}$  fractions (43% for the 300 °C mold sample to 51% for the 100 °C mold sample) lying in the range between 10% to 20% nominal  $\text{Eu}^{2+}$  fraction for FCZ based glasses. The reason for this is the highly oxygen providing LCB glass host, which oxidizes a large amount of the  $\text{Eu}^{2+}$  into  $\text{Eu}^{3+}$  during glass melting and also while cooling down the glasses in the pre-heated molds. Furthermore, some constituent chemicals of the LCB glass like fluorine act as nucleation grains, which can cause ceramization of the glass without any additional annealing step. This leads to optical scattering from the crystallites and limits the spatial resolution when the glass is used as an storage phosphor image plate.

Regardless of the mold temperatures, XRD measurements revealed only orthorhombic  $\text{BaCl}_2$  nanoparticles inside the glass matrix; the hexagonal phase

did not emerge. In Ref. [47] it has been reported that oxygen might be a trigger for the phase transformation from hexagonal to orthorhombic phase  $\text{BaCl}_2$  in FCZ based glass ceramics. This seems to be the case for LCB based glasses with high oxygen amounts. A higher mold temperature resulted in a higher number of larger  $\text{BaCl}_2$  nanocrystals; the maximum mean diameter of 85 nm occurred in the sample which was poured into the 300 °C tempered mold. Therefore, one would suggest from the prior investigated Eu-doped FCZ glass series that the  $\text{Eu}^{2+}$  PL signal increases with increasing nanoparticle sizes and volume fraction. However, this effect is counteracted by the decrease of the  $\text{Eu}^{2+}$  fraction with increasing mold temperature in favor of an increasing  $\text{Eu}^{3+}$  fraction measured by XANES. The higher  $\text{Eu}^{3+}$  PL signals confirm these measurements.

Compared to the  $\text{Eu}^{2+}$ -doped FCZ based glasses, the investigated LCB based glasses provide significantly lower PSL signals and thus are far away from the values of  $\text{BaFBr:Eu}^{2+}$ . Nevertheless, the CE increases with increasing mold temperature from 0.08  $\text{pJ}/\text{mm}^2/\text{mR}$  at 100 °C to 0.25  $\text{pJ}/\text{mm}^2/\text{mR}$  at 300 °C, because of an increasing volume fraction of orthorhombic  $\text{BaCl}_2$  and  $\text{Eu}^{3+}$ . This result supports the explanation in Chapter 4: a higher  $\text{Eu}^{3+}$  fraction causes more defects to be present in the glass matrix, leading to an increase in CE, probably applies in this case.

In conclusion, the developed  $\text{Eu}^{2+}$ -doped LCB based glasses show an interesting crystallization behavior, which demonstrates again the difficulty of handling and understanding the complex equilibria of glass melts. That being the case, the current glass composition and preparation needs further detailed investigations and improvements to increase the transparency and PSL conversion efficiency.



## RADIATION DETECTION FIBERS

---

Glass has the big advantage of being easily formable when it is a molten mass, i.e., a fiber can be pulled from the melt. In addition, Eu- and BaCl<sub>2</sub>-doped FZ can be heat treated in desired glass regions afterwards in order to make them luminescent upon irradiation with UV light or ionizing radiation. A possible new application on this basis could be the precise detection of an x-ray dose inside specific human body regions, which only a glass fiber with a luminescent tip can reach. The rest of the fiber would be used as an optical conductor which would guide the generated scintillation light out of the body into a photomultiplier characterizing the incident x-rays and giving a dose dependent luminescence signal, respectively. During this work, several fiber production methods were investigated in collaboration with PHILIPP GOLDSCHMIDT, who has written his Bachelors thesis on this topic [77]. This chapter will only focus on two techniques, which involved two different materials in the pulling process: Eu-doped FCZ based glass and SiO<sub>2</sub> glass. The obtained fibers as well as the fiber characterization in terms of quality and fluorescence properties are presented in the following sections. For further information see [77].

### 7.1 FIBER PULLING VIA PIPETTE

One fiber production method was the pulling from a cylindric preform, which was previously produced by the so called built-in technique, where two materials with different refractive indices are merged. A common commercially available quartz glass (SiO<sub>2</sub>) pipette was used as cladding layer, while the Eu-doped FCZ based glass acted as core. The main reason behind this idea was, that SiO<sub>2</sub> compared to ZBLAN is not harmful for the human body ensuring a safe application of such fibers in medical applications. Figure 66 shows the schematic setup for the preform production. The built-in process was realized with a syringe which was connected to the SiO<sub>2</sub> pipette via a rubber hose. A hose clamp between syringe and pipette was used to control the vacuum when raising the plunger of the syringe. The glass pipette was directly placed into the hot glass melt so that, upon opening the valve, the negative pressure drew the melt up into the pipette. Therefore, the glassy carbon crucible was taken out of the furnace and the melt temperature was reduced from 745 °C to 580 °C in order to take into account the slow cooling of the melt inside the pipette. Higher temperatures resulted in a faster nucleation and partial crystallization of the glass matrix and the BaCl<sub>2</sub> nanocrystals.

Figure 67 (top) shows the Eu-doped FCZ based glass filled SiO<sub>2</sub> pipette under UV multi-band excitation with 254/366 nm. The different fluorescence regions inside the glass are caused by temperature differences during the cooling process leading to different BaCl<sub>2</sub> crystallization phases and nanoparticle sizes. The

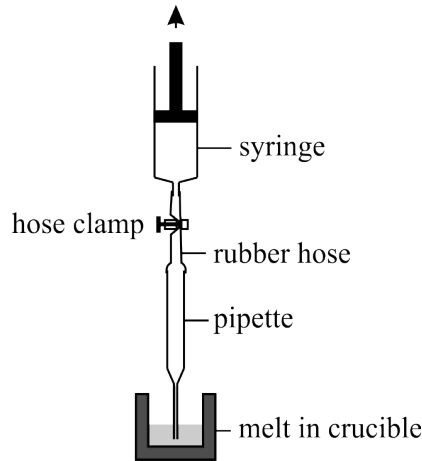


Figure 66: Schematic setup for a preform production.

blue-violet emission of the pipettes bottom region is attributed to orthorhombic nanoparticles in the glass. During the pulling process, this part of the pipette was inside the hot glassy carbon crucible and therefore was exposed to the highest temperatures for the longest time – long enough to form the orthorhombic crystal phase. Going into the higher regions of the pipette, a light-blue emission is observed which is attributed to hexagonal nanoparticles. Going even higher into the non-luminescent glass region, the cooling is fast enough to prevent nucleation and crystallization. Just this glassy part was processed to a preform afterwards, which then was pulled into an 8 cm long and approximately  $250\ \mu\text{m}$  thick fiber by using a Bunsen burner to heat up and melt the preform (see Fig. 67, middle). A technological problem was the difference in melting points of  $\text{SiO}_2$  (around  $900\ ^\circ\text{C}$ ) and the ZBLAN core (around  $260\ ^\circ\text{C}$ ). While the FCZ based glass core was already boiling, the outer cladding layer was still solid. Thus, the fiber showed air bubbles, some inclusions and a full crystallization of the FCZ based glass. However, the functionality could be shown by observing the down-conversion mechanism under UV multi-band excitation with  $254/366\ \text{nm}$  (see Fig. 67, bottom).

## 7.2 FIBER PULLING VIA CAPILLARY

In a second step and as an attempt to overcome homogeneity problems due to the different melting points of core and cladding layer material, the total fiber diameter was kept constant. Therefore,  $200\ \mu\text{m}$  thin  $\text{SiO}_2$  capillaries with a cavity diameter of  $150\ \mu\text{m}$  were used, into which the hot glass melt was drawn up via a syringe and a needle, which was hermetically glued onto the capillaries. The negative pressure was sufficient to draw the Eu-doped FCZ based glass melt into the cavity, where it hardened after a few seconds. Figure 68 shows an optical microscope image of a filled capillary. Glass regions with many bubbles inside and also regions free of glass are visible. A possible explanation could be that a part of the gases which are formed during the cooking is additionally sucked into the capillary. However, the cooling inside the capillary was fast enough to prevent crystallization of the  $\text{BaCl}_2$ . In order to check

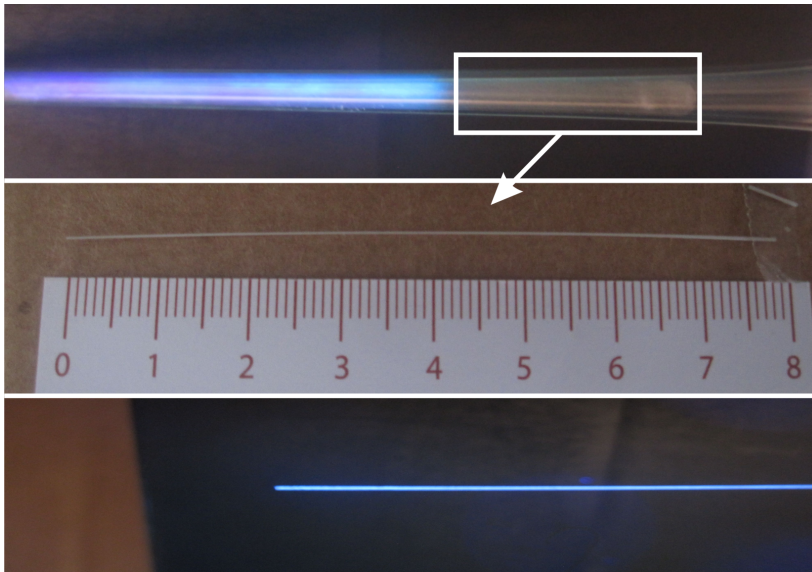


Figure 67: Side view of an Eu-doped FCZ based glass filled  $\text{SiO}_2$  pipette under UV multi-band excitation with 254/366 nm (top). The non-crystalline region was drawn together with the  $\text{SiO}_2$  cladding layer into a fiber afterwards which is shown without UV excitation (middle) and under UV multi-band excitation (bottom) [77].

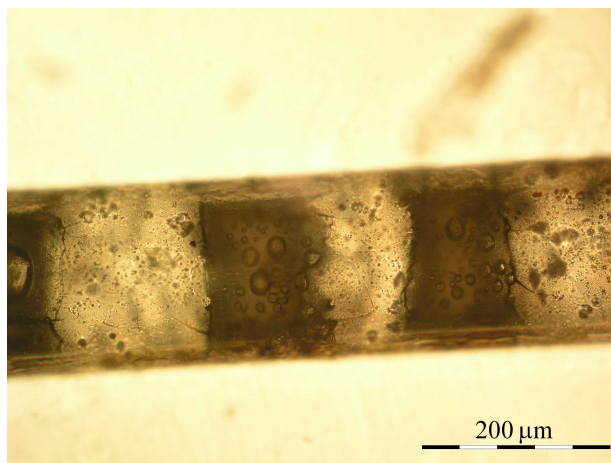


Figure 68: Side view of an Eu-doped FCZ based glass filled  $\text{SiO}_2$  capillary under an optical microscope. Air bubbles, glass (dark) and air (bright) regions are visible [77].

the optical application functionality and to initiate the  $\text{BaCl}_2$  crystallization, the fiber was heat treated in an argon atmosphere for 20 minutes at  $290^\circ\text{C}$ . Note that the fiber was exposed to air for several hours before the heat treatment.

Untreated and heat treated Eu-doped FCZ based glass filled  $\text{SiO}_2$  fibers were investigated under a scanning electron microscope (SEM) to evaluate their quality. Figure 69 shows the corresponding recorded SEM images of the untreated (left) and heat treated (right) capillaries. Regions where the  $\text{SiO}_2$  surfaces are just covered by a  $1 - 5\ \mu\text{m}$  thin FCZ based glass layer are shown in Fig. 69a and Fig. 69b. They can be explained by the inter-molecular attractive forces between the melt and the solid  $\text{SiO}_2$  surrounding surfaces. Adhesion forces are larger than the cohesion forces of the melt, so that in total, the resulted force is orientated into the wall surface and pulls the melt up. A closer look onto the surfaces is taken in Fig. 69c and Fig. 69d. While the FCZ based glass layer of the untreated capillary shows a smooth and homogeneous surface, the glass surface of the heat-treated fiber is rough and uneven. In Chapter 4 it was shown, that exposure to air followed by an annealing step in argon leads to a small partial and diffusion-limited oxidation of  $\text{Eu}^{2+}$  on and near the oxygen-contaminated glass surfaces. In literature [14] it has been reported, that oxidation and the corresponding chemical reactions on the surface can form small quantities of acidic reaction products like HF and HCl, which are able to degrade the glass surface. This could lead to the observed roughness. Beside the above mentioned structures, completely filled cavities are also observed as shown in Fig. 69e and Fig. 69f; they nevertheless are rare.

### 7.3 PHOTOLUMINESCENCE

Figure 70 (left) shows PL emission spectra of the 20 minutes at  $290^\circ\text{C}$  heat treated (solid curve) and the untreated capillaries (dashed curve). The annealed capillary clearly shows the known broad emission bands of  $\text{Eu}^{2+}$  ions adjacent to or incorporated into hexagonal  $\text{BaCl}_2$  nanocrystals when excited with 280 nm UV light. The peak at 406 nm is attributed to the 5d-4f transition of  $\text{Eu}^{2+}$  in hexagonal  $\text{BaCl}_2$ , while the broader 486 nm emission is again interpreted to be based on an impurity associated  $\text{Eu}^{2+}$  site with a perturbed crystal field [58, 59]. The untreated capillary shows no luminescence signal. Excitation of trivalent Eu with 393 nm, however, leads to the typical  $\text{Eu}^{3+}$  emission bands (see Fig. 70 (right)) in both the untreated and heat treated capillaries. The intensity maxima of the 614 nm emission bands are attributed to the radiative  ${}^5\text{D}_0 \rightarrow {}^7\text{F}_2$   $\text{Eu}^{3+}$  transition and are almost equal for both cases. Since the  $\text{Eu}^{2+}$  emission intensity of the heat treated capillary is almost zero in this spectral region, one can say that the  $\text{Eu}^{3+}$  was not affected by the additional heat treatment and  $\text{BaCl}_2$  crystallization.

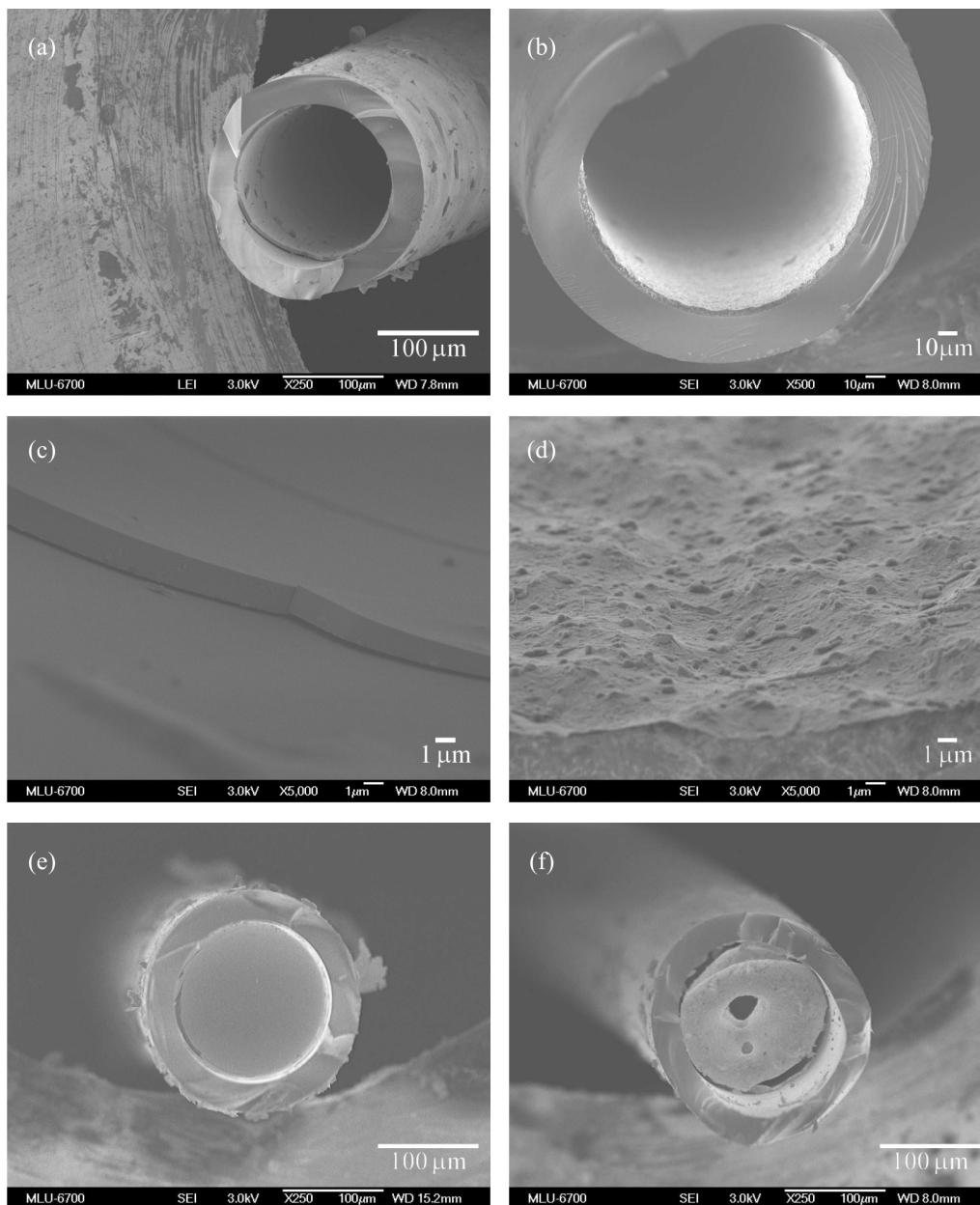


Figure 69: Scanning electron microscope images of untreated (left) and heat treated (right) Eu-doped FCZ based glass filled  $\text{SiO}_2$  capillaries [77]. Cavity regions where the  $\text{SiO}_2$  surfaces are just covered by a 1 – 5  $\mu\text{m}$  thin FCZ based glass layer are shown in (a) and (b). The difference in surface roughness between untreated and heat treated capillary is shown in (c) and (d), while (e) and (f) show completely filled cavities.

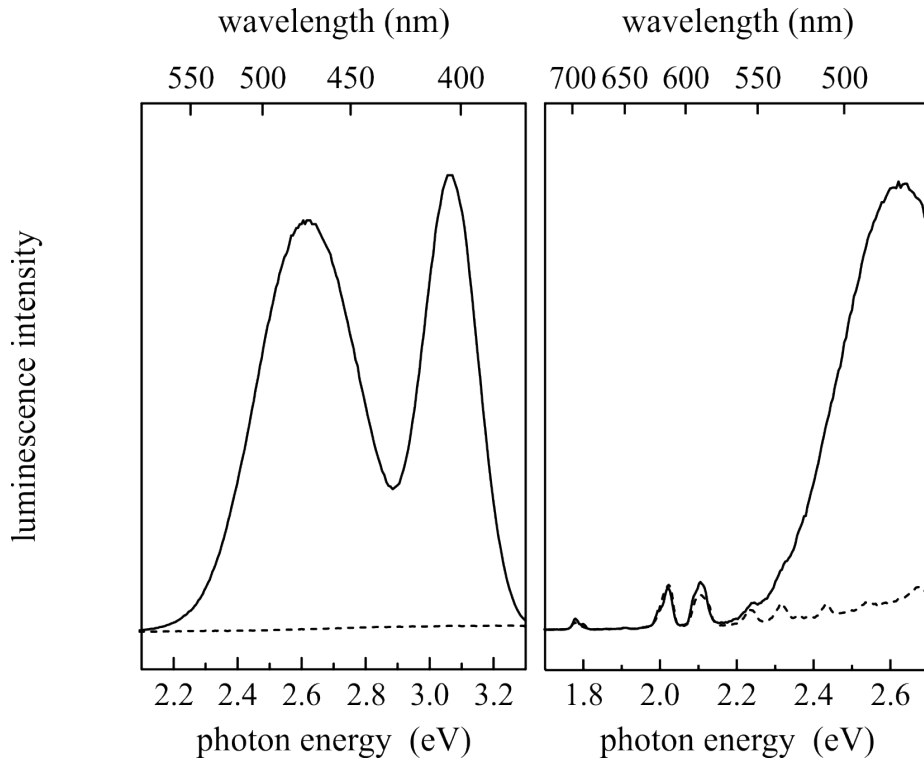


Figure 70: PL spectra for a Eu-doped FCZ based glass filled  $\text{SiO}_2$  fiber annealed at  $290^\circ\text{C}$  for 20 min (solid curve) and untreated (dashed curve). The PL was excited at 280 nm (left) and 393 nm (right) [77].

#### 7.4 DISCUSSION

The fiber pulling method via pipette turned out to be problematic for two reasons. Firstly, only a small amount of non-crystalline glass, which was sitting at the top of the capillary, could be used for further processing; a lot of material crystallized during the pulling process and hence was wasted. Secondly, the different melting temperatures of the FCZ based and  $\text{SiO}_2$  glass led to structural defects like air bubbles, during the necessary additional pulling step into a thinner fiber. The usage of a  $200\ \mu\text{m}$  thin solid  $\text{SiO}_2$  capillary was easier to produce, but has shown that the capillary effect has an impact on the filling ability of the fiber cavity. For proper applicability, the cavity needs to be completely filled in order to increase the light guiding properties by total internal reflection. Rough surfaces, as observed for the heat treated of a non-completely filled fiber, would lead to scattering and signal losses.

After having finally realized an optimized fiber pulling process, which would produce completely filled fibers of a specific length, each fiber would need an x-ray dose dependent PSL calibration in order to take spectral signal losses due to minor structural defects in the fiber, the fiber length and the peripheral detection devices (monochromator and photomultiplier) into account. The front tip surface would need a thin  $\text{SiO}_2$  glass layer to protect the Eu-doped FCZ based glass from the outer surroundings. This front layer could additionally be optimized with a reflective coating like silver to reflect some of the generated scintillation light back into the fiber.

The presented fiber pulling methods have shown the possibility of developing a scintillating Eu-doped FCZ based glass filled SiO<sub>2</sub> fiber. This new idea and the first results look promising for medical applications. The capillary fiber has already shown its scintillation potential under UV excitation, where the typical PL emission bands for Eu<sup>2+</sup> adjacent to or incorporated into hexagonal BaCl<sub>2</sub> were observed.



## SUMMARY

Various series of luminescent europium (Eu)-doped fluorozirconate (FZ) based glass ceramics containing barium chloride ( $\text{BaCl}_2$ ) nanocrystals have been produced in order to improve the complex FCZ glass system and in particular the  $\text{Eu}^{2+}$  luminescence behavior for imaging applications. The addition of  $\text{InF}_3$  to the glass proved to be essential to glass quality, because it maintained the zirconium in its 4+ state and hence reduced the black precipitates. X-ray diffraction (XRD) and photoluminescence (PL) measurements have shown that indium is needed for the transformation from hexagonal to orthorhombic phase  $\text{BaCl}_2$  nanoparticles upon post thermal heat treatment and hence for storage phosphor applications. A subsequent remelting step of the glass has proved to have a negative influence on the storage phosphor properties, while the  $\text{Eu}^{2+}$  content, measured via x-ray absorption near edge structure (XANES), was increased, improving the performance for scintillator applications.

The valency of Eu has a marked effect on the properties of the glasses and glass ceramics. XANES measurements have also revealed that during the glass-melting process,  $\text{Eu}^{3+}$  is partially reduced to  $\text{Eu}^{2+}$ . The detailed investigation of multivalent Eu-doped FCZ based glasses has shown a saturation of the  $\text{Eu}^{2+}$  fraction with higher  $\text{Eu}^{2+}$ -to- $\text{Eu}^{3+}$  doping ratio. The small difference of 13% between 60% and 100% nominal and measured  $\text{Eu}^{2+}$  fraction makes the usage of the cheaper  $\text{EuCl}_3$  attractive in order to reduce costs without lowering the  $\text{Eu}^{2+}$  luminescence significantly. In addition, it was shown that europium chloride converts more  $\text{Eu}^{3+}$  into the divalent valence state than its fluoride counterparts. Slight oxidation of  $\text{Eu}^{2+}$  during annealing was observed when the samples had been previously exposed to air. XRD, PL and photostimulated luminescence (PSL) measurements have shown that a higher amount of  $\text{Eu}^{2+}$  inside the glass results in a phase transition from hexagonal to orthorhombic  $\text{BaCl}_2$  at lower temperatures. Unfortunately, the PSL parameters, stimulation energy (SE) and conversion efficiency (CE), of the best working sample are still a factor 3.4 higher and a factor 4.6 worse than the values for the most commercially used x-ray storage phosphor,  $\text{BaFBr:Eu}^{2+}$ . It has been shown that the CE decreases with increasing  $\text{Eu}^{2+}$  and decreasing  $\text{Eu}^{3+}$  fraction leading to the assumption that  $\text{Eu}^{3+}$  is needed to act as a defect, which might be a source for the photostimulatable electron- and hole traps in the glass matrix or that too much  $\text{Eu}^{2+}$  leads to an energy self-quenching effect.

Co-doping of the  $\text{Eu}^{2+}$ -doped FCZ based glasses with trivalent Tb, Yb, Nd and Gd has proved to have no significant enhancement of the total Eu PL and PSL output when the  $\text{Eu}^{2+}$  is excited. However,  $\text{GdCl}_3$  substantially retarded the nucleation and growth of  $\text{BaCl}_2$  nanocrystals, which was attributed to the larger atomic radius of  $\text{Gd}^{3+}$  resulting in a higher electro-negativity and higher probability to attract electrons towards the nucleus. It makes higher annealing

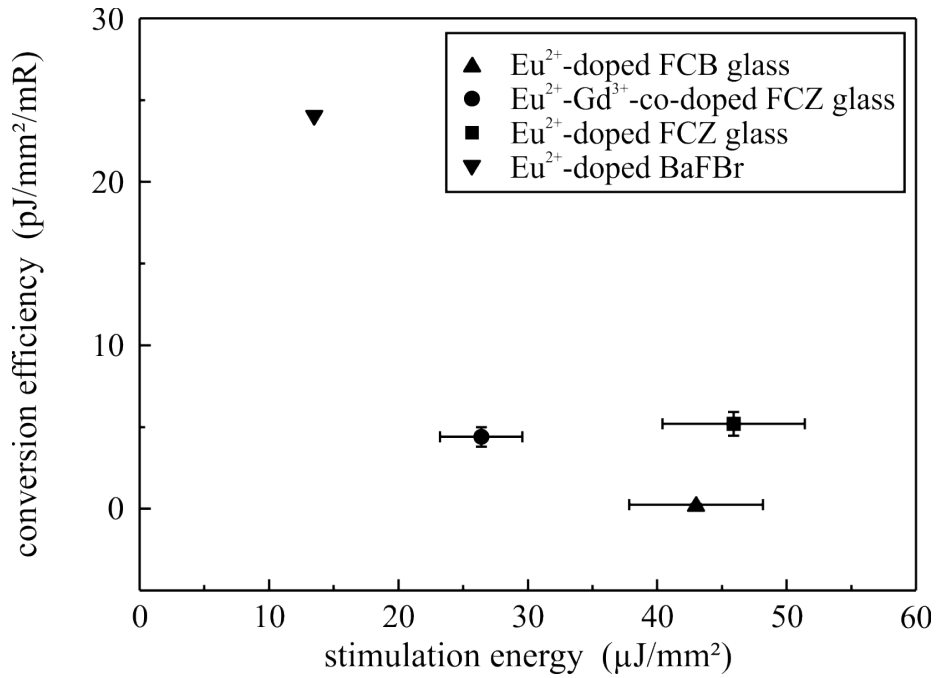


Figure 71: Overview of the PSL results of the best working samples in comparison to BaFBr:Eu<sup>2+</sup>.

temperatures necessary to produce the same orthorhombic BaCl<sub>2</sub> nanocrystal sizes as well as the same total luminescence output and CE of the other three investigated co-dopants, which all behave similarly: All SEs were in the range of 10 to 30  $\mu\text{J}/\text{mm}^2$ , which is comparable to BFB. However, the CEs were still below 5  $\text{pJ}/\text{mm}^2/\text{mR}$ , which is again around a factor 5 worse than for BFB. A final overview of the obtained results for the FCZ based glasses is shown in Fig. 72.

Lithium-borate based (LCB) glasses have been introduced as host material for BaCl<sub>2</sub> nanoparticles and Eu<sup>2+</sup> in order to address issues with homogeneity and reproducibility of the produced FCZ based glasses and glass ceramics. First investigations have shown that adding BaCl<sub>2</sub> to the LCB composition led to an uncontrollable ceramization directly after the pouring step. Regardless mold temperature, the highly oxygen providing LCB glass host leads to only orthorhombic BaCl<sub>2</sub> nanoparticles inside the glass matrix and oxidizes a large amount of the Eu<sup>2+</sup> into Eu<sup>3+</sup> during glass melting and the cooling step. XANES and PL measurements have shown that LCB glasses show significantly lower Eu<sup>2+</sup> fractions than FCZ based glasses. The resulting PSL signals are worse than for FCZ based glasses. Nevertheless, the CE increases with increasing mold temperature to 0.25  $\text{pJ}/\text{mm}^2/\text{mR}$  at 300 °C, because of an increasing volume fraction of orthorhombic BaCl<sub>2</sub> and Eu<sup>3+</sup>. The PSL results of the best working sample out of each series are shown in Fig. 71.

As a new promising medical application, Eu-doped FCZ based glasses and glass ceramics were processed to scintillation fibers for radiation detection. The fiber drawing method via a thin SiO<sub>2</sub> capillary was easier to handle than the pipette method, where the FCZ based glass and the thick SiO<sub>2</sub> pipette had to be

drawn into a thinner fiber leading to a lot of structural problems and defects in the glasses due to the different melting points of the materials. However, the capillary fiber has already shown its scintillation potential under UV excitation, where the typical PL emission bands for  $\text{Eu}^{2+}$  adjacent to or incorporated into hexagonal  $\text{BaCl}_2$  were observed.

The results of this thesis contribute to a greater understanding of the complex fluorozirconate and borate glass systems. The ultimate goal in this field of research is to optimize glass quality, luminescent output, and production costs. It was found that quality, luminescent properties and costs were all inter-related.

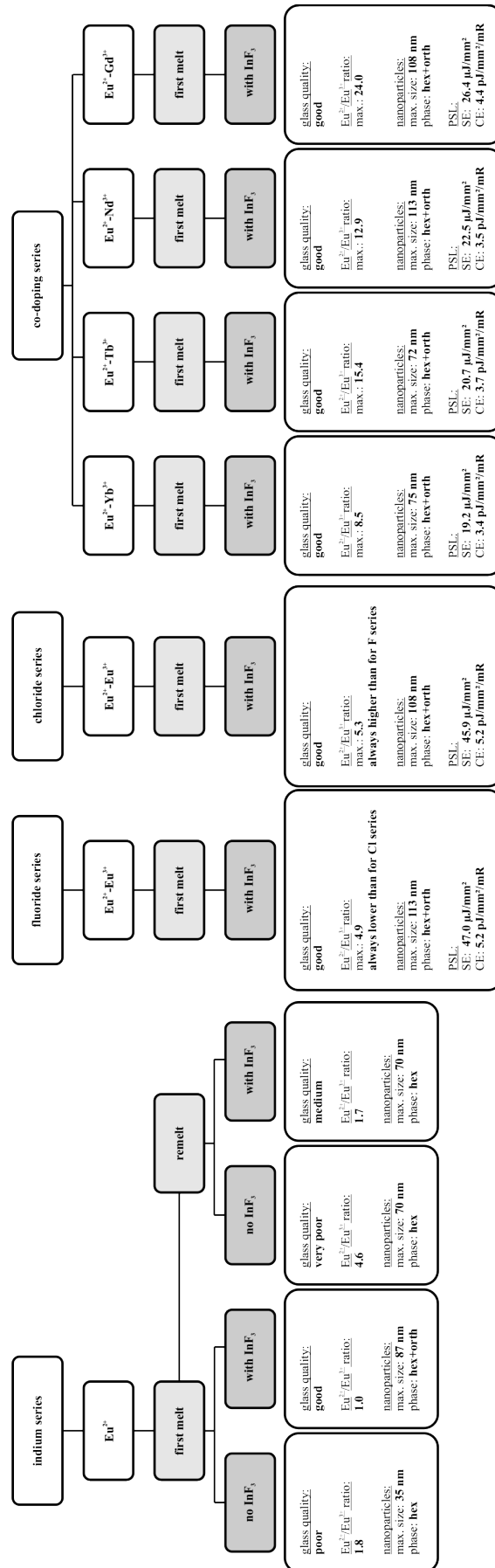


Figure 72: Final overview of the obtained results for the FCZ based glasses.

## OUTLOOK

---

Future work should focus on a better control of the  $\text{BaCl}_2$  crystallization which is essential for the  $\text{Eu}^{2+}$  luminescence. First studies with a two-step annealing process were already successfully done and recently presented on the 18th International Symposium on Non-Oxide and New Optical Glasses ISNOG (St. Malo, France, July 2012). The technique is based on a formation of a large number of nuclei in a first low temperature step with treatment temperatures near the glass transition temperature. In the second step the nucleated grains are grown at the temperature with the maximum crystallization rate; the required sizes can be adjusted by the annealing time. DSC was used to find the maxima in nucleation and crystallization rate for each individual glass. The recently available XRD sample heating stage at the Centre for Innovation Competence SiLi-nano<sup>®</sup> might be a useful tool for an in-situ XRD particle and phase analysis during heating of the glass samples. The possibility of driving defined temperature ramps is a good prerequisite for a reproducible and controlled crystallization.

For the RE co-doping series, a systematic study of different excitation wavelengths for PL and PSL investigations should be considered, in particular in the range of the respective RE excitation bands to check on possible influences on the  $\text{Eu}^{2+}$  luminescence. Beside that, other RE co-dopants could be introduced like  $\text{Sm}^{3+}$ , which lately seems to get growing interest from the glass community, especially in current solid state lighting technology, where co-doping with  $\text{Eu}^{2+}$  can yield in a superimposed emission profile and higher color rendering properties.

For medical and other applications, glasses must have a certain size to cover the necessary area. Thus, a very important area of research is still the up-scaling and the reduction of imperfections including inhomogeneities, bubbles and black spots in the larger glass plates. Normally, air bubbles would be trapped in larger glass batches since thermal convection is not sufficient to let them diffuse from the bottom to the top of the melt. Recently, a breakthrough in bubble reduction was made by drilling side holes into the mold giving them an escape route.

$\text{Eu}^{2+}$ -doped LCB based glasses open a new field of research and make more basic research in terms of glass composition and glass preparation process necessary. A starting point would be the preparation of a borate glass series with various oxygen amounts to confirm that oxygen triggers the  $\text{BaCl}_2$  phase transformation. Furthermore, the  $\text{BaCl}_2$  and  $\text{Eu}^{2+}$ -doping level should be varied in order to investigate the crystallization and luminescence behavior.

The work on scintillating fibers for radiation detection should be pursued further with the aim to optimize the systems' efficiency and cost. Photostimulated luminescence measurements are important to evaluate the functionality, to

find the minimum and maximum possible doses and to create an x-ray dose dependent PSL calibration curve for each fiber. Therefore, longer fibers in the range of 2-3 meters are needed to guide the generated scintillation light out of an x-ray diffractometer into peripheral detection devices (monochromator, photomultiplier, computer). This would drastically increase the costs. An option to minimize the costs could be a split fiber, where the light guiding part is made out of pure ZBLAN, while the scintillating tip is additionally doped with BaCl<sub>2</sub> and Eu<sup>2+</sup>. The usage of Eu<sup>2+</sup> ion implantation should also be evaluated.

Part III

APPENDIX



## CALCULATION OF THE PSL PARAMETERS

---

Table 4 shows the used parameters for the photostimulated luminescence measurements. The relative error is listed in the  $\Delta x/x$  column.

The calculations for the conversion efficiency and stimulation energy were performed at SUNY-Stony Brook, NY, USA, with the software *Matlab* and are described in detail below.

### A.1 CONVERSION EFFICIENCY

$V(t)$  = voltage output from amp at  $t (= R \cdot I(t))$

$ES$  = exposure speed, from fit

$Sr$  = sampling rate = 50 samples/s

time for  $1/e$  decay:

$$T_0 = 1/e \text{ decay time} = (1/ES) \cdot 1/Sr$$

area under  $V(t)$  curve:

$$VOT_0 = V_0 \cdot T_0$$

The conversion efficiency is then calculated by

$$CE = (VOT_0 \cdot E_{ph}) / (R \cdot G \cdot eta \cdot F \cdot Cis \cdot As \cdot alf \cdot Q) \quad (16)$$

with the amplifier transimpedance,  $R$ , the PMT gain,  $G$ , the photocathode quantum efficiency,  $eta$ , the filter transmittance (at 532 nm),  $F$ , the sphere collection efficiency (fraction of sample light collected at exit port),  $Cis$ , the irradiated sample area (size of input hole),  $As$ , the x-ray absorption,  $alf$ , for the specific sample thickness and the x-ray exposure,  $Q$ .

### A.2 STIMULATION ENERGY

$ES$  = exposure speed, from fit

$Sr$  = sampling rate = 50 samples/s

$Ns$  = number of samples = 1000

time for  $1/e$  decay:

$$T_0 = 1/e \text{ decay time} = (1/ES) \cdot 1/Sr$$

The stimulation energy is then calculated by

$$SE = (P_0 \cdot 10^{-3} \cdot f_p \cdot T_0) / As \quad (17)$$

Table 4: Overview of the relative errors  $\Delta x/x$  for various PSL parameters.

parameter	function	value	$\Delta x/x$ [%]
$R$	amplifier transimpedance	1.0E6	These are taken from specifications for the instruments and have no random (experimental) error.
$G$	PMT gain	1.3E5	
$\epsilon$	photocathode QE (at 532 nm)	0.24	
$F$	filter transmittance (at 532 nm)	0.75	5
$C_{is}$	sphere collection efficiency	0.064	3
$Q$	x-ray exposure	320 mR	3
$P_0$	laser power	10.3 mW	2
$f_p$	fraction of laser power transmitted to sample port	3.2E-3	
$T_0$	1/e decay time		10
$V_0 \cdot T_0$	area under fitted S vs. T graph		15
$alf$	x-ray absorption for specific sample thickness	e.g. 0.92	These are calculated from known materials properties and the size of the drilled port hole.
$A_s$	irradiated sample area / size of input hole [mm <sup>2</sup> ]	6.15	
$E_{ph}$	photon energy [eV]	3.1	

## ERROR CALCULATION

---

### B.1 THERMAL STABILITY PARAMETERS

In chapter 5 the Hrubby constant  $H_r$  was calculated by

$$H_r = (T_x - T_g)/(T_m - T_x) \quad (18)$$

with the corresponding absolute errors  $\Delta T_x = \Delta T_g = \Delta T_m = 0.5 \text{ }^\circ\text{C}$ .

For this errors the maximum measurement uncertainty of the measurement result then can be calculated as the total differential of  $H_r$ :

$$\Delta H_r = \left| \frac{\partial H_r}{\partial T_g} \right| \cdot \Delta T_g + \left| \frac{\partial H_r}{\partial T_x} \right| \cdot \Delta T_x + \left| \frac{\partial H_r}{\partial T_m} \right| \cdot \Delta T_m \quad (19)$$

### B.2 PHOTOSTIMULATED LUMINESCENCE

The single PSL measurements are statistically independent of each other and therefore one can say that the influences of the single measurement uncertainties on the uncertainty of the result partially cancel each other. The mathematical approach to this problem is given by a formula for the measurement uncertainty from C. F. Gauß:

$$\Delta y = \sqrt{\sum_{i=1}^x \left( \frac{\partial y}{\partial x_i} \right)^2 \Delta x_i^2} \quad (20)$$

In case of  $y = c \cdot x_1^n \cdot x_2^m$  the following simplified expression for the relative Gaussian Error is valid:

$$\frac{\Delta y}{y} = \sqrt{n^2 \left( \frac{\Delta x_1}{x_1} \right)^2 + m^2 \left( \frac{\Delta x_2}{x_2} \right)^2} \quad (21)$$

By addition of relative errors listed in Table 4 the variations of CE and SE appear to be about  $\frac{\Delta CE}{CE} = 14\%$  and  $\frac{\Delta SE}{SE} = 12\%$ .

## B.3 X-RAY ABSORPTION NEAR EDGE STRUCTURE

The mole fractions of divalent and trivalent Eu ions are calculated by the mole ratio,  $M_{\text{Eu}} = RA_{\text{Eu}}$ , which is determined by the area ratio,  $A_{\text{Eu}}$ , between the  $\text{Eu}^{2+}$  and  $\text{Eu}^{3+}$  WLs from the XANES spectrum. The  $\text{Eu}^{2+}$  fraction is then given by

$$f_{\text{Eu}^{2+}} = \frac{1}{1 + \frac{1}{M_{\text{Eu}}}} \quad (22)$$

and the corresponding maximum measurement uncertainty is calculated as the total differential of  $f_{\text{Eu}^{2+}}$ :

$$\Delta f_{\text{Eu}^{2+}} = \left| \frac{\partial f_{\text{Eu}^{2+}}}{\partial M_{\text{Eu}}} \right| \cdot \Delta M_{\text{Eu}} = \left| \frac{1}{\left(1 + \frac{1}{M_{\text{Eu}}}\right)^2 \cdot M_{\text{Eu}}^2} \right| \cdot \Delta M_{\text{Eu}} \quad (23)$$

The  $\text{Eu}^{3+}$  fraction is given by

$$f_{\text{Eu}^{3+}} = \frac{1}{M_{\text{Eu}} \left(1 + \frac{1}{M_{\text{Eu}}}\right)} \quad (24)$$

and the corresponding maximum measurement uncertainty is:

$$\begin{aligned} \Delta f_{\text{Eu}^{3+}} &= \left| \frac{\partial f_{\text{Eu}^{3+}}}{\partial M_{\text{Eu}}} \right| \cdot \Delta M_{\text{Eu}} \\ &= \left| \frac{1}{M_{\text{Eu}}^2 \left(1 + \frac{1}{M_{\text{Eu}}}\right)} + \frac{1}{M_{\text{Eu}}^3 \left(1 + \frac{1}{M_{\text{Eu}}}\right)^2} \right| \cdot \Delta M_{\text{Eu}}. \end{aligned} \quad (25)$$

## MISCELLANEOUS

## C.1 USED FILTERS

During this thesis, optical glass-plastic composite (KV) filters with long-pass character were used for photoluminescence measurements. Figure 73 shows their spectral internal transmittance,  $\tau_i$ , versus wavelength and their negligible edge shift. KV filters are marked by their low self-fluorescence, which make them attractive for use in spectroscopy. The spectral properties are determined by a plastic film embedded in two glass plates. The spectral internal transmittance for the filters, KV 370 and KV 408, is 50% for the edge wavelengths  $370 \pm 2$  nm and  $408 \pm 2$  nm, respectively. The spectral transmittance can be obtained from multiplication of the  $\tau_i$  values with the reflection coefficient  $P=0.92$ .

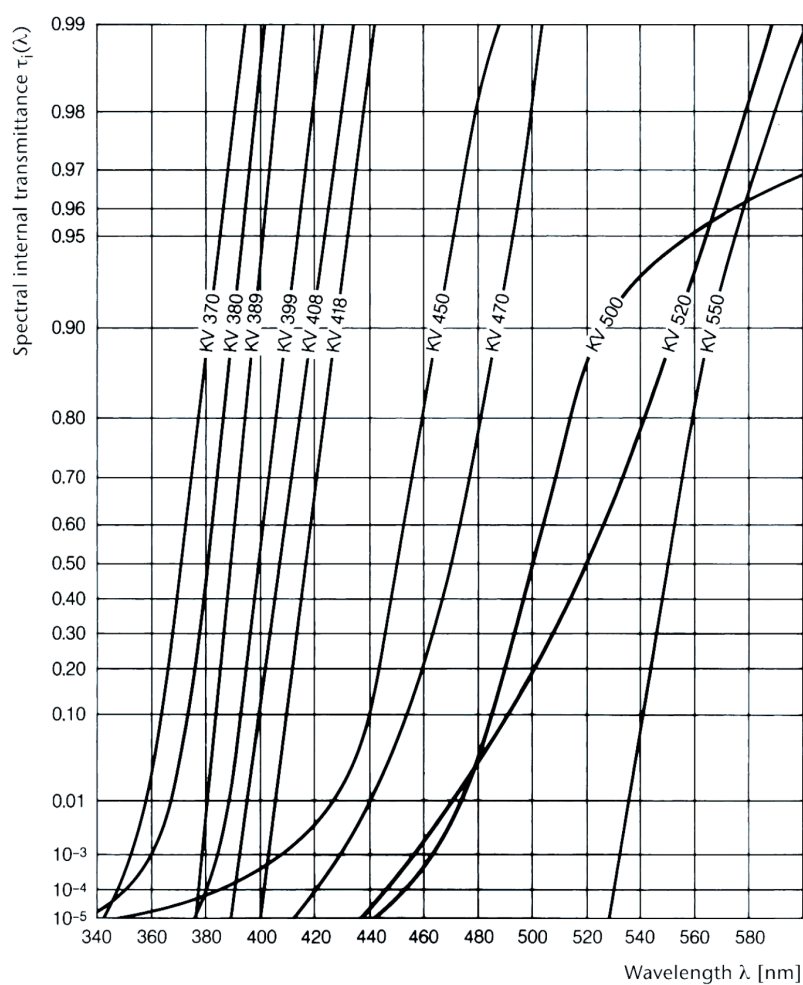


Figure 73: Spectral internal transmittance curves for several KV filters (Schott AG).



## BIBLIOGRAPHY

---

- [1] P. C. Fujiwara. Strahlenbelastung sinkt durch digitales Röntgen. *Management & Krankenhaus*, 2:18, 2001.
- [2] S. Schweizer. Physics and Current Understanding of X-Ray Storage Phosphors. *Phys. Stat. Sol. A*, **187**(2):335, 2001.
- [3] G. Chen, J. A. Johnson, R. Weber, S. Schweizer, D. MacFarlane, J. Woodford, and F. De Carlo. ZBLAN-based x-ray storage phosphors and scintillators for digital x-ray imaging. *Proc. SPIE*, 5745:1351–1358, 2005.
- [4] J. A. Johnson, S. Schweizer, B. Henke, G. Chen, J. Woodford, P. J. Newman, and D. R. MacFarlane. Eu-activated fluorochlorozirconate glass-ceramic scintillators. *J. Appl. Phys.*, **100**:034701, 2006.
- [5] J. A. Johnson, R. Weber, S. Schweizer, D. R. MacFarlane, P. Newman, and G. Chen. Multi-radiation large area detector. Technical report, The University of Chicago, 2007.
- [6] J. A. Johnson, S. Schweizer, and A. R. Lubinsky. A Glass-Ceramic Plate for Mammography. *J. Am. Ceram. Soc.*, **90**(3):693–698, 2007.
- [7] J. A. Johnson, R. Weber, A. I. Kolesnikov, and S. Schweizer. Glass Ceramics for High-Resolution Imaging. In *Proceedings of IMECE2008, 2008 ASME International Mechanical Engineering Congress and Exposition, October 31 - November 6, 2008, Boston, MA, USA*, 2008.
- [8] P. N. Prasad. *Nanophotonics*. John Wiley & Son, Inc., New Jersey, 2004.
- [9] S. Schweizer, L. W. Hobbs, M. Secu, J.-M. Spaeth, A. Edgar, and G. V. M. Williams. Photostimulated luminescence in Eu-doped fluorochlorozirconate glass ceramics. *Appl. Phys. Lett.*, **83**(3):449, July 2003.
- [10] S. Schweizer, L. W. Hobbs, M. Secu, J.-M. Spaeth, A. Edgar, G. V. M. Williams, and J. Hamlin. Photostimulated luminescence from fluorochlorozirconate glass ceramics and the effect of crystallite size. *J. Appl. Phys.*, **97**:083522, 2005.
- [11] Information about the cost of rare-earth minerals in recent times, [http://www.upi.com/Business\\_News/Energy-Resources/2011/06/23/rare-earth-minerals-prices-skyrocket/UPI-76601308849756/](http://www.upi.com/Business_News/Energy-Resources/2011/06/23/rare-earth-minerals-prices-skyrocket/UPI-76601308849756/), June 23 2011.
- [12] J. A. Rard. Chemistry and thermodynamics of europium and some of its simpler inorganic compounds and aqueous species. *Chem. Rev.*, **85**:555–582, 1985.

- [13] L. Massot, P. Chamelot, L. Cassayre, and P. Taxil. Electrochemical study of the Eu(III)/Eu(II) system in molten fluoride media. *Electrochim. Acta*, **54**:6361–6366, 2009.
- [14] J. K. R. Weber, M. Vu, C. Paßlick, S. Schweizer, D. E. Brown, C. E. Johnson, and J. A. Johnson. The oxidation state of europium in halide glasses. *J. Phys.: Condens. Matter*, **23**:495402, 2011.
- [15] S. Schweizer, B. Henke, P. T. Miclea, B. Ahrens, and J. A. Johnson. Multifunctionality of fluorescent nanocrystals in glass ceramics. *Radiat. Meas.*, **45**:485–489, 2010.
- [16] B. Ahrens, B. Henke, P. T. Miclea, J. A. Johnson, and S. Schweizer. Enhanced up-converted fluorescence in fluorozirconate based glass ceramics for high efficiency solar cells. *Proceedings of SPIE: Photonics for Solar Energy Systems II*, 7002:700206, 2008.
- [17] B. Ahrens, P. Löper, J. C. Goldschmidt, S. Glunz, B. Henke, P. T. Miclea, and S. Schweizer. Neodymium-doped fluorochlorozirconate glasses as an upconversion model system for high efficiency solar cells. *Phys. Status Solidi A*, **205**(12):2822–2830, 2008.
- [18] C. Paßlick, B. Henke, B. Ahrens, P. T. Miclea, J. Wenzel, E. Reisacher, W. Pfeiffer, J. A. Johnson, and S. Schweizer. Glass-ceramic covers for highly efficient solar cells. In *SPIE Newsroom*, 2010.
- [19] J. Miyahara and K. Takahashi. A new type of x-ray area detector utilizing laser stimulated luminescence. *Nucl. Instrum. Methods Phys. Res. A*, **246**:572–578, 1986.
- [20] S. V. Moharil. A review of X-ray imaging phosphors. *Bull. Mater. Sci.*, **17**(1):25–33, 1994.
- [21] M. Sonoda, J. Takano, J. Miyahara, and H. Cato. Computed Radiography Utilizing Scanning Laser Stimulated Luminescence. *Radiology*, **148**:833–838, 1983.
- [22] Private communication with R. Lubinsky.
- [23] G. Blasse and B. C. Grabmaier. *Luminescent Materials*. Springer Verlag, Berlin Heidelberg, 1994.
- [24] H. E. Hoefdraad. Charge-transfer spectra of tetravalent lanthanide ions in oxides. *J. Inorg. Nucl. Chem.*, **37**:1917–1921, 1975.
- [25] J. A. Koningstein. Energy Levels and Crystal-Field Calculations of Europium and Terbium in Yttrium Aluminum Garnet. *Phys. Rev.*, **136**(3A):A717, 1964.
- [26] C. Görrler-Walrand, E. Huygen, K. Binnemans, and L. Fluyt. Optical absorption spectra, crystal-field energy levels and intensities of Eu<sup>3+</sup> in GdAl<sub>3</sub>(BO<sub>3</sub>)<sub>4</sub>. *J. Phys. B: Condens. Matter*, **6**(38):7797–7812, 1994.

- [27] Mi. Poulain, Ma. Poulain, J. Lucas, and P. Brun. Verres fluores au tetrafluorure de zirconium proprietes optiques d'un verre dope au  $\text{Nd}^{3+}$ . *Mater. Res. Bull.*, **10**(4):243, 1975.
- [28] K. Ohsawa and T. Shibata. Preparation and Characterization of  $\text{ZrF}_4$ - $\text{BaF}_2$ - $\text{LaF}_3$ - $\text{NaF}$ - $\text{AlF}_3$  Glass Optical Fibers. *J. Lightwave Technol.*, **LT-2**(5), 1984.
- [29] I. D. Aggarwal and G. Lu. *Fluoride Glass Fibre Optics*. Academic Press, INC., 1991.
- [30] L. Wetenkamp, G. F. West, and H. Többen. Optical properties of rare earth-doped ZBLAN glasses. *J. Non-Cryst. Solids*, **140**:35–40, 1992.
- [31] M. Dyrba, P.-T. Miclea, and S. Schweizer. Spectral down-conversion in Sm-doped borate glasses for photovoltaic applications. *Proc. SPIE*, **7725**:77251D, 2010.
- [32] J. Bischoe and B. E. Warren. X-ray diffraction study of soda-boric oxide glass. *J. Am. Ceram. Soc.*, **21**(8):287–293, 1938.
- [33] G. Liu and H. A. Eick. Solvolytic decomposition studies on mixed phases: Synthesis of the anti- $\text{Fe}_2\text{P}$ -type  $\text{BaX}_2$  ( $X = \text{Cl}, \text{Br}$ ) from  $\text{BaX}_2$ — $\text{LnX}_3$  phases. *J. of the Less Common Metals*, **129**:47, 1989.
- [34] C. Bohley, J.-M. Wagner, C. Pfau, P.-T. Miclea, and S. Schweizer. Raman spectra of barium halides in orthorhombic and hexagonal symmetry: An ab initio study. *Phys. Rev. B*, **83**:024107, 2011.
- [35] A. Sadoc and A. Guillo. *C. R. Acad. Sci. Ser. B*, **273**:203, 1971.
- [36] S. Aasland, M.-A. Einarsrud, and T. Grande. Spectroscopic Investigations of Fluorozirconate Glasses in the Ternary Systems  $\text{ZrF}_4$ - $\text{BaF}_2$ - $\text{AF}$  ( $A = \text{Na}, \text{Li}$ ). *J. Phys. Chem.*, **100**(13):5457–5463, 1996.
- [37] E. B. Brackett, T. E. Brackett, and R. L. Sass. The Crystal Structures of Barium Chloride, Barium Bromide, and Barium Iodide. *J. Phys. Chem.*, **67**(10):2132, 1963.
- [38] B. K. Vainshtein. *Dokl. Akad. Nauk SSSR*, **60**:1169, 1948.
- [39] B. K. Teo. *EXAFS: Basic Principles and Data Analysis*. Springer-Verlag GmbH, 1986.
- [40] J. A. Bearden and A. F. Burr. Reevaluation of X-Ray Atomic Energy Levels. *Rev. Mod. Phys.*, **39**:125, 1967.
- [41] T. Ressler. WinXAS: a Program for X-ray Absorption Spectroscopy Data Analysis under MS-Windows. *J. Synchrotron Rad.*, **5**:118–122, 1998.
- [42] M. O. Krause and J. H. Oliver. Natural widths of atomic K and L levels,  $\text{K}\alpha$  X-ray lines and several KLL Auger lines. *J. Phys. Chem. Ref. Data*, **8**:329, 1979.

- [43] J. I. Langford and A. J. C. Wilson. Scherrer after Sixty Years: A Survey and Some New Results in the Determination of Crystallite Size. *J. Appl. Cryst.*, **11**:102–113, 1978.
- [44] P. Scherrer. Bestimmung der Grösse und der inneren Struktur von Kolloidteilchen mittels Röntgenstrahlen. *Nachr. Ges. Wiss. Göttingen*, **2**:98–100, 1918.
- [45] A. Hruby. Evaluation of glass forming tendency by means of DTA. *Czech. J. Phys. B*, **22**:1187, 1972.
- [46] S. Schweizer, B. Henke, S. Köneke, J. A. Johnson, G. Chen, and J. Woodford. Energy-dependent scintillation intensity of fluorozirconate-based glass-ceramic x-ray detectors. *Proc. of SPIE*, **6142**:61422Y–1, 2006.
- [47] G. Chen, J. Johnson, J. Woodford, and S. Schweizer. Insights into phase formation in fluorochlorozirconate glass-ceramic storage phosphors. *Appl. Phys. Lett.*, **88**:191915, 2006.
- [48] A. Glassner. *A survey of the free energies of formation of the fluorides, chlorides, and oxides of the elements to 2500 K*. Argonne, Ill. : Argonne National Laboratory, Chemical Engineering Division, 1953.
- [49] J. Ball, C. M. Jenden, S. J. Lyle, and W. A. Westall. A moessbauer spectroscopy study of an anhydrous non-stoichiometric europium (III) chloride phase. *J. Less Common Met.*, **95**:161–70, 1983.
- [50] J. M. Parker. Fluoride Glasses. *Annu. Rev. Mater. Sci.*, **19**:21, 1989.
- [51] M. M. Broer. Melting Apparatus for the Synthesis of Bulk ZrF<sub>4</sub>-Based Fluoride Glass. *J. Am. Ceram. Soc.*, **72**(3):492–495, 1989.
- [52] L. J. Moore, D. R. MacFarlane, and P. J. Newman. Surface crystallization of ZBLAN glasses. *J. Non-Cryst. Solids*, **140**:159–165, 1992.
- [53] B. Henke, C. Paßlick, P. Keil, J. A. Johnson, and S. Schweizer. Eu oxidation state in fluorozirconate-based glass ceramics. *J. Appl. Phys.*, **106**:113501, 2009.
- [54] J. Rohler. *Handbook on the Physics and Chemistry of Rare Earths*. North-Holland, Amsterdam, 1987.
- [55] Y. Takahashi, G. R. Kolonin, G. P. Shironosova, I. I. Kupriyanova, T. Uruga, and H. Shimizu. Determination of the Eu(II)/Eu(III) ratios in minerals by X-ray absorption near-edge structure (XANES) and its application to hydrothermal deposits. *Miner. Mag.*, **69**(2):179–190, 2005.
- [56] M. R. Antonio, L. Soderholm, and I. Song. Design of spectroelectrochemical cell for in situ X-ray absorption fine structure measurements of bulk solution species. *J. Appl. Electrochem.*, **27**:784–792, 1997.
- [57] M. Baricco, L. Battezzati, M. Braglia, G. Cocito, J. Kraus, and E. Modone. Crystallization behaviour of fluorozirconate glasses. *J. Non-Cryst. Solids*, **161**:60–65, 1993.

- [58] A. Edgar, M. Secu, G. V. M. Williams, S. Schweizer, and J.-M. Spaeth. Structural phase changes in barium bromide nano-crystals in a fluorobromozirconate glass-ceramic x-ray storage phosphor. *J. Phys.: Condens. Matter*, **13**:6259–6269, 2001.
- [59] M. Secu, S. Schweizer, U. Rogulis, and J.-M. Spaeth. Radiation-induced defects and their recombination processes in the x-ray storage phosphor BaBr<sub>2</sub>:Eu<sup>2+</sup>. *J. Phys.: Condens. Matter*, **15**:2061, 2003.
- [60] T. Kobayasi, S. Mroczkowski, J. F. Owen, and L. H. Brixner. Fluorescence lifetime and quantum efficiency for 5d → 4f transitions in Eu<sup>2+</sup> doped chloride and fluoride crystals. *J. Lum.*, **21**(3):247–257, 1980.
- [61] C. Paßlick, B. Ahrens, B. Henke, J. A. Johnson, and S. Schweizer. Structural properties of fluorozirconate-based glass ceramics doped with multivalent europium. *J. Appl. Phys.*, **110**:113527, 2011.
- [62] D. R. MacFarlane, P. J. Newman, J. D. Cashion, and A. Edgar. In situ generation of Eu<sup>2+</sup> in glass-forming melts. *J. Non-Cryst. Solids*, **256&257**:53, 1999.
- [63] B. Phebus, B. Getman, S. Kiley, D. Rauser, M. Plesha, and R. H. Terrill. Preparation and analysis of Eu<sup>3+</sup>- and Eu<sup>2+</sup>-doped ZBLAN and ZBLALi fluorozirconate glasses. *Solid State Ion.*, **176**:2631–2638, 2005.
- [64] J. M. D. Coey, A. McEvoy, and M. W. Shafer. Moessbauer study of europium in fluorozirconate glass. *J. Non-Cryst. Solids*, **43**:387–92, 1981.
- [65] D. M. Laptev, T. V. Kiseleva, N. M. Kulagin, V. F. Goryushkin, and E. S. Voronkov. *Russ. J. Inorg. Chem.*, **31**:1965, 1986.
- [66] H. E. Kissinger. Reaction Kinetics in Differential Thermal Analysis. *Anal. Chem.*, **29**(11):1702–1706, 1957.
- [67] L. Samek, J. Wasylak, and K. Marczuk. Optical properties of fluorozirconate glasses activated with rare earth elements. *J. Non-Cryst. Solids*, **140**:243–248, 1992.
- [68] M. Secu, R. Kalchgruber, S. Schweizer, J.-M. Spaeth, and A. Edgar. Photo-stimulated luminescence in BaX<sub>2</sub>:Eu<sup>2+</sup> (X = Br, Cl) X-ray storage phosphors. *Radiation Effects & Defects in Solids*, **157**:957–962, 2002.
- [69] B. Ahrens, C. Eisenschmidt, J. A. Johnson, P. T. Miclea, and S. Schweizer. Structural and optical investigations of Nd-doped fluorozirconate-based glass ceramics for enhanced upconverted fluorescence. *Appl. Phys. Lett.*, **92**:061905, 2008.
- [70] C. Paßlick, B. Ahrens, B. Henke, J. A. Johnson, and S. Schweizer. Differential scanning calorimetry investigations on Eu-doped fluorozirconate-based glass ceramics. *J. Non-Cryst. Solids*, **356**:3085–3089, 2010.
- [71] C. Paßlick, B. Ahrens, B. Henke, J. A. Johnson, and S. Schweizer. Crystallization behavior of rare-earth doped fluorochlorozirconate glasses. *J. Non-Cryst. Solids*, **357**(11-13):2450–2452, 2011.

- [72] V. S. R. Murthy. *Structure and Properties of Engineering Materials*. Tata McGraw-Hill Publishing Company Limited, New Delhi, 2003.
- [73] M. T. Harrison and R. G. Denning. Site selective spectroscopy and molecular dynamics simulation of Eu(III) ZBLAN glasses. *J. Lumin.*, **69**(5-6):265–285, 1996.
- [74] E. Clementi, D. L. Raimondi, and W. P. Reinhardt. Atomic Screening Constants from SCF Functions. II. Atoms with 37 to 86 Electrons. *J. Chem. Phys.*, **47** (4):1300–1307, 1967.
- [75] G. A. Appleby, C. M. Bartle, G. V. M. Williams, and A. Edgar. Lithium borate glass ceramics as thermal neutron imaging plates. *Current Applied Physics*, **6**:389–392, 2006.
- [76] G. A. Appleby, A. Edgar, G. V. M. Williams, and P. Vontobel. Structure and neutron imaging characteristics of lithium borate-barium chloride glass-ceramics. *Nucl. Instrum. Methods Phys. Res., Sect A*, **564**(1):424, 2006.
- [77] P. Goldschmidt. Glaskeramische Fasern für medizinische Anwendungen. Zentrum für Innovationskompetenz SiLi-nano, Martin-Luther-Universität Halle-Wittenberg, August 2012.
- [78] Robert Bringhurst. *The Elements of Typographic Style*. Version 2.5. Hartley & Marks, Publishers, Point Roberts, WA, USA, 2002.

## PUBLICATIONS

---

Some parts and figures of this work have appeared previously in the following publications:

- (1) B. Henke, C. Paßlick, P. Keil, J. A. Johnson, and S. Schweizer  
*Eu oxidation state in fluorozirconate-based glass ceramics*  
J. Appl. Phys. 106, 113501 (2009).
- (2) B. Henke, P. Keil, C. Paßlick, D. Vogel, M. Rohwerder, M. C. Wiegand, J. A. Johnson, and S. Schweizer  
*XANES studies on Eu-doped fluorozirconate based glass-ceramics*  
Mater. Res. Soc. Symp. Proc. Vol. 1262, 1262-W08-03 (2010).
- (3) S. Schweizer, B. Henke, B. Ahrens, C. Paßlick, P. T. Miclea, J. Wenzel, E. Reisacher, W. Pfeiffer, and J. A. Johnson  
*Progress on up- and down-converted fluorescence in rare-earth doped fluorozirconate-based glass ceramics for high efficiency solar cells*  
Proc. SPIE 7725, 77250X (2010).
- (4) C. Paßlick, B. Ahrens, B. Henke, J. A. Johnson, and S. Schweizer  
*Differential scanning calorimetry investigations on Eu-doped fluorozirconate-based glass ceramics*  
J. Non-Cryst. Solids 356, 3085–3089 (2010).
- (5) C. Paßlick, B. Henke, B. Ahrens, , P. T. Miclea, J. Wenzel, E. Reisacher, W. Pfeiffer, J. A. Johnson, and S. Schweizer  
*Glass-ceramic covers for highly efficient solar cells*  
SPIE Newsroom, 25 May 2010.
- (6) C. Paßlick, B. Henke, I. Császár, B. Ahrens, P. T. Miclea, J. A. Johnson, and S. Schweizer  
*Advances in up- and down-converted fluorescence for high efficiency solar cells using rare-earth doped fluorozirconate-based glasses and glass ceramics*  
Proc. SPIE 7772, 77720A (2010).

- (7) S. Schweizer, C. Paßlick, B. Ahrens, B. Henke, P. T. Miclea, and J. A. Johnson  
*Rare-earth doped fluorozirconate-based glass ceramics for high efficiency solar cells: Recent developments*  
Proc. of 25th European Photovoltaic Solar Energy Conference and Exhibition / 5th World Conference on Photovoltaic Energy Conversion, 6-10 September 2010, Valencia, Spain, p. 47.
- (8) C. Paßlick, B. Ahrens, B. Henke, J. A. Johnson, and S. Schweizer  
*Crystallization behavior of rare-earth doped fluorochlorozirconate glasses*  
J. Non. Cryst. Sol. 357, 2450–2452 (2011).
- (9) B. Ahrens, S. Brand, T. Büchner, P. Darr, S. Schönfelder, C. Paßlick, and S. Schweizer  
*Mechanical properties of fluorozirconate-based glass ceramics for medical and photovoltaic applications*  
J. Non. Cryst. Sol. 357, 2264–2267 (2011).
- (10) J. K. R. Weber, M. Vu, C. Paßlick, S. Schweizer, D. E. Brown, C. E. Johnson, and J. A. Johnson  
*The oxidation state of europium in halide glasses*  
Journal of Physics: Condensed Matter 23, 495402 (2011).
- (11) C. Paßlick, O. Müller, D. Lützenkirchen-Hecht, R. Frahm, J. A. Johnson, and S. Schweizer  
*Structural properties of fluorozirconate-based glass ceramics doped with multivalent europium*  
J. Appl. Phys. 110, 113527 (2011).
- (12) C. E. Johnson, M. Vu, J. A. Johnson, D. E. Brown, J. K. R. Weber, C. Paßlick, and S. Schweizer  
*Mössbauer spectroscopy of europium-containing glasses: Optical activator study for x-ray image plates*  
Submitted to Hyperfine Interact. (2011).
- (13) C. Paßlick, J. A. Johnson, and S. Schweizer  
*Crystallization studies on rare-earth co-doped fluorozirconate-based glasses*  
Accepted for publication in J. Non. Cryst. Sol. (January 2013).
- (14) C. Pfau, C. Paßlick, S. Gray, J. A. Johnson, C. E. Johnson, and S. Schweizer  
*Mössbauer spectroscopy of europium-doped fluorochlorozirconate glasses and glass ceramics: optimization of storage phosphors in computed radiography*  
Submitted to J. Phys.: Condens. Matter (January 2013).

Presented talks at conferences:

- (1) *Crystallization and structural investigation of Eu-doped fluorozirconate-based glass ceramics*  
Condensed Matter Division of the German Physical Society (DPG),  
(Regensburg, Germany, March 2010).
- (2) *Crystallization behavior of rare-earth doped fluorochlorozirconate glasses*  
17th International Symposium on Non-Oxide and New Optical Glasses  
XVII ISNOG (Ningbo, China, June 2010).
- (3) *Progress on up- and down-converted fluorescence in rare-earth doped fluorozirconate-based glasses and glass ceramics for high efficiency solar cells*  
Solar Energy + Technology Division of the SPIE Optics + Photonics  
(San Diego, USA, August 2010).
- (4) *Optical and structural properties of fluorozirconate-based glass ceramics doped with divalent and trivalent europium*  
Condensed Matter Division of the German Physical Society (DPG),  
(Dresden, Germany, March 2011).
- (5) *Two-step annealing process for controlled barium halide crystallization in Eu-doped fluorozirconate-based glasses*  
18th International Symposium on Non-Oxide and New Optical Glasses  
ISNOG (St. Malo, France, July 2012).



*Success has nothing to do with what you gain in life or accomplish for yourself. It's what you do for others.*

— Danny Thomas

## ACKNOWLEDGEMENTS

---

An dieser Stelle möchte ich all denjenigen danken, die in irgendeiner Art und Weise zu dieser Promotion beigetragen haben:

PROF. DR. STEFAN SCHWEIZER danke ich für die Möglichkeit in seiner Arbeitsgruppe zu promovieren und besonders für die stets hilfsbereite und kompetente Betreuung und Förderung, auch nachdem ich die Universität frühzeitig verlassen hatte.

PROF. DR. RALF B. WEHRSPHORN sei gedankt für die Übernahme der Aufgabe als Zweitgutachter und sein Interesse an dieser Arbeit.

CHARLOTTE PFAU und NEHA SARDANA sei gedankt für die tolle Büro-Atmosphäre, ihre stets offenen Ohren und die vielen Gespräche und Diskussionen.

DR. BERND AHRENS und PETER NOLTE danke ich für wissenschaftliche Diskussionen, aber vor allem für die zahlreichen außeruniversitären Aktionen, wie Sport, Skatrunden oder entspannende Stammtische. DR. BERND AHRENS gilt insbesondere mein Dank für die XANES-Messungen in Hamburg sowie die ausgiebige Korrekturlesung.

DR. KERSTIN MITZSCHKE und DR. ANNETT WELTROWSKI gebührt mein Dank für ihre Hilfe bei unzähligen Verwaltungsangelegenheiten, vor allem den Dienstreise-Abrechnungen.

OLIVER MÜLLER sei gedankt für die sehr gute Kooperation hinsichtlich der Synchrotron-Aufenthalte, die zur Verfügung gestellten Strahlzeit am Hasylab, Hamburg, und hinsichtlich der XANES Messdatenauswertungen.

DR. BASTIAN HENKE danke ich für die vielen Geräte-Einführungen und die gemeinsamen Strahlzeiten in Argonne.

DR. PAUL MICLEA, DR. MANUELA MICLEA, DR. CHRISTIAN BOHLEY und ULRICH SKRZYPCZAK möchte ich für zahlreiche helfende Diskussionen danken.

Regarding the research stays at the University of Tennessee Space Institute in Tullahoma, TN, USA, many thanks go to PROF. DR. JACQUELINE ANNE and PROF. DR. CHARLES JOHNSON, DOUG WARNBERG, BETSY HARBIN, MANH VU, CAROLE THOMAS and especially to the reviewers and good friends LEE LEONARD, CHRIS FOERSTER and SHARON GRAY for the good cooperation, support, provision of glass samples, ideas and the great time.

PHILIPP GOLDSCHMIDT, LUISE WAGNER, TORSTEN BÜCHNER und MONIQUE IRRGANG möchte ich danken für ihre Zuarbeit bei Probenpräparation, Glasherstellung und den vielen anfallenden Kleinigkeiten im Laboralltag; PHILIPP GOLDSCHMIDT besonders für seine Arbeit und Versuche mit den Glasfasern.

Dem gesamten ZIK und der Fachgruppe  $\mu$ MD gilt mein Dank für die gute Zusammenarbeit und das tolle Arbeitsklima.

Many thanks go to DR. ANTHONY RICK LUBINSKY for discussions and the PSL measurements at SUNY-Stony Brook, NY, USA, and to DR. RICK WEBER from Materials Development Inc. in Arlington Heights, IL, USA, for helpful conversations and the good cooperation.

Für die manchmal doch nötige außeruniversitäre Abwechslung in Halle, möchte ich all meinen Hallenser Freunden danken.

Meinen ehemaligen Kommilitonen aus der Paderborner Zeit, speziell CHRISTIAN MIETZE, ALEXANDER ZADO, CHRISTIAN HÖLSCHER, MAIK PALUGA und HOLGER MÜHLENBERND, möchte ich natürlich auch danken – für die Lernrunden, aber auch für die gute Zeit.

Meiner Freundin, EUGÉNIE VERBEURGT, danke ich für Ihre herzliche Unterstützung, das entgegengebrachte Verständnis und vor allem für die Motivation in den letzten Wochen des Schreibens.

Ein besonders herzlicher Dank gilt meinen ELTERN und meinem BRUDER, von denen ich immer Unterstützung und Hilfe in allen Lagen erfahren durfte.

Danke auch allen, die keine namentliche Erwähnung gefunden, aber dennoch zum Gelingen dieser Arbeit beigetragen haben.

This work was supported by the FhG Internal Programs under Grant No. Attract 692 034. In addition, I would like to thank the German Science Foundation ('Deutsche Forschungsgemeinschaft') (DFG Project No. PAK88) and the Federal Ministry for Education and Research ('Bundesministerium für Bildung und Forschung') for their financial support within the Centre for Innovation Competence SiLi-nano<sup>®</sup> (project number 03Z2HN11).

Parts of this work were also supported by the National Institute of Biomedical Imaging and Bioengineering (NIBIB) (Grant No. 5R01EB006145-02) and the National Science Foundation under Grant Number DMR1001381. The content is solely the responsibility of the author and does not necessarily represent the official views of the NIBIB or the National Institutes of Health.

Portions of this work were performed at the DuPont-Northwestern-Dow Collaborative Access Team (DND-CAT) located at Sector 5 of the Advanced Photon Source (APS). DND-CAT is supported by E.I. DuPont de Nemours & Co., The Dow Chemical Co., the U.S. National Science Foundation through Grant No. DMR-9304725 and the State of Illinois through the Department of Commerce and the Board of Higher Education Grant No. IBHE HECA NWU 96. Use of the APS was supported by the U.S. Department of Energy, Office of Science, Office of Basic Energy Sciences, under Contract No. DE-AC02-06CH11357 (2009) and W-31 – 109-Eng-38 (2011).

#### COLOPHON

This thesis was typeset with  $\text{\LaTeX} 2_{\epsilon}$  using Hermann Zapf's *Palatino* and *Euler* type faces (Type 1 PostScript fonts *URW Palladio L* and *FPL* were used). The listings are typeset in *Bera Mono*, originally developed by Bitstream, Inc. as "Bitstream Vera". (Type 1 PostScript fonts were made available by Malte Rosenau and Ulrich Dirr.)

The typographic style was inspired by Bringhurst's genius as presented in *The Elements of Typographic Style* [78]. It is available for  $\text{\LaTeX}$  via CTAN as "classicthesis".



# LEBENS LAUF

---

## PERSÖNLICHE DATEN

Christian Paßlick

Köppenweg 35  
37574 Einbeck

E-Mail: christian.passlick@physik.uni-halle.de

Geboren am 14.04.1985 in Bad Driburg

## BILDUNGSWEG

- 08/1991–07/1995 **Besuch der Kath. Grundschule Bredenborn**
- 08/1995–06/2004 **Besuch des Gymnasiums St. Xaver** in Bad Driburg  
Abschluss: Abitur
- 07/2004–10/2004 **Grundwehrdienst** im 6. ABCAbwBtl 7 in Höxter
- 10/2004–10/2009 **Studium der Physik** an der Universität Paderborn  
Abschluss: Master of Science in Physics mit Auszeichnung
- 10/2009–09/2012 **Anstellung als wissenschaftlicher Mitarbeiter**  
Zentrum für Innovationskompetenz SiLi-Nano<sup>®</sup>,  
Halle (Saale)
- 09/2012–dato **Anstellung als Entwickler für Optik/Lichttechnik**  
Auer Lighting GmbH, Bad Gandersheim



## DECLARATION

---

I hereby declare that this submission is my own work and to the best of my knowledge it contains no materials previously published or written by another person, nor material which to a substantial extent has been accepted for the award of any other degree or diploma at the Martin Luther University of Halle-Wittenberg or any other educational institution, except where the acknowledgement is made in the thesis. Any contribution made to the research by others, with whom I have worked at Halle or elsewhere, is explicitly acknowledged in the thesis. I also declare that the intellectual content of this thesis is the product of my own work, except to the extent that assistance from others in the project's design and conceptions or in style, presentation and linguistic expression is acknowledged.

*Halle (Saale), March 2013*

---

Christian Paßlick